

DISSERTATION

ATTENUATION CORRECTION OF X-BAND POLARIMETRIC DOPPLER WEATHER RADAR
SIGNALS: APPLICATION TO SYSTEMS WITH HIGH SPATIO-TEMPORAL RESOLUTION

Submitted by

Miguel Bustamante Gálvez

Department of Electrical and Computer Engineering

In partial fulfillment of the requirements

For the Degree of Doctor of Philosophy

Colorado State University

Fort Collins, Colorado

Fall 2015

Doctoral Committee:

Advisor: V. N. Bringi

Co-Advisor: Jose G. Colom-Ustariz

Anura Jayasumana

Ali Pezeshki

Paul W. Mielke

Copyright by Miguel Bustamante Gálvez 2015

All Rights Reserved

ABSTRACT

ATTENUATION CORRECTION OF X-BAND POLARIMETRIC DOPPLER WEATHER RADAR SIGNALS: APPLICATION TO SYSTEMS WITH HIGH SPATIO-TEMPORAL RESOLUTION

In the last decade the atmospheric science community has seen widespread and successful application of X-band dual-polarization weather radars for measuring precipitation in the lowest 2 km of the troposphere. These X-band radars have the advantage of a smaller footprint, lower cost, and improved detection of hydrometeors due to increased range resolution. In recent years, the hydrology community began incorporating these radars in novel applications to study the spatio-temporal variability of rainfall from precipitation measurements near the ground, over watersheds of interest. The University of Iowa mobile XPOL radar system is one of the first to be used as an X-band polarimetric radar network dedicated to hydrology studies. During the spring of 2013, the Iowa XPOL radars participated in NASA Global Precipitation Measurements (GPM) first field campaign focused solely on hydrology studies, called the Iowa Flood Studies (IFloodS).

Weather radars operating in the 3.2 cm (X-band) regime can suffer from severe attenuation, particularly in heavy convective storms. This has led to the development of sophisticated algorithms for X-band radars to correct the meteorological observables for attenuation. This is especially important for higher range resolution hydrology-specific X-band weather radars, where the attenuation correction aspect remains relatively unexamined. This research studies the problem of correcting for precipitation-induced attenuation in X-band polarimetric weather radars with high spatio-temporal resolution for hydrological applications. We also examine the variability in scattering simulations obtained from the drop spectra measured by two dimensional video disdrometers (2DVD) located in different climatic and

geographical locations. The 2DVD simulations provide a ground truth for various relations (e.g., $A_H - K_{DP}$ and $A_H - A_{DP}$) applied to our algorithms for estimating attenuation, and ultimately correcting for it to provide improved rain rates and hydrometeor identification.

We developed a modified ZPHI attenuation correction algorithm, with a differential phase constraint, and tuned it for the high resolution IFloodS data obtained by the Iowa XPOL radars. Although this algorithm has good performance in pure rain events, it is difficult to fully correct for attenuation and differential attenuation near the melting layer where a mixed phase of rain and melting snow or graupel exists. To identify these regions, we propose an improved iterative FIR range filtering technique, as first presented by Hubbert and Bringi (1995), to better estimate the differential backscatter phase, δ , due to Mie scattering at X-band from mixed phase precipitation.

In addition, we investigate dual-wavelength algorithms to directly estimate the α and β coefficients, of the $A_H = \alpha K_{DP}$ and $A_{DP} = \beta K_{DP}$ relations, to obtain the path integrated attenuation due to rain and wet ice or snow in the region near the melting layer. We use data from the dual-wavelength, dual-polarization CHILL S-/X-band Doppler weather radar for analyzing the coefficients and compare their variability as a function of height, where the hydrometeors are expected to go through a microphysical transformation as they fall, starting as snow or graupel/hail then melting into rain or a rain-hail mixture. The S-band signal is un-attenuated and so forms a reference for estimating the X-band attenuation and differential attenuation. We present the ranges of the α and β coefficients in these varying precipitation regimes to help improve KDP-based attenuation correction algorithms at X-band as well as rain rate algorithms based on the derived A_H .

ACKNOWLEDGEMENTS

I begin by thanking God for giving me the strength to persevere, the patience to learn the finer details, and the wisdom to navigate through the obstacles presented during the final years of my PhD journey. I want to thank my advisor Dr. V. N. Bringi for his patience, for sharing with me a morsel of his vast knowledge in electromagnetic polarimetry, and most importantly, for his guidance and selfless support in helping me define, refine, and reach my ultimate goal of the PhD degree. He is the true embodiment of a mentor and academic advisor, and I will be forever grateful that he believed in me and took me on as his student. I would also like to thank Dr. Jose G. Colom-Ustariz for serving as my Co-advisor, although from a distance in Mayagüez, Puerto Rico, who was instrumental in making it possible for me to reach the end, by providing technical and at times, moral support. My sincere gratitude goes to the following members of my committee for your support: Dr. Paul W. Mielke, Dr. Anura Jayasumana, and Dr. Ali Pezeshki.

I would also like to thank Dr. Witold Krajewski for his invitation to the Iowa Flood Center as a visiting researcher during the IFloodS field campaign, and for the entire summer of 2014, which led to a great collaboration and eventual definition of the research presented herein as my dissertation topic. While in Iowa, Witek was a gracious host and mentor both academically and twice a week on the soccer pitch, teaching me the true meaning of a work-life balance. I'm also grateful to Dr. Anton Kruger for his technical support during my visit in Iowa, for his frank advice in presenting my ideas to others, and most importantly for volunteering his wife Truda to serve as guide/host to my family during their visit to Iowa City. A special thanks goes to my good friend and colleague, Dr. Kumar Vijay Mishra for making the initial recommendation and introduction to Witek, which led

to a productive CSU-UIowa collaboration and in the end, suggested I help them with the attenuation correction of the high spatio-temporal XPOL radars, resulting in the realization of my PhD dissertation topic. To Dr. Merhala Thurai, I am indebted to you for sharing your expertise in all things 2DVD, for your collaboration in several publications, and for providing support in the revision of this manuscript. Thank you Dr. Gwo-Jong Huang for helping me become a better Matlab programmer, by sharing your insight in visualizing radar signal processing techniques.

I am blessed to have a supportive family, and especially privileged to have my wife Chely keep us together, and financially support the household in the end so I could focus on completing the PhD degree. I want to thank my children, Gemma del Rocio and Diego Miguel, for your love, encouragement, and understanding while I was away from home for long hours doing research in the lab or in another state, and for the times when I was home but still thinking about the research. To my Mother, Dora Bustamante Gálvez who always encouraged me to follow my dreams, spent countless hours helping me with my homework, and listened to me when I was a child, I am eternally grateful for your love and guidance. I want to thank my brothers and sisters (Marcie, Benny, Vivian, David Eliseo, Belinda, Diana Levi, and Abbie) for your love, support, visits, and for always asking, "when are you going to graduate?" Special thanks to my extended families who gave me a place to decompress and prevent getting burned out: the U-18 Fort Collins Girls Soccer teams I helped coach; the staff and students at the CSU offices for Adult Learner and Veteran Services, the Native American Cultural Center, and El Centro; and all the volunteers at the Fort Collins Bike COOP. I dedicate this monumental accomplishment to you all, and so to my *Familia* I say, "WE DID IT *CARNALITOS!*"

This dissertation is typeset in L^AT_EX using a document class designed by Dr. Leif Anderson.

TABLE OF CONTENTS

Abstract	ii
Acknowledgements	iv
List of Tables	ix
List of Figures	x
Chapter 1. Introduction	1
1.1. Motivation and Background.....	1
1.2. Problem Statement	2
Chapter 2. Theoretical Background and Instrumentation.....	4
2.1. Dual-polarized Radar	5
2.1.1. The Weather Radar Equation	5
2.1.2. Backscatter of electromagnetic waves.....	7
2.2. Dual-Wavelength Reflectivity and Differential Reflectivity	10
2.3. Radar Platforms	12
2.3.1. University of Iowa XPOL Radar System.....	12
2.3.2. CSU-CHILL Dual Wavelength, Dual Polarization Radar	13
2.4. Ground-based instrumentation	14
Chapter 3. 2-D Video Disdrometer (2DVD) Scattering Simulations at X-band.....	19
3.1. Overview of the T-matrix Method.....	19
3.2. Use of global 2DVD scattering simulations to estimate a range of α & β coefficients for X-band attenuation correction procedure.....	19
3.3. Comparison of the DSDs obtained from the Global data set	22

3.4.	Scattering simulations from 1-minute DSDs of Global 2DVD locations.....	25
3.5.	Rain Rate algorithms derived from fits to scattering simulations.....	27
Chapter 4. Attenuation Correction using the iterative ZPHI Method and an improved		
	differential backscatter phase estimator	40
4.1.	Summary of Attenuation Correction Procedure.....	40
4.2.	Data processing steps for the attenuation-correction procedure	42
4.3.	Iterative FIR range filter design for X-band radars operating at high range	
	resolutions of $\Delta r=30m$	44
4.4.	Signal Processing steps of the two-stage FIR range filter for improved δ	
	estimation at X-band	52
Chapter 5. Results and comparative analyses of attenuation-corrected XPOL radar		
	data collected during the NASA GPM IFloodS field campaign	57
5.1.	Comparison of 2DVD scattering simulations to XPOL radar-derived relations	
	at X-band	59
5.2.	Attenuation Correction Applied to the University of Iowa XPOL Radars	61
5.3.	Comparison of XPOL-2 and XPOL-4 scans.....	66
5.4.	Rain rate comparisons between NASA rain gauges and radar-derived algorithms	
	from XPOL-4.....	67
5.5.	Application of two-stage FIR range filter to XPOL data collected during	
	IFloodS for improved differential backscatter phase " δ " estimation	73
Chapter 6. Dual Wavelength Ratios of Reflectivity & Differential Reflectivity.....		
6.1.	Description of Dual Wavelength Analysis Procedure	79

6.2. DWR-derived α and β coefficient variability with height in rain and mixed phase precipitation.....	82
6.2.1. Dual-Wavelength derived α coefficient in uniform Rain and Rain-Hail mixed phase regions.....	85
6.2.2. Dual-Wavelength Differential Reflectivity derived β coefficient in Rain only ..	87
6.2.3. Summary of variability in α & β coefficients using dual wavelength techniques	90
Chapter 7. Summary, Conclusions	94
Bibliography	96

LIST OF TABLES

2.1 University of Iowa XPOL Radar Parameters 13

2.2 CSU-CHILL dual-wavelength Polarimetric Radar Parameters 16

3.1 Summary of mean D_m , mean $\log_{10}(N_w)$, number of 1-minute DSD, and climatology for the various locations..... 25

3.2 Scattering Simulation Relations between $A_H - K_{DP}$ & $A_{DP} - K_{DP}$. Linear fit slope and y-intercept are summarized for the various locations. We should note the y-intercept values for both fits are very small and thus we assume the relations only by the slope, i.e., coefficient. 32

3.3 Rain Rate algorithms from 2DVD scattering simulations, summarized for the various locations. 34

5.1 Standard Deviations of Z_{H-cor} , Z_{DR-cor} , and K_{DP} for XPOL-2 & -4 in the overlap region enclosed by a 6-20 km range interval and a 1-5 km height of the comparative RHIs 67

6.1 Variability of Dual Wavelength derived α and β coefficients with Height..... 93

LIST OF FIGURES

2.1	University of Iowa XPOL-2 Radar during testing and installation of the elevation rotary joint, summer 2014. The RF transceiver, digital receiver and signal processing computer are housed in the white enclosure at the base of the antenna positioner.	13
2.2	CSU-CHILL Radar with dual-offset 8.5 m Gregorian antenna, as seen inside the inflatable radome. (image courtesy of CSU-CHILL National Radar Facility)	15
2.3	2DVD principle of operation diagram, adapted from Schoenhuber et al. (2008), Chapter 1 in [8].....	18
3.1	This global map highlights the locations of the 18 2DVDs, used in the recent study of the prevalence and large drops by Gatlin et al. (2015). The blue arrows indicate the locations of the subset of 4 instruments used in our analysis. Image courtesy of P. N. Gatlin and M. Thurai.....	20
3.2	NASA-GPM IFloodS instrumentation map. 2DVDs: SN25, etc. Radars: NPOL S-band, XPOL-2, XPOL-4, XPOL-3, and XPOL-5	21
3.3	One-minute DSD comparisons between the following 2DVD locations: (a,b) Gan, Huntsville (HSV), & Global datasets; (a,b) Gan, Iowa (IFloodS), & Global datasets; (e,f) Gan, Oklahoma (MC3E), & Global datasets. In the left column, mass-weighted mean diameter, D_m , of normalized gamma DSDs, and in the right column are the normalized intercept parameters, as $\log_{10}(N_w)$. Distributions are shown as % frequency of occurrence to easily compare the different locations, with varying numbers of observations.....	24

3.4	α coefficient vs. mass-weighted mean diameter, D_m , computed using the one-minute DSDs from each 2DVD located in (a) Huntsville, AL (HSV), (b) Iowa (IFloodS), (c) Maldives (Gan), and (d) Oklahoma (MC3E).....	27
3.5	β coefficient vs. mass-weighted mean diameter, D_m , computed using the one-minute DSDs from each 2DVD located in (a) HSV, (b) IFloodS, (c) Gan, and (d) MC3E	28
3.6	Global coefficients vs. mass-weighted mean diameter, computed using the one-minute DSDs from four 2DVDs located in different geographical locations. (a) α vs. D_m and (b) histogram of Global α ; (c) β vs. D_m and (d) histogram of Global β	29
3.7	The $A_H - K_{DP}$ relations, derived from scattering simulations using one-minute DSDs from four 2DVDs located in different geographic locations. (a) Huntsville, AL (HSV), (b) Iowa (IFloodS), (c) Maldives (Gan), and (d) Oklahoma (MC3E)..	30
3.8	The $A_{DP} - K_{DP}$ relations, derived from scattering simulations using one-minute DSDs from four 2DVDs located in different geographic locations. (a) Huntsville, AL (HSV), (b) Iowa (IFloodS), (c) Maldives (Gan), and (d) Oklahoma (MC3E)..	31
3.9	2DVD scattering simulations for the Global (a) $A_H - K_{DP}$ and (b) $A_{DP} - K_{DP}$ fits, derived from the combined (i.e., Global) DSDs from the four geographical locations.....	32
3.10	Rain Rate estimator using the $Z_{H-lin} - R$ fit to scattering simulations using one-minute DSDs from four 2DVDs located in different geographical locations. (a) Huntsville, AL (HSV), (b) Iowa (IFloodS), (c) Maldives (Gan), and (d) Oklahoma (MC3E).....	35

3.11	Rain Rate estimator $R(A_H)$ fit to scattering simulations using one-minute DSDs from four 2DVDs located in different geographical locations. (a) Huntsville, AL (HSV), (b) Iowa (IFloodS), (c) Maldives (Gan), and (d) Oklahoma (MC3E).	36
3.12	Rain Rate estimator $R(A_H, Z_{dr-linear})$ fit to scattering simulations using one-minute DSDs from four 2DVDs located in different geographical locations. (a) Huntsville, AL (HSV), (b) Iowa (IFloodS), (c) Maldives (Gan), and (d) Oklahoma (MC3E).	37
3.13	Rain Rate estimator $R(K_{DP})$ fit to scattering simulations using one-minute DSDs from four 2DVDs located in different geographical locations. (a) Huntsville, AL (HSV), (b) Iowa (IFloodS), (c) Maldives (Gan), and (d) Oklahoma (MC3E).	38
3.14	Global Rain Rate estimator algorithms fit to scattering simulations using one-minute DSDs from four 2DVD locations: (a) $R(A_H)$, (b) $R(A_H, Z_{dr-linear})$, (c) $R(K_{DP})$, and (d) $Z_{H-lin} - R$	39
4.1	Example range profile from XPOL-4 radar during IFloodS on June 12, 2013 at 233230 UTC, AZ=310°, EL=10.7°. In panels (a) and (b) 'corr' stands for attenuation-corrected values. In (c) 'filt' stands for FIR range filtered Φ_{DP} . Data mask value of 1 \equiv 'meteo' echoes and 0 \equiv 'non-meteo' echoes (in this beam the latter is receiver noise).	45
4.2	FIR30m-100 filter shows improvement in the ability to mitigate Mie backscattering between 20-24 km from the Φ_{DP} range profile through a convective storm. Radar data from a low elevation ($EL = 3^\circ$) XPOL-4 PPI scan, at $AZ = 287^\circ$, during IFloodS on 20130612-2327 UTC.	48

4.3	Magnitude response of the 40 th order 30 meter lowpass FIR Kaiser range filter, "FIR30M-40". The design criteria included a minimum attenuation of 25 dB at the stop-band, in this case at 421.5 m (or 0.071167 km ⁻¹).....	50
4.4	Magnitude response of the 100 th order 30 meter lowpass FIR Kaiser range filter, "FIR30M-100". The design criteria included a minimum attenuation of 25 dB at the stop-band, in this case at 1.050 km (or 0.02856 km ⁻¹).....	51
4.5	Comparion of δ suppression by the iterated filters using (a) 100 th order and (b) 40 th order Kaiser lowpass FIR filters. Note: (blue) raw Ψ_{DP} , (dashed) n^{th} iteration, (red) final iteration. A threshold of 3 ^o is assessed at each range bin, while a convergence factor of 0.001 ^o is used to stop the iteration process. The data is from the University of Iowa XPOL-4 radar ($\Delta r=30m$), collected during the IFloodS field experiment in the summer of 2013.....	51
4.6	Interpolating over the non-meteo "gaps" in range profile segments. We interpolate over these regions prior to beginning the iterative filtering procedure in the two-stage FIR process. Shown are (blue) raw Ψ_{DP} , smooth filtered Φ_{DP} using the (magenta) FIR30M-100 Kaiser filter, and (dashed) iterations.....	53
4.7	Range profile through a convective storm complex. In both, raw Ψ_{DP} is (blue); (a) is the Final iteratively filtered $\Phi_{DP-iter100}$ using the FIR30M-100 Kaiser filter (red), and in (b) the resulting two-stage smooth filtered $\Phi_{DP-2FIR}$ (magenta) after a single application of the FIR30M-40 Kaiser FIR to the Final iteratively filtered $\Phi_{DP-iter100}$ of (a). Radar data from Iowa XPOL-4 PPI at AZ=287 & EL=3, observed during IFloodS field campaign on 12 June 2013 at 23:27 UTC.....	54

4.8	<p>Estimated differential backscatter phase "δ" comparison between the proposed 2-stage FIR lowpass filter and the 75m FIR lowpass filter of Hubbert & Bringi (1995), H-B 95, when applied to the higher 30 m range resolution data of the XPOL-4. (a) Raw and filtered Φ_{DP} using both 2-stage FIR & FIR75m filters; (b) δ estimation, $r=16-24$ km; (c) δ vs. Z_{DR-cor} scatter plot for the $AZ = 287^\circ$ ray profile; (d) Histogram of $\delta > 4^\circ$ & $Z_{DR-cor} > 1$ dB for the ray profile. Radar data from Iowa XPOL-4 PPI at $AZ=287$ & $EL=3$, observed on 20130612-2327 UTC during the IFloodS field campaign.....</p>	56
5.1	<p>Intensity contour (in $\log_{10}(\#occurrences)$) plots of (a) A_{DP} vs A_H and (b) A_H vs K_{DP}. Data from XPOL-4 during IFloodS on 20130612-2107 to 20130613-0300 UTC. The overlay are disdrometer scattering simulation results, calculated for X-band from 4 days during IFloodS, for the same parameters.....</p>	60
5.2	<p>Intensity contour (in $\log_{10}(\#occurrences)$) plots of K_{DP} vs Z_H, A_H vs Z_H, and Z_{DR} vs Z_H. Data from XPOL-4 during IFloodS on 20130612-2107 to 20130613-0300 UTC. The overlay are disdrometer scattering simulation results, calculated for X-band from 4 days during IFloodS, for the same parameters. Plots (a), (c), and (e) are comparisons with uncorrected Z_H and Z_{DR}, while (b), (d), and (f) are with attenuation-corrected data.</p>	62
5.3	<p>PPI scans of (a) measured and (b) attenuation-corrected Z_H field from 12 June 2013 at 2334:00 UTC. The origin is at the XPOL-4 radar location. The plot axes are aligned with true North/South and West/East, shown with 10 km range rings. The dashed line indicates a vertical RHI profile at azimuth=10°.....</p>	63

5.4	RHI scans of measured (panels (a) & (b)) and attenuation-corrected (panels (c) & (d)) Z_H and Z_{DR} along the $AZ=310^\circ$, from XPOL-4 radar data during IFloodS on June 12, 2013 at 2332:30 UTC, at $AZ=310^\circ$. The dashed line indicates the ray profile at an $EL=10.7^\circ$	64
5.5	RHI scan of calculated K_{DP} from XPOL-4 radar during IFloodS on June 12, 2013 at 2332:30 UTC, at $AZ=310^\circ$. The colorbar units are in deg/km , and the dashed line indicates the $EL=10.7^\circ$ beam.	65
5.6	XPOL-2 to XPOL-4 radar intercomparison during IFloodS on June 12, 2013 at 23:18 & 23:19 UTC, respectively. Upper panels in the left column show RHIs from XPOL-2. (top) Z_{H-cor} , (middle) Z_{DR-cor} , (bottom) K_{DP} . Agreement in the attenuation-corrected values between the two radars is confirmed by congruency in their respective distributions (right column) in the overlap region enclosed by a 6-20 km range interval and a 1-5 km height, marked by the box in the top panel. Image adapted from [23]	68
5.7	Advection is visible as rain falls to the right in this photo taken during a recent Northern Colorado spring thunderstorm. When analyzing high resolution (30 m or less) radar derived rain rates, this effect suggests we cannot only select range bins directly above and adjacent to the rain gauges for comparison, but rather select the nearest neighbor bins with minimal errors to in situ rain rates measured on the ground. (Photo by M. B. Galvez, May 2, 2015).....	69
5.8	XPOL-4 Z_{H-cor} PPI plot of an inbound convective storm, highlighting the locations of 12 NASA dual tipping rain gauges within its 40 km unambiguous range. A blow-up is shown for Gauges 32 and 43, which are used to illustrate the nearest-neighbor selection criteria for range bins within a radius $r_{nn} < 500m$ of	

the gauges. The \square 's represent the starting azimuth of the range bin, and the \diamond 's the center of the bin. Radar data from XPOL-4 during IFloodS on 20130612-2334 UTC..... 71

5.9 Comparison of XPOL-4 nearest-neighbor range bins ($r_{nn} < 500m$) of radar-derived Rain rates to NASA dual tipping bucket Gauge 32 A&B. Rain Rates are computed using the $R(A_H)$ relation. Radar data from XPOL-4 during IFloodS on 20130612-13..... 73

5.10 Signal Extinction starting around 11.5 km W-SW of XPOL-4 during IFloodS field campaign on 20130612-2353 UTC. This resulted in the absence of received signal to compute radar-derived rain rates for comparison to NASA Gauges 43, 32, 29, 42, and 44, at or around this time..... 74

5.11 Comparison of XPOL-4 nearest-neighbor range bins ($r_{nn} < 500m$) of radar-derived Rain rates to NASA dual tipping bucket Gauge 32 A&B. Rain Rates are computed using the following relations: $Z_{H-lin} - R$ (top left), $R(A_H)$ (top right), $R(K_{DP})$ (bottom left), and $R(Z_{DR-lin}, A_H)$ (bottom right). Radar data from XPOL-4 during IFloodS on 20130612-2334 UTC, and shifted by +4 minutes to account for drop fall-time from a height of approximately 1.122 km..... 75

5.12 Comparison of XPOL-4 nearest-neighbor range bins ($r_{nn} < 500m$) of radar-derived Rain rates to NASA dual tipping bucket Gauge 43 A&B. Rain Rates are computed using the following relations: $Z_{H-lin} - R$ (top left), $R(A_H)$ (top right), $R(K_{DP})$ (bottom left), and $R(Z_{DR-lin}, A_H)$ (bottom right). Radar data from XPOL-4 during IFloodS on 20130612-2334 UTC, and shifted by +2 minutes to account for drop fall-time from a height of approximately 0.633 km..... 76

5.13	Application of the 75 m, 40th order Lowpass Butterworth FIR filter to a Φ_{DP} range profile through a convective storm, with evidence of Mie backscattering between 20-24 km. Radar data from a low elevation ($EL = 3^\circ$) XPOL-4 PPI scan, at $AZ = 287^\circ$, during IFloodS on 20130612-2327 UTC.....	77
5.14	Application of the 30m, 40th order Lowpass Kaiser FIR filter to a Φ_{DP} range profile through a convective storm, with evidence of Mie backscattering between 20-24 km. Radar data from a low elevation ($EL = 3^\circ$) XPOL-4 PPI scan, at $AZ = 287^\circ$, during IFloodS on 20130612-2327 UTC.	77
5.15	Application of the 30m, 100th order Lowpass Kaiser FIR filter to a Φ_{DP} range profile through a convective storm, with evidence of Mie backscattering between 20-24 km. Radar data from a low elevation ($EL = 3^\circ$) XPOL-4 PPI scan, at $AZ = 287^\circ$, during IFloodS on 20130612-2327 UTC.	78
6.1	CSU-CHILL RHI scans at $AZ=291^\circ$ for S-band: (a) Z_{H-S} and (b) Z_{DR-Ssm} , and at X-band: (c) Z_{H-X} & (d) Z_{DR-X} observed on 18 July 2013 at 2210 UTC. The black line shows the range profile at $EL=1.7^\circ$ to be analyzed for Dual wavelength attenuation correction at X-band.....	81
6.2	(a) Z_{H-S} RHI showing a convective storm with high reflectivities above 50 dBZ up to 8 km above ground; (c) Z_{H-X} showing attenuation starting at 25 km and beyond; (b) dual-wavelength ratio, $DWR = Z_{H-S} - Z_{H-X}$; (d) K_{DP-X} indicating heavy rain around 25 km, below 2 km height. Data collected from a CSU-CHILL S-X RHI scan, at $AZ = 291^\circ$, on 20130803-2142 UTC.	83
6.3	CSU-CHILL S/X-band range profiles from RHI scans at $AZ=291^\circ$ & $EL=1.7^\circ$, observed on 18 July 2013 at 22:10 UTC for (a) Z_{H-S} and Z_{H-X} vs Φ_{DP-X} ; (b)	

Z_{DR-S} and Z_{DR-X} vs ρ_{HV} ; (c) DWR_Z vs Φ_{DP-S} ; (d) ΔZ_{DR} vs Φ_{DP-X} . Estimated coefficients are, $\alpha = 0.375$ dB/deg; $\beta = 0.058$ dB/deg 84

6.4 α vs. height in Rain-only. (left) Vertical profiles, between range=25-30 km, of Z_{H-S} , Z_{DR-S} , A_{H-X} , and K_{DP-X} from a CHILL S-X RHI scan, at $AZ = 291^\circ$, on 20130803-2142 UTC; (top right) low Mie scatter signal over the range interval; (bottom right) α coefficient estimated, over the range interval between 25-30 km on a ray-by-ray basis, using the direct $\alpha = \Delta DWR / \Delta \Phi_{DP-X}$ method. This was determined to be a "Rain-only" region below 3 km in height, which was confirmed with $\alpha \approx 0.3dB/deg$ and the low Mie signal, as expected. 86

6.5 α vs. height in Rain-Hail mix. (left) Vertical profiles, between range=30-35 km, of Z_{H-S} , Z_{DR-S} , A_{H-X} , and K_{DP-X} from a CSU-CHILL S-X RHI scan, at $AZ = 291^\circ$, on 20130803-2142 UTC; (top right) high Mie scatter signal over the range interval; (bottom right) α coefficient estimated, over the range interval between 30-35 km on a ray-by-ray basis, using the direct $\alpha = \Delta DWR / \Delta \Phi_{DP-X}$ method. This was determined to be a "mixed-phase" column, which was confirmed with higher α 's and increasing Mie signal with height. The vertical profiles show near-zero Z_{DR-S} , with $Z_{H-S} \approx 50$ dBZ, and decreasing K_{DP-X} above 3 km, indicating spherical particles probably due to wet hail aloft. 88

6.6 (a) Z_{DR-S} RHI showing a convective storm with high differential reflectivities above 3 dB up to 5 km above ground; (c) Z_{DR-X} showing attenuation starting at 25 km and beyond; (b) Dual-wavelength Differential Reflectivity, DFR $Z_{DR} = Z_{DR-S} - Z_{DR-X}$; (d) K_{DP-X} indicating heavy rain around 25 km, below 2 km height. Data collected from a CHILL S-X RHI scan, at $AZ = 291^\circ$, on 20130803 21:42 UTC. 89

6.7 β vs. height in Rain-only. (left) Vertical profiles, between range=25-30 km, of Z_{H-S} , Z_{DR-S} , Z_{DR-X} , and K_{DP-X} from a CHILL S-X RHI scan, at $AZ = 291^\circ$, on 20130803-2142 UTC; (top right) $1dB < \Delta Z_{DR} < 3.5dB$ over the range interval and below 2 km height; (bottom right) β coefficient estimated, over the range interval between 25-30 km on a ray-by-ray basis, using the direct $\beta = \Delta Z_{DR} / \Delta \Phi_{DP-X}$ method. This was in a heavy "Rain-only" region below 3 km in height, which was confirmed with $\beta \approx 0.06dB/deg$ 91

6.8 Dual-wavelength derived α and β coefficients in Rain only. Radar data was collected by CSU-CHILL S/X band radar on 20130803 at 21:42, 21:53, and 22:03 UTC. 92

6.9 Dual-wavelength derived α coefficient in Rain-Hail mixed phase. (a) Radar data was collected by CSU-CHILL S/X band radar on 3 August 2013 at 21:42, 21:53, and 22:03 UTC. 93

CHAPTER 1

INTRODUCTION

1.1. MOTIVATION AND BACKGROUND

The backbone of weather monitoring, nowcasting and forecasting is the long range network of S-band Doppler, dual-polarization radars such as NEXRAD in the US and C-band counterparts in Europe, Japan and many other countries. The main driving force for dual-polarization upgrade to the NEXRAD network was based on improvements in rain fall estimation, improved hail detection and improved data quality by virtue of distinguishing between 'meteo' and non-meteo echoes. In the past, single polarized X-band radars were relegated to short range applications due to attenuation in moderate to severe weather. However, in the last decade the atmospheric community has seen widespread and successful application of X-band dual-polarization weather radars for measuring precipitation in the lowest two km of the troposphere. These X-band radars have the advantage of a smaller footprint, lower cost, and improved detection of hydrometeors due to increased range resolution. In recent years, the hydrology community began incorporating these radars in novel applications to study the spatio-temporal variability of rainfall from precipitation measurements near the ground, over watersheds of interest. The University of Iowa XPOL radar system is one of the first to be used as an X-band polarimetric radar network dedicated to hydrology studies. During the spring of 2013, the Iowa XPOL radars participated in NASA Global Precipitation Measurement (GPM) mission's first field campaign focused solely on hydrology studies, called the Iowa Flood Studies (IFloodS). A collaborative effort between Dr. Bringi's polarimetric radar lab at CSU and the Iowa Flood Center has led to the investigation of improvements upon the currently employed attenuation correction methods, with the intent of

obtaining more accurate radar-derived rain estimates for hydrological applications. X-band dual-polarized radars are also being used extensively in networked configuration to monitor severe weather events such as tornadic super cells (the network also provides for dual- or multiple Doppler derived wind fields). Such compact networks are also being investigated as gap-filler radars within the NEXRAD S-band network of long range radars covering the entire US. Another application is hydrometeor-type classification whereby fuzzy logic methods based on dual-polarized radar data are used to classify 'meteo' versus 'non-meteo' echoes and further classify 'meteo' echoes as due to rain, hail, snow etc. For all these applications, attenuation-correction is a crucial step which is the main topic of this dissertation.

1.2. PROBLEM STATEMENT

Weather radars operating in the 3.2 cm (X-band) regime can suffer from severe attenuation, particularly during heavy convective storms. This has led to the development of sophisticated algorithms for X-band radars to correct the meteorological observables for attenuation. Although X-band polarimetric weather radars have seen increased acceptance by the atmospheric and hydrology communities in recent years, the attenuation correction aspect remains relatively unexamined. This research studies the problem of correcting for precipitation-induced attenuation in X-band polarimetric weather radars with high spatio-temporal resolution for hydrological applications. The research objectives of this dissertation are focused in the following general areas:

- I. The first objective is to understand the role regional climatology has on the variability of 2DVD scattering simulations from a drop size distribution viewpoint, as well as its effects on the α and β coefficients, and lastly on derived rain rate algorithms, as compared to that derived from a global climatology.

- II. The second objective is to investigate the ZPHI method for attenuation correction of precipitation-induced attenuation in X-band polarimetric radars with high spatio-temporal resolution dedicated to hydrology studies of vast river basins and watersheds. We also study the effects of filtering techniques used to estimate the differential backscatter phase due to Mie scattering effects at X-band.
- III. The third objective is to evaluate performance of the attenuation correction and FIR filtering algorithms, applied to the high spatio-temporal data collected by the University of Iowa XPOL radars, during the hydrology-focused NASA-GPM mission, Iowa Flood Studies (or IFloodS) field campaign conducted in the spring of 2013.
- IV. For the final objective, we investigate dual-wavelength algorithms to directly estimate the α and β coefficients, of the $A_H = \alpha K_{DP}$ and $A_{DP} = \beta K_{DP}$ relations, to obtain the path integrated attenuation due to rain and wet ice or snow in the region near the melting layer. We analyze data from the dual-wavelength, dual-polarization CHILL S-/X-band Doppler weather radar to examine the coefficients and compare their variability as a function of height, where the hydrometeors are expected to go through a microphysical transformation as they fall, starting as snow or graupel/hail then melting into rain or a rain-hail mixture.

CHAPTER 2

THEORETICAL BACKGROUND AND INSTRUMENTATION

In this chapter, theoretical background is presented to introduce important concepts specific to dual-polarized (i.e., polarimetric) radar, like the weather radar equation and the backscatter of electromagnetic waves from precipitation. The backscatter cross-section is discussed with respect to the dielectric factor for water and ice, where it is dependent on wavelength and temperature. The backscatter cross-section is related to the radar reflectivity factor (i.e., $Z_{H,V}$) from horizontal and vertical polarizations, from which their difference provides detail about the drop shape, as the differential reflectivity, Z_{DR} . The absorption and scattering cross sections combined make up the extinction cross section, from which the specific attenuation in horizontal polarization, A_H , can be derived. The specific differential phase, K_{DP} , is also presented, as is the co-polar differential phase, from which we will derive several relations for attenuation correction procedures and radar-derived rain rate algorithms. Also included in this chapter is background related to dual-wavelength ratios (DWR) for reflectivity and differential reflectivity, that allow for direct derivation of attenuation correction coefficients (α & β), from differences in measured S-band to X-band wavelength radar moments.

We present the various key instruments used to investigate attenuation correction methods for X-band polarimetric radars with high spatio-temporal resolution, like the University of Iowa XPOL mobile radar platform, and the CSU-CHILL dual-wavelength dual-polarization weather radar (operating at both S- & X-bands). The two-dimensional video disdrometer, used to make *in situ* measurements of drop size distributions near to the ground is introduced, along with some key computations in estimating the rain rates and drop sizes

within the distribution measured. In essence, this chapter introduces the theoretical background and key instrumentation used to realize this research.

2.1. DUAL-POLARIZED RADAR

2.1.1. THE WEATHER RADAR EQUATION. The weather radar equation is a volumetric estimation of scattering from hydrometeors, rather than a point target equation. Here we estimate the effective reflectivity based on the drop size distribution (DSD) in a volume defined by the horizontal and vertical beam widths, as well as the radial range gate spacing.

Reflectivity, η , is the general radar term describing the volumetric backscatter cross-section per unit volume, and is calculated from the received complex signal envelope, derived from the discrete $I + jQ$ components at the output of the digital receiver. The reflectivity from meteorological backscatterers can be written as, $\eta = (\pi^5/\lambda^4)|k_w|^2 Z_e$. The equivalent reflectivity factor Z_e can be estimated from the received power, P_r , using the weather radar equation [1], shown here in a form for units commonly used by radar meteorologists,

$$(2.1) \quad P_r = \frac{\pi^5 10^{-17} P_t G^2 G_r \tau \theta_{3dB}^2 |k_w|^2 Z_e}{6.75 \times 10^{14} \ln 2 r^2 \lambda^2 l_r}$$

Receive power at range r , $P(r)$ is measured in mW , transmit power P_t in Watts, antenna and receiver gains, G and G_r are dimensionless, transmit pulse width τ in micro seconds (μs), antenna 3dB-beamwidth (H and V) θ_{3dB} in degrees, the dielectric factor of water $|k_w|^2 = |(\epsilon_r - 1)/(\epsilon_r + 2)|^2$ where ϵ_r is the complex relative permittivity of water, the range r is in kilometers, wavelength λ is in centimeters, and attenuation and receiver losses, l and l_r are dimensionless. The equivalent reflectivity factor Z_e is simply referred to, by radar meteorologists, as reflectivity for H,V polarizations at a range r , $Z_{h,v}(r)$ measured in units of $mm^6 m^{-3}$ in dBZ .

By rearranging the weather radar equation the reflectivity, at range r , for a given power measured at the H and V channel outputs of the digital receiver, can be expressed as,

$$(2.2) \quad Z_{h,v}(r) = \left(\frac{6.75 \times 2^{14} \ln 2}{\pi^5 10^{-17}} \right) \left(\frac{l_r G^2}{\tau \theta_{3dB}^2 |k_w|^2} \right) \left(\frac{\lambda^2(f_{NCO}) l^2}{P_t G_r(f_{NCO})} \right) r^2 P_{h,v}(r)$$

where the quantities within the parentheses represent parts of the radar system constant $C = C_k C_s C_d$, C_k is a numerical constant, C_s is dependent on static system hardware parameters including the antenna and receiver gains, and C_d is dependent on dynamic hardware parameters such as sampled transmit frequency and associated automatic frequency control parameters (i.e., f_{NCO}) set during the coherent-on-receive step. For example, the transmitted wavelength perturbations are due to the random variations in frequency output from the magnetron, and calculated as $\lambda(f_{NCO}) = c/(f_{NCO} + f_{STALO})$, where the STALO frequency is fixed, and the NCO frequency varies depending on the estimated frequency of the sampled transmit pulse. It is widely accepted in the radar meteorology community to represent Z using a logarithmic scale and written as,

$$(2.3) \quad Z_{h,v}(r) = 10 \log[C P_{h,v}(r) r^2] \quad [\text{in } dBZ]$$

and will henceforth be referred to in dBZ . The noise in a radar system is an important factor to keep track of, and so the radar equation can be rewritten as a signal-to-noise ratio (SNR) by dividing through by the noise power resulting in,

$$(2.4) \quad SNR = \frac{P_R}{N_R} = \frac{\lambda P_T G^2 \sigma}{(4\pi)^3 R^4 L(k T F_N) B}$$

where k is the Boltzmann's constant = 1.38×10^{-23} J/K, T is the nominal noise temperature (290K), F_N is the receiver system noise factor, B is the bandwidth at the antenna port, and L are the losses within the transmitter and receiver systems.

2.1.2. BACKSCATTER OF ELECTROMAGNETIC WAVES. The radar equation is based on the physics of electromagnetic propagation out from and returning to the antenna. The returning electromagnetic energy emitted by the scatterers (e.g., hydrometeors like rain drops, hail, snow, etc.) is commonly referred to as backscatter which has a radar cross section, $\sigma = 4\pi R^2 \lim_{R \rightarrow \infty} (\frac{P_r}{P_i})$, the limit of the ratio of received power to incident power as the range approaches infinity. There are three regions of scattering relating the radius a of a spherical backscatterer to the operating wavelength λ which are: Rayleigh, Mie or resonant, and the optical regions. The Rayleigh scattering region includes $a \ll \lambda$ (approximately $D < \lambda/16$), while the optical region is for $a \gg \lambda$. Between these two, the Mie solution to Maxwell's equations is applied.

Assuming the particle lies in the Rayleigh region, the backscattering cross section can be approximated by,

$$(2.5) \quad \sigma_b = \frac{\pi^5 |k_w|^2 D^6}{\lambda^4}$$

where $D = 2a$, and $|k_w|^2 = |(\epsilon_r - 1)/(\epsilon_r + 2)|^2$, is the dielectric factor for water and ϵ_r is the complex relative permittivity of the dielectric and can be expressed $\epsilon_r = \epsilon' + i\epsilon''$ (complex dielectric constant that is time dependent as $e^{-j\omega t}$). The real part of ϵ_r is the relative permittivity, while the imaginary part is the loss factor associated with wave attenuation. The dielectric factor k_w depends on the wavelength and temperature, where for example

at 0 C the refractive index $N = \sqrt{\epsilon_r}$, at $\lambda=3$ cm, is $7.089+2.907i$, while for dry ice it is $1.781+2.325 * 10^{-3}i$.

As an electromagnetic wave travels through precipitation it suffers power loss due to energy absorption and scattering by the dielectric hydrometeors. The absorption by hydrometeors depends on the absorption cross section σ_a that is due to power dissipated as heat, while the scattering cross section σ_s for small spheres can be related to the backscatter cross section as $\sigma_s = 2\sigma_b/3$. The total power lost due to absorption and scattering is defined as the extinction cross section, $\sigma_{ext} = \sigma_a + \sigma_s$, where

$$(2.6) \quad \sigma_a = \frac{\pi^2 D^3}{\lambda} \text{Im}(-k_w)$$

$$(2.7) \quad \sigma_s = \frac{2\pi^5 D^6}{3\lambda^4} |k_w|^2$$

Several fundamental relationships for the application of the weather radar equation are described in detail in [2]. The electromagnetic wave interaction with precipitation results in backscatter and attenuation, described by the radar backscatter cross section per unit volume η ($m^2 m^{-3}$), and the extinction cross section σ_{ext} (m^2). The radar reflectivity factor, z , is related to the precipitation backscatter cross section as,

$$(2.8) \quad z = \frac{\lambda^4}{\pi^5 |k_p|^2} \eta$$

$$(2.9) \quad = \frac{\lambda^4}{\pi^5 |k_p|^2} \int \sigma_p(D) N(D) dD$$

where λ is the wavelength, $|k_p|^2$ is the dielectric factor of hydrometeors, $\sigma_p(D)$ is the radar cross section for precipitation and $N(D)$ is the particle size distribution, or the number of particles per unit volume with sizes in the interval $[D, D + \Delta D]$. Also note, that z is reflectivity in linear units while Z is in dBZ (both $mm^6 m^{-3}$). For oblate and prolate

spheroids there exists a difference in the backscatter cross sections for horizontally and vertically polarized electromagnetic waves, and hence there is a difference in their observed radar reflectivities z_h and z_v , and their ratio is expressed as the differential reflectivity

$$(2.10) \quad Z_{DR} = 10 \log_{10} \frac{z_h}{z_v}.$$

The specific attenuation in horizontal polarization, A_H , can be expressed as a function of σ_{ext} and $N(D)$ as

$$(2.11) \quad A_H = 4.343 * 10^3 \int \sigma_{ext} N(D) dD$$

with units of $dBkm^{-1}$. The specific differential phase K_{DP} due to non-spherical precipitation observed as the phase difference between horizontal and vertical polarizations can be expressed as

$$(2.12) \quad K_{DP} = \frac{180\lambda}{\pi} \int \Re[f_h(D) - f_v(D)] N(D) dD$$

where f_h and f_v are the forward scattering amplitudes for the horizontal and vertical polarization states and \Re is the real part of a complex number. The observed co-polar phase is expressed as

$$(2.13) \quad \Psi_{DP} = 2 \int_{r_1}^{r_2} K_{DP}(r) dr + \delta$$

$$(2.14) \quad = \phi_{DP} + \delta$$

where δ is the differential backscatter phase and ϕ_{DP} is the differential propagation phase.

The specific differential attenuation, is defined as

$$(2.15) \quad A_{DP} = 8.686 * 10^3 \int \Im[f_h(D) - f_v(D)]N(D)dD$$

where \Im refers to the imaginary part of a complex number, and A_{DP} is in $dBkm^{-1}$.

2.2. DUAL-WAVELENGTH REFLECTIVITY AND DIFFERENTIAL REFLECTIVITY

Dual wavelength radars were originally motivated by the detection of hail and the estimation of liquid water content within a rain cell. The dual-wavelength reflectivity (DWR) can be defined as the ratio of intrinsic (i.e., attenuation-corrected) reflectivity at a long wavelength to the reflectivity at a short wavelength, and for this study we will use data from the CSU-CHILL dual-wavelength dual-polarization radar operating at S- and X-band ($\lambda=10$ cm & 3 cm, respectively) [3]. The basic idea behind the use of dual-wavelength reflectivity (DWR= Z_{H-S}/Z_{H-X}) of reflectivity for hail detection is to compare the simultaneous observations of a storm complex at two different wavelengths (i.e., S- and X-band), and taking advantage of the fact that in the presence of hail ($\geq 1cm$ in size) the X-band radar enters the Mie region before the S-band radar. The Mie scattering produced by hail at X-band manifests itself as a perturbation in the normally monotonic increase of DWR for rain-only events.

The advantage of having simultaneous reflectivity and differential reflectivity measurements at X and S band provides new avenues for investigating attenuation-correction algorithms at X-band. As previously mentioned, we take advantage of the S-band wavelength's immunity to Mie scattering effects (unless hail is very large, $\geq 5cm$) and assume the measured Z_H^S is equal to the intrinsic reflectivity $Z_H^{S,int}$, while at X-band intrinsic reflectivity $Z_H^{X,int}$ is equal to the measured Z_H^X plus the path integrated attenuation $A_H(2\Delta r)$ over a

range interval Δr . Assuming the intrinsic reflectivities from uniform echoes at S- and X-band are equal,

$$(2.16) \quad Z_H^S = Z_H^{S,int}$$

$$(2.17) \quad Z_H^X = Z_H^{X,int} - A_H(2\Delta r)$$

$$(2.18) \quad Z_H^S - Z_H^X = A_H(2\Delta r)$$

where the difference in measured reflectivities of the two wavelengths is the DWR, and over a range interval Δr , encompassing 'meteo' echoes, ΔDWR is equal to the total path integrated attenuation (PIA). The coefficient α of the $A_H = \alpha K_{DP}$ relation can be estimated if we take the ratio of ΔDWR to the change in differential propagation phase at X-band, $\Delta\phi_{DP}^X = (\phi_{DP}^X(r_0) - \phi_{DP}^X(r_1)) = 2 \int_{r_1}^{r_0} K_{DP}(s) ds$, as

$$(2.19) \quad \alpha = \frac{\Delta DWR}{\Delta\phi_{DP}^X}$$

where r_1 and r_0 are the range gates at the beginning and end of the storm complex, respectively.

Similarly, we can estimate the β coefficient in the $A_{DP} = \beta K_{DP}$ relation over the same 'meteo' echo range interval Δr , by taking the ratio of ΔDWR_{Zdr} to the change in differential propagation phase at X-band $\Delta\phi_{DP}^X$, as

$$(2.20) \quad \beta = \frac{\Delta DWR_{Zdr}}{\Delta\phi_{DP}^X}$$

where ΔDWR_{Zdr} is the difference in $Z_{DR}^S - Z_{DR}^X$, and making the assumption that the intrinsic differential reflectivities at S- and X-bands, $Z_{DR}^{S,int}$ and $Z_{DR}^{X,int}$, are equal.

2.3. RADAR PLATFORMS

During the course of this research, data from two different radar platforms are used. These platforms are both transportable Doppler weather radars, although with contrasting size scales, in particular: the first is a trailer-mounted radar node operating at X-band that can be readily configured into a network; and the second is at a national facility as a stand alone dual-wavelength, dual-polarization research radar operating at the S- and X-bands. Specifications and a brief description about each system are presented in the subsequent sections.

2.3.1. UNIVERSITY OF IOWA XPOL RADAR SYSTEM. The University of Iowa procured four X-band polarimetric Doppler weather radars (XPOL) to more accurately estimate rainfall at high spatio-temporal resolution [4, 5]. The XPOL radar node is a compact, transportable (i.e., trailer mounted), relatively low cost dual-polarization weather radar based on a modified marine radar, seen here in Figure 2.1. The four XPOLs were identically designed and manufactured by ProSensing, Inc., to the specifications listed in Table 2.1.

The XPOL radars can be set up to operate independently or in a complimentary networked environment, in various configurations (i.e., with 2, 3, or 4 nodes), to simultaneously observe rainfall near the ground, over a particular watershed of interest. Unlike most X-band polarimetric radar networks that are typically tower mounted at fixed locations, the transportability of the XPOL radar network allows for hydrological experiments of watersheds located in more diverse locations, that normally might not be studied. The Iowa polarimetric radar network was developed to serve the US hydrologic community to provide unique opportunities for hydrological studies requiring high spatio-temporal resolution, typically over a network of rain gauges and disdrometers for comparative analyses.

TABLE 2.1. University of Iowa XPOL Radar Parameters

Technical Characteristics	Description
Operating Frequency	9410 \pm 30 MHz
Transmitter	Magnetron, $P_t = 25$ kW
Transmit Mode	Simultaneous H-V transmit & receive
Antenna shape and size	1.8 m parabolic reflector
Polarization	Dual linear, H and V
Gain and 3-dB beam width	42 dBi, 1.4° (nom.)
Nominal max. Range, R_{max}	40 km
Range Resolution	Selectable 15 - 150 m
Range oversampling	Selectable 7.5 - 75 m
RF Receiver Gain	~ 33 dB
Cross-channel receiver isolation	> 50 dB

2.3.2. CSU-CHILL DUAL WAVELENGTH, DUAL POLARIZATION RADAR. The CSU-CHILL radar is a dual-wavelength polarimetric Doppler weather radar capable of operating at the S- and X-bands independently or simultaneously. The frequency variation is possible by replacing the antenna feedhorn with one of three transposable feeds: S-only, X-only, or both S



FIGURE 2.1. University of Iowa XPOL-2 Radar during testing and installation of the elevation rotary joint, summer 2014. The RF transceiver, digital receiver and signal processing computer are housed in the white enclosure at the base of the antenna positioner.

& X simultaneous configurations. Its 8.5 m parabolic dual-offset Gregorian reflector antenna [6] is mounted on an elevation over azimuth pedestal, encompassed by an inflatable radome, as seen in Figure 2.2. The S-band dual klystron-based transmitters and channel receivers are housed in a mobile trailer outside the radome, while the X-band single magnetron-based transceiver and data acquisition enclosures are installed directly onto the sub-reflector mounting structure. Table 2.2 highlights the key specifications of the CSU-CHILL dual-wavelength S/X-band radar; a more detailed list of system specifications can be found in [3].

The S/X-band radar provides a unique platform to observe meteorological events simultaneously at two wavelengths and also for developing dual-wavelength algorithms. One advantage of the collocated dual-wavelength polarimetric beams is that the S-band observations can serve as a reference for the attenuation-corrected measurements of reflectivity and differential reflectivity (CZ_H & CZ_{DR}) of the X-band data. A recent study by Matrosov et al [7] proposed using the CSU-CHILL dual-wavelength ratio to directly estimate the CHILL X-band radar signal attenuation coefficients (of the $A_H - K_{DP}$ and $A_{DP} - K_{DP}$ relations) directly from rain-only data. Although some pre-processing was necessary to match their beamwidths ($S = 1^\circ$, $X = 0.3^\circ$), the results of this study would not be so easily attainable using data from two independent S-band and X-band radars.

2.4. GROUND-BASED INSTRUMENTATION

The two-dimensional video distrometer (2DVD) is a precision instrument that makes *in situ* measurements of drop size distributions near to the ground. The advantages of using a 2DVD over traditional electromechanical disdrometers and rain gauges, that provide drop size distribution (DSD) and rain rate accumulations, are the addition of measured drop



FIGURE 2.2. CSU-CHILL Radar with dual-offset 8.5 m Gregorian antenna, as seen inside the inflatable radome. (image courtesy of CSU-CHILL National Radar Facility)

shapes (from two orthogonal views) and their fall velocities. We refer to Schoenhuber et al. (2008) in Chapter 1 of [8], for the following summarized principle of operation. Figure 2.3, illustrates a diagram highlighting the principle of operation diagram of a 2DVD that consists of two orthogonal optical systems, with horizontally-aligned line scan cameras illuminated by a background light source. The optics of the background illumination system focus an intense collimated light plane, from a standard halogen bulb, onto a certain number of camera pixels that when "shadowed," indicate the width of a particle in the 10 cm x 10 cm Virtual

TABLE 2.2. CSU-CHILL dual-wavelength Polarimetric Radar Parameters

Parameter	S-band	X-band
Operating Frequency	2725 MHz	9410 ± 30 MHz
Transmitters	Dual Klystron	Single Magnetron
Peak Output Power	1 MW per CH	25 kW, 12 kW per CH
Transmit modes	Single-pol, simultaneous, alternating H-V	Simultaneous H-V
Antenna type	8.5 m dual-offset Gregorian parabolic	shared
Polarization	Linear H and V	Linear H and V
Gain and 3-dB beam width	43 dBi, 1.0°	53 dBi, 0.3°
Sensitivity	-10 dBZ, 30 km	-10 dBZ, 30 km
Noise Figure	3.4 dB	4.0 dB
Dynamic Range	80 dB	90 dB
Range Resolution	150 m	150 m
Range Sampling	30 - 150 m	1.5-192 m
Data Products	$Z, Z_{DR}, \rho_{HV}, \phi_{DP}, K_{DP}, V, W, SNR, NCP$	Same as S-band

Measuring Area. The orthogonal collimated light planes are separated by a distance of 6-7 mm, which allow for direct measurement of the time it takes a particle to break both planes, from which a fall velocity can be computed. The cameras recognize each particle line by line, and are then disassembled into slices of the front and side contours, stored for later reconstruction of individual hydrometeors (or frozen particles).

Approximately every $18\mu s$, both cameras sample the measurement area for any occlusions of the the light plane, by particles. The light intensity is represented by an 8-bit A/D conversion (0 to 255 levels) for each of the 630 pixels of the line scan camera, where each pixel has a resolution below 0.2 mm. Refer to Schoenhuber et al. (2008) in [8] for details regarding measurement errors based on particle size and the 50% relative threshold of pixel occlusion. Rainfall rate is yielded when dividing the rain amount by the corresponding time interval as,

$$(2.21) \quad R = 3600 \frac{1}{\Delta t} \sum_{i=1}^n \frac{V_i}{A_i}, \quad \left[\frac{mm}{h} \right],$$

where Δt is the user-selectable integration time interval [$> 15s$], i is drop number, n is the total number of fully visible drops measured in time interval Δt , V_i is the volume of i^{th} drop [mm^3], and A_i is the effective measuring area for the i^{th} drop [mm^2]. The DSDs are calculated using information of the equivolume sphere diameter of raindrops, time stamps, sizes of their effective measuring areas, their fall velocities, user-defined integration interval and size class width. The DSD is the number of drops per unit volume per unit size, where a particular size class is determined as,

$$(2.22) \quad N(D_i) = \frac{1}{\Delta t \Delta D} \sum_{j=1}^{m_i} \frac{1}{A_j v_j}, \quad \left[\frac{1}{m^3 mm} \right],$$

where Δt is the user-selectable integration time interval [$> 15s$], i denotes a particular drop size class, j denotes particular drop within size class i and time interval Δt , m_i is the number of drops within size class i and time interval Δt , D_i is the mean diameter of class i [mm], ΔD the width of drop size class [typically 0.25 mm], A_j is the effective measuring area for the j^{th} drop [m^2], and finally v_i the fall velocity of the j^{th} drop [m/s]. For a more detailed overview of the 2DVD, refer to [8, 9]. There are at least two important parameters that describe the $N(D)$. First is the mass-weighted mean drop diameter (D_m) defined as the ratio of the 4th to 3rd moments of the $N(D)$. The second is the normalized intercept parameter (N_w) defined (excluding constants) as the ratio of the rain water content to D_m^4 . These two parameters (D_m and N_w) can be defined for any measured $N(D)$. The N_w is the same as the intercept parameter (N_0) of an equivalent exponentially-shaped distribution that has the same D_m and rain water content as the measured $N(D)$. Note that the Marshall-Palmer exponential DSD keeps $N_0=8,000 \text{ mm}^{-1} \text{ m}^{-3}$ with D_m being expressed as a power law with rain rate, R .

Following are the equations of D_m and N_w with respect to the drop size distribution, $N(D)$,

$$(2.23) \quad D_m = \frac{\int D^4 N(D) dD}{\int D^3 N(D) dD}$$

$$(2.24) \quad N_w = \frac{4^4}{\pi \rho_w} \left[\frac{10^3 W}{D_m^4} \right], mm^{-1} m^{-3},$$

where ρ_w is the water density ($1 g cm^{-3}$), and W is the water content in $g m^{-3}$

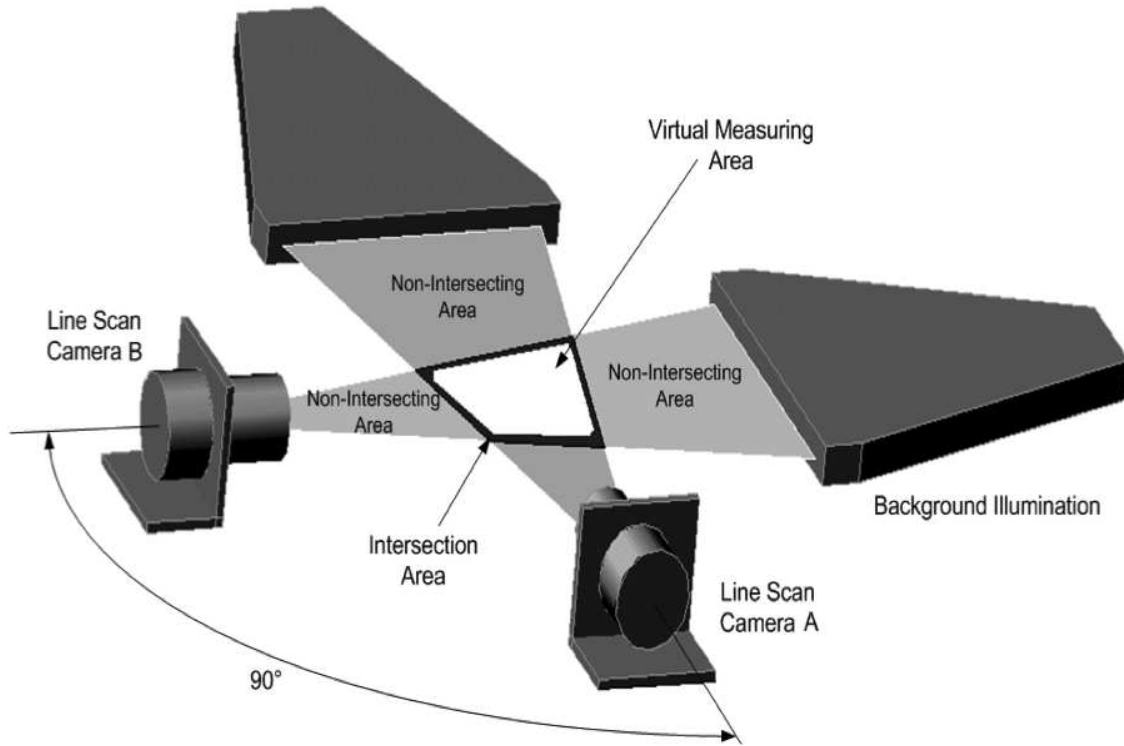


FIGURE 2.3. 2DVD principle of operation diagram, adapted from Schoenhuber et al. (2008), Chapter 1 in [8]

CHAPTER 3

2-D VIDEO DISDROMETER (2DVD) SCATTERING

SIMULATIONS AT X-BAND

3.1. OVERVIEW OF THE T-MATRIX METHOD

The transition, or T-matrix method is a numerical technique for calculating the scattering from spheroids, first developed by [10], also referred to as the extended boundary condition method. We summarize the description of the T-matrix, and defer details of the vector spherical harmonic analysis and solution for the transition matrix presented in the appendices (2,3,4) of the book *Polarimetric Doppler Weather Radar: Principles and applications*, by Bringi and Chandrasekar (2001). In essence, a plane wave that is incident on the particle is expanded in vector spherical harmonics (like a Fourier series) with known coefficients of the plane wave, while the scattered field can also be expanded in vector spherical harmonics, with unknown coefficients. The scattering coefficients and the incident plane wave coefficients are related by the T-matrix, and dependent on the shape of the particle and its dielectric constant, whereby we can determine the unknown scattering coefficients and incidentally the backscattered field.

3.2. USE OF GLOBAL 2DVD SCATTERING SIMULATIONS TO ESTIMATE A RANGE OF α & β COEFFICIENTS FOR X-BAND ATTENUATION CORRECTION PROCEDURE

The data used for the scattering calculations is a subset of the global 2DVD datasets used for a recent study on the prevalence and occurrence of large drops by [11]. The dataset compiled consisted of a large and diverse set of measurements from 18 locations around the globe. A map of these locations is given in Figures 3.1. Indicated on it with blue arrows are

four locations used in the current simulations, namely, (i) Huntsville, Alabama, (ii) Iowa, (iii) Oklahoma, and (iv) Gan near Maldives. The first three are continental US locations and the last one is a tropical oceanic location in the Indian ocean.

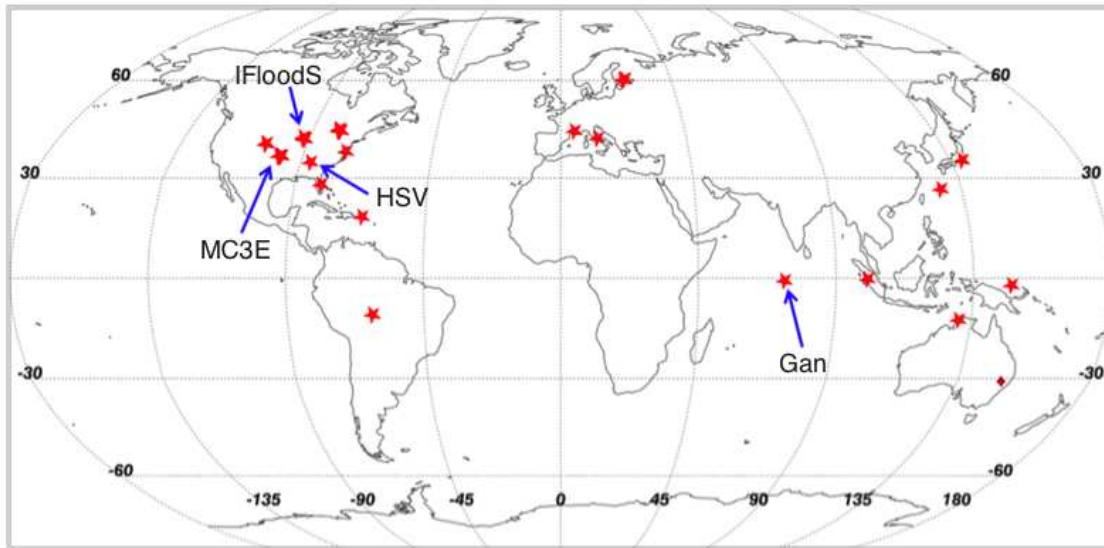


FIGURE 3.1. This global map highlights the locations of the 18 2DVDs, used in the recent study of the prevalence and large drops by Gatlin et al. (2015). The blue arrows indicate the locations of the subset of 4 instruments used in our analysis. Image courtesy of P. N. Gatlin and M. Thurai.

Following are brief descriptions of the locations and associated field campaigns for each of the four 2DVD sites selected for our analysis:

- I. Huntsville, Alabama (HSV): The 2DVD (SN16) provided by Colorado State University was installed at a site belonging to the University of Alabama, Huntsville, as part of a long-term collaboration. From the full dataset, 7,520 1-minute DSDs from 37 different events over a 10-month period were extracted. Analyses of rain DSD characteristics using these data have been previously published by [12], and [13].
- II. Iowa (various locations, IFloodS): The 2DVD data from Iowa were taken during the NASA-GPM ground validation campaign, the Iowa Flood Studies (IFloodS; [14]),

which was conducted in eastern Iowa from May to June 2013. This was the first NASA-GPM campaign focused on hydrology studies theory-radars and featured several radars as well as many ground-based instruments including six 2DVDs for in situ observations. The six units were separated by tens of kilometers (see Figure 3.2). Data from all six units from four separate events have been utilized in the current study.

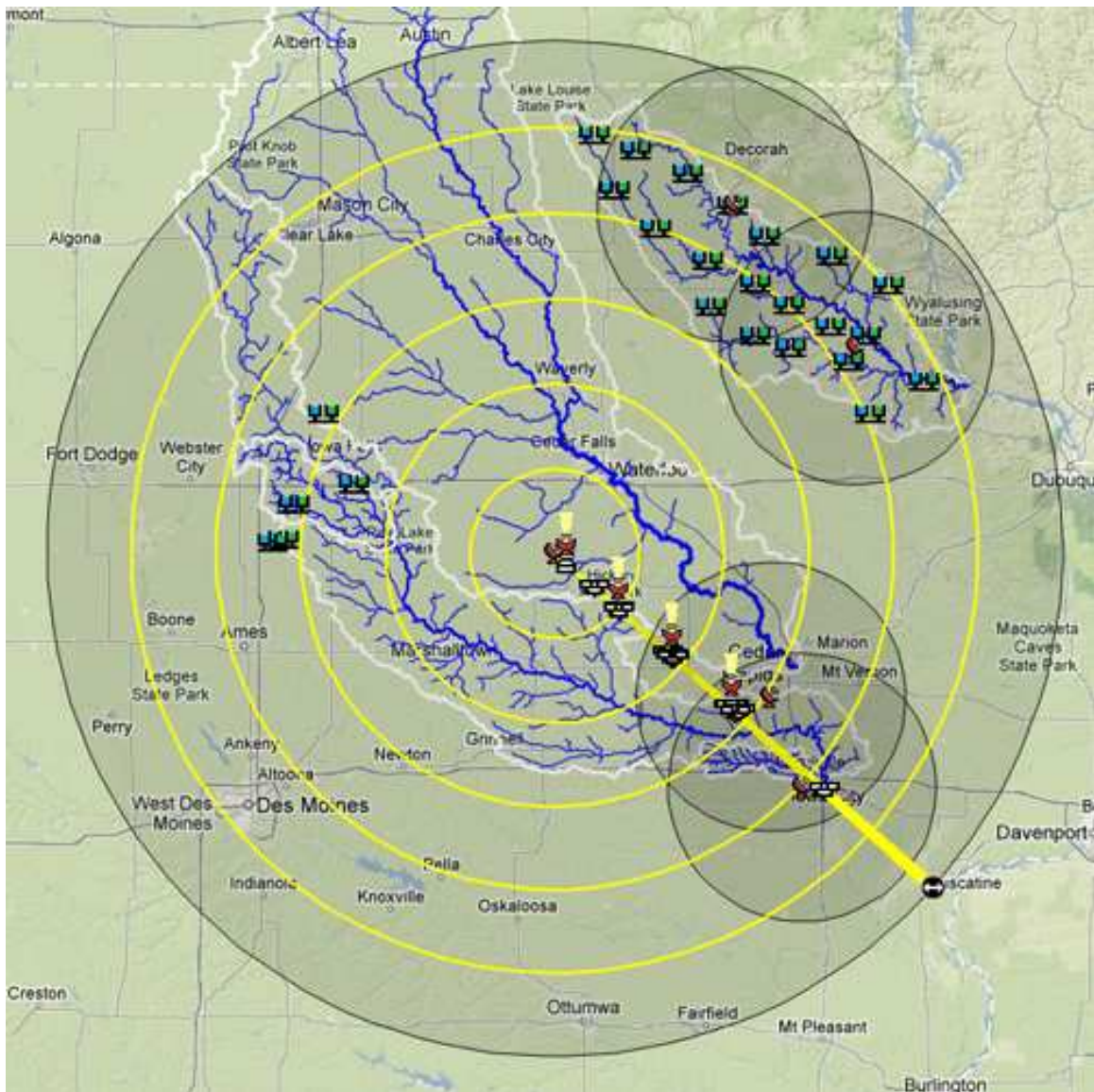


FIGURE 3.2. NASA-GPM IFloodS instrumentation map. 2DVDs: SN25, etc. Radars: NPOL S-band, XPOL-2, XPOL-4, XPOL-3, and XPOL-5

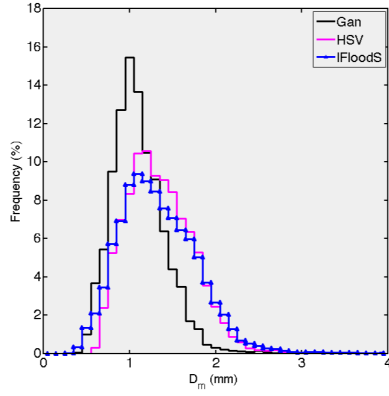
- III. Oklahoma (MC3E): The 2DVD data from Oklahoma were taken from the Mid-latitude Continental Convective Clouds Experiment (MC3E; [15]) conducted in south-central Oklahoma during the April to May 2011 period. This campaign also involved many radars and ground instruments, including seven 2DVDs. Data from several events from all seven units from this campaign were utilized in this study.
- IV. Gan near Maldives (Gan): Whilst the above three represent mid-latitude, continental climates, the fourth location considered in our study is an equatorial, location, situated in the Indian ocean. Data used in this study were obtained from one 2DVD only but over a 3.5 month period as part of the DYNAMO ((Dynamics of the Madden-Julian Oscillation) field campaign (for example, [16]). Extensive analysis of the 3.5 month 2DVD dataset from this campaign has been recently completed [17]. One of the interesting and important findings from this study is that the DSD characteristics were very similar to those derived from another equatorial, oceanic location in the Western Pacific, namely, Manus island. In both cases, the study found that DSDs were characterized by small to medium drop diameters compared with continental DSDs.

3.3. COMPARISON OF THE DSDS OBTAINED FROM THE GLOBAL DATA SET

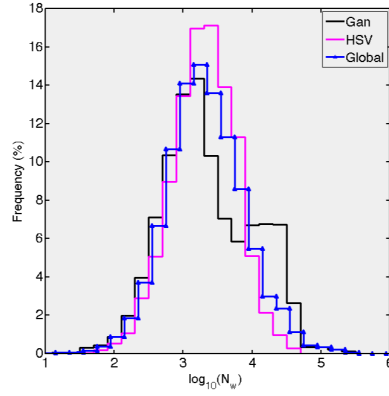
The computations presented herein, were obtained using 1-minute drop size distributions (DSDs) from the four geographic locations, both independently and in a global sense. In Figure 3.3, we illustrate the histograms of the mass-weighted mean diameters, D_m , and the corresponding normalized intercept parameter, N_w , of the DSDs for each location as compared to that of Gan and the Global dataset. From the D_m histograms in (a), (c), and (d) note that the following points can be made, (i) the Gan DSDs are the most distinct with

a skew toward smaller drops and a tail showing fewer large drops, as expected for tropical environments, (ii) the Global distribution is biased toward the DSDs of Huntsville, Alabama (HSV) as this was a longer-term experiment where more diverse rain events were observed, (iii) the distribution of MC3E followed the Global trend, as would be expected in continental mid-latitudes in spring time, and (iv) the IFloodS D_m distribution is shifted to the right due to the increased samples of larger drops observed during convective rain events during the campaign. In Table 3.1, we summarize the mean and standard deviation of the D_m distributions for the four locations, and see that the smallest mean and standard deviations were measured in Gan, the largest mean D_m in IFloodS, with the largest spread (std. dev.= 0.504 mm) seen in MC3E.

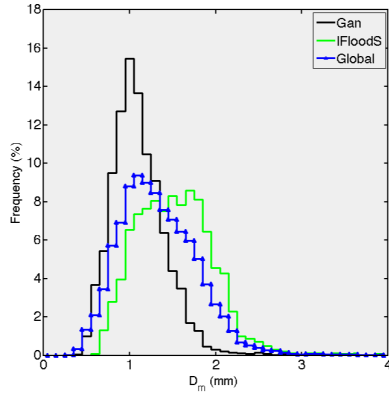
Referring to the histograms (in b,d,f) and summarized statistics in the Table 3.1, one can say almost all the normalized intercept parameters, N_w , are close to the Marshall-Palmer (M-P) normalized intercept parameter for an exponential distribution of $N_0 = 3.9031$ (i.e., $8,000mm^{-1}m^{-3}$), [18]. We should also note however, that the N_w for IFloodS is significantly smaller than M-P, which is caused by the increased number of larger drops due to the more convective nature of the dataset. It should be clear we are not discussing the actual shape of the distributions (i.e., in terms of gamma parameters), but recognizing the DSD shapes can be different, but still have intercept parameters near the exponential distribution of M-P. It should also be noted that we are not separating the D_m 's based on rain types, as we note the dominant convective events in IFloodS, while the other locations are composed of mixed rain types primarily of stratiform and some convective events.



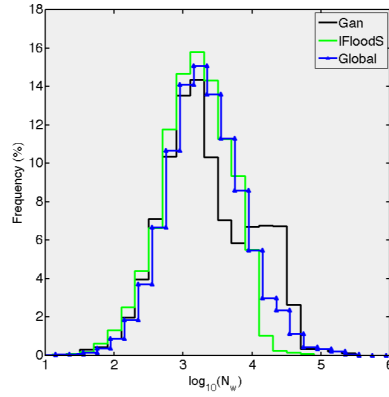
(a) Gan, HSV, Global DSDs



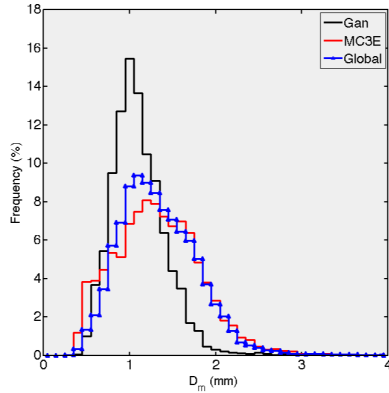
(b) Gan, HSV, Global $\log_{10}(N_w)$



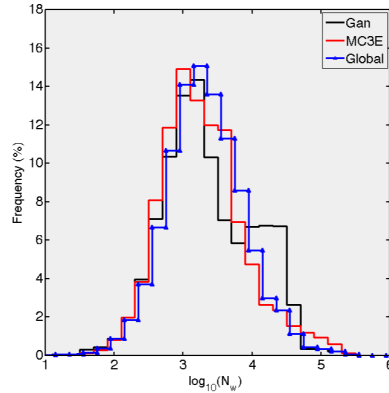
(c) Gan, IFloodS, Global DSDs



(d) Gan, IFloodS, Global $\log_{10}(N_w)$



(e) Gan, MC3E, Global DSDs



(f) Gan, MC3E, Global $\log_{10}(N_w)$

FIGURE 3.3. One-minute DSD comparisons between the following 2DVD locations: (a,b) Gan, Huntsville (HSV), & Global datasets; (a,b) Gan, Iowa (IFloodS), & Global datasets; (e,f) Gan, Oklahoma (MC3E), & Global datasets. In the left column, mass-weighted mean diameter, D_m , of normalized gamma DSDs, and in the right column are the normalized intercept parameters, as $\log_{10}(N_w)$. Distributions are shown as % frequency of occurrence to easily compare the different locations, with varying numbers of observations.

TABLE 3.1. Summary of mean D_m , mean $\log_{10}(N_w)$, number of 1-minute DSD, and climatology for the various locations.

2DVD Location (# instruments)	D_m (mm)		$\log_{10}(N_w)$	1-min DSDs	Climatology	
	mean	std. dev.	mean	# samples	type,	latitude
HSV (1)	1.404	0.391	3.6259	6,876	continental,	mid-latitude
IFloodS (6)	1.577	0.4478	3.5428	6,466	continental,	mid-latitude
MC3E (7)	1.376	0.504	3.9187	7,863	continental,	mid-latitude
Gan (1)	1.156	0.359	3.9397	6,271	oceanic,	equatorial
Global (15)	1.386	0.454	3.7907	27,476		

3.4. SCATTERING SIMULATIONS FROM 1-MINUTE DSDS OF GLOBAL 2DVD LOCATIONS

Next we consider the coefficients α and β of the $A_H - K_{DP}$ and $A_{DP} - K_{DP}$ relations from the 2DVD scattering simulations, which are key components used in the ZPHI method, with Φ_{DP} constraint, for attenuation correction of measured Z_H and Z_{DR} (we summarize the ZPHI method later in chapter 4). There are two trends observed at the four locations in the $\alpha - D_m$ relations seen in Figure 3.4, firstly, for D_m values between 1.5 mm to about 2.2 mm, α has a distinct dependence on D_m that sharply increases from $0.22dB/^\circ$ before stabilizing near a value around $0.32 dB/^\circ$, at the larger $D_m > 2mm$. Conversely, for small D_m values less than 1.5 mm, α tends to start high, then decrease to a value of $0.22dB/^\circ$, for an overall "U-shaped" curve, which is consistent with the X-band results presented by [19]. In Figure 3.5, it is more clear that the variation in β is more dependent on D_m , with less scatter, mainly due to $A_{DP} = A_H - A_V$ and $K_{DP} = d\Phi_{DP}/dr$, being differential quantities of the H-V polarization components, thus the correlation. In Figure 3.6, we see the Global relations of $\alpha - D_m$ and $\beta - D_m$, with more scatter present in α due to the variability in rain types at the various locations, but referring to the histograms, still within the values reported by [20], for temperature-averaged power-law fits of $\alpha = 0.233dB/^\circ$ and $\beta = 0.033dB/^\circ$ at an X-band frequency of 9.3 GHz. From the scattering simulations comparing the coefficients to the mass-weighted mean diameters, it is apparent that both α and β can take different values

over the range of D_m 's, while in the Iterative ZPHI method, with Φ_{DP} constraint, we find a single *optimal* coefficient for the entire beam. This can lead to over/under estimation of the attenuation (both A_H and A_{DP}) along the beam, but can be improved by optimizing α and β over shorter range intervals (i.e., dividing the full beam into segments), then applying the estimation procedure over each interval, as proposed by [21]. The histograms for the Global dataset are useful for providing a range of values for α and β , necessary for setting the interval of *optimal* coefficient values in the iterative ZPHI method as proposed by [22], for a large number of optimized beams.

In the attenuation correction procedure of the ZPHI method, we typically determine the α & β coefficients from the slopes in the $A_H - K_{DP}$ & $A_{DP} - K_{DP}$ relations of 2DVD scattering simulations, and typically do not compare their relation to the mass-weighted mean diameters, D_m , as previously described. We should note that the slopes of $\alpha \approx 0.30$ from the mean fit in the $A_H - K_{DP}$ relations, as illustrated in Figures 3.7 (and summarized in Table 3.2), are not exactly equal to the mode Global $\alpha = 0.25$ in the $\alpha - D_m$ histogram (in Fig. 3.6). The variability in D_m is embedded in the A_H data, so we optimize the α coefficient in the ZPHI method to account for this variability and can tend to have higher values. In Figures 3.8, we see more scatter in the $A_{DP} - K_{DP}$ relations, even though this ratio is derived from two differential quantities, which is apparent in the variability in β values, summarized in Table 3.2 and in the absence of a distinct mode in the Global β vs. D_m histogram (Fig. 3.6(b)). Figure 3.9, illustrates these $A_H - K_{DP}$ & $A_{DP} - K_{DP}$ relations from scattering simulations using the Global dataset, which are in good agreement with the relations of the independent locations.

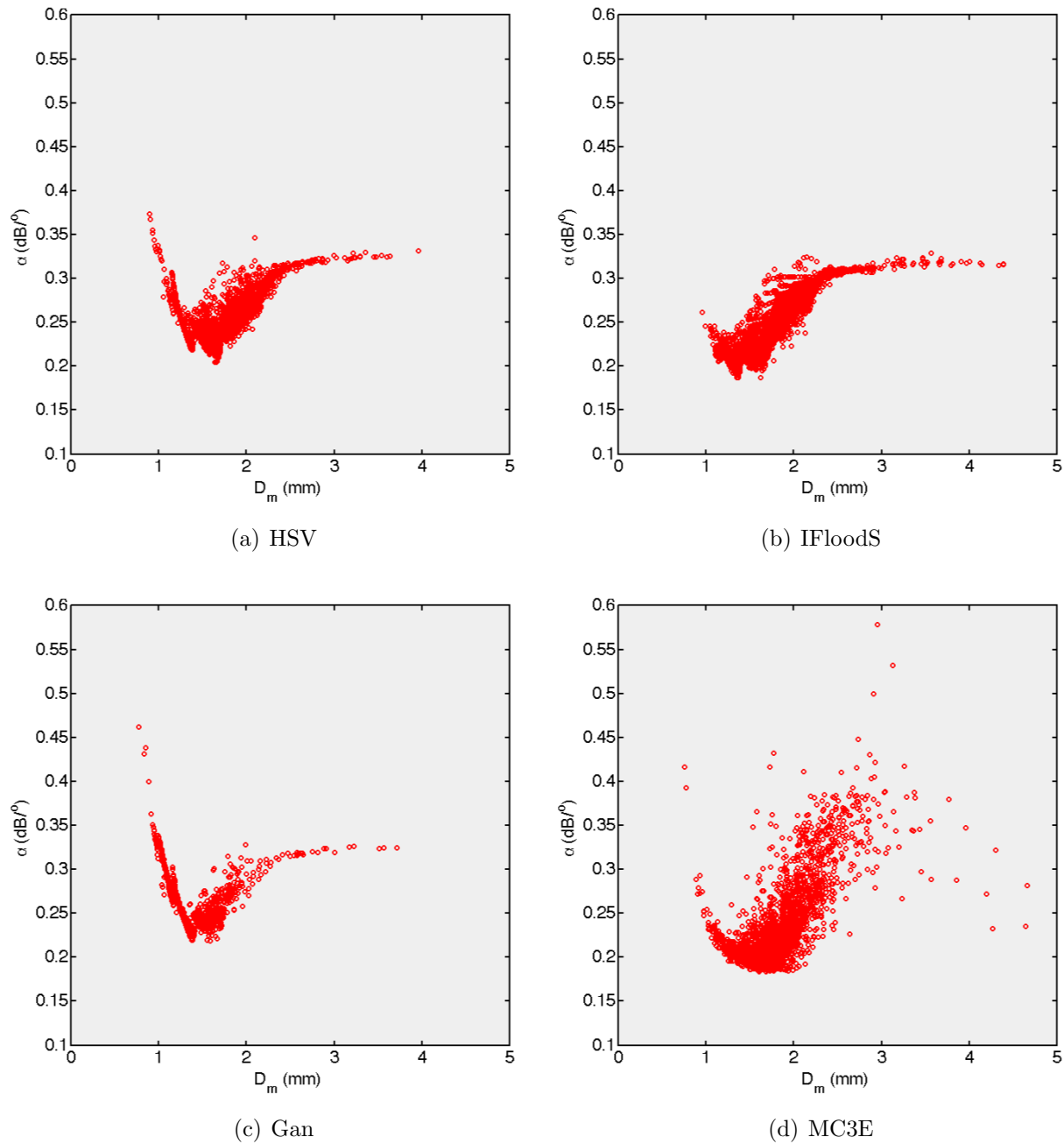


FIGURE 3.4. α coefficient vs. mass-weighted mean diameter, D_m , computed using the one-minute DSDs from each 2DVD located in (a) Huntsville, AL (HSV), (b) Iowa (IFloodS), (c) Maldives (Gan), and (d) Oklahoma (MC3E)

3.5. RAIN RATE ALGORITHMS DERIVED FROM FITS TO SCATTERING SIMULATIONS

Various radar-derived rain rate algorithms, summarized in Table 3.3, can be derived by applying a power law fit to the scattering simulations between the 2DVD-derived rain rates

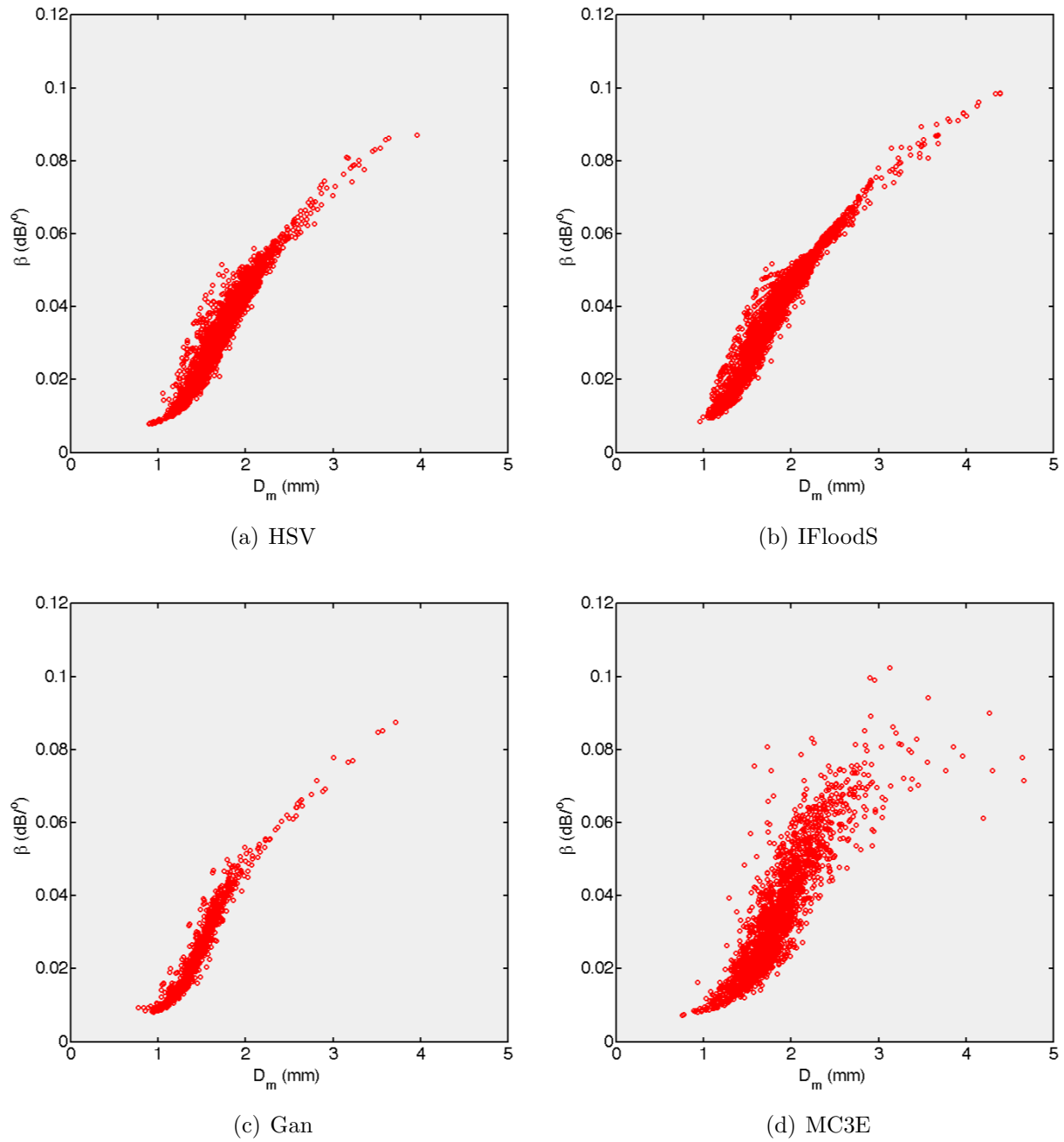


FIGURE 3.5. β coefficient vs. mass-weighted mean diameter, D_m , computed using the one-minute DSDs from each 2DVD located in (a) HSV, (b) IFloodS, (c) Gan, and (d) MC3E

to the derived reflectivity, Z_H , specific attenuation, A_H , differential reflectivity, Z_{DR} , and the specific differential phase, K_{DP} , for instance. Although the relations are not perfect, the

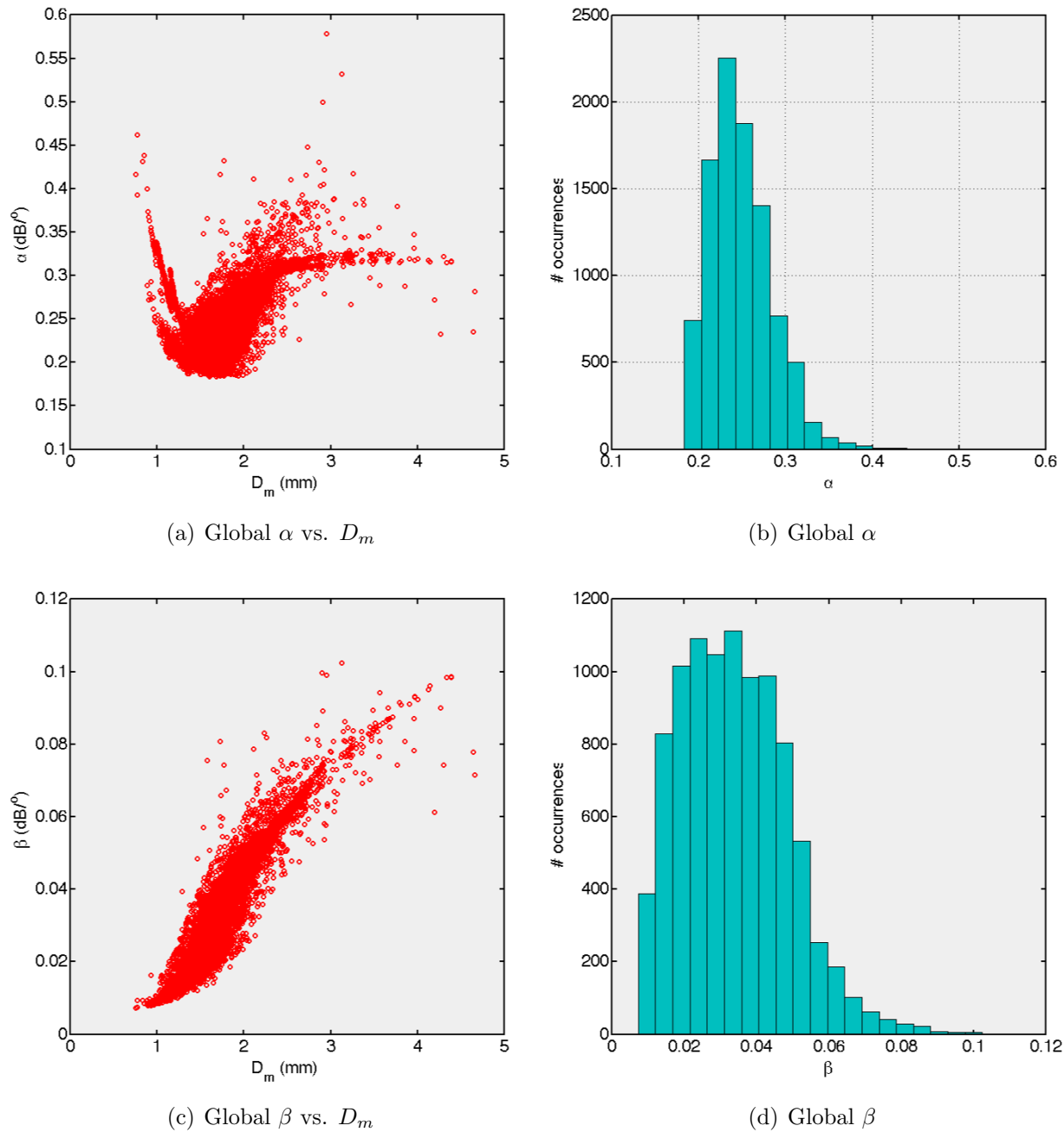
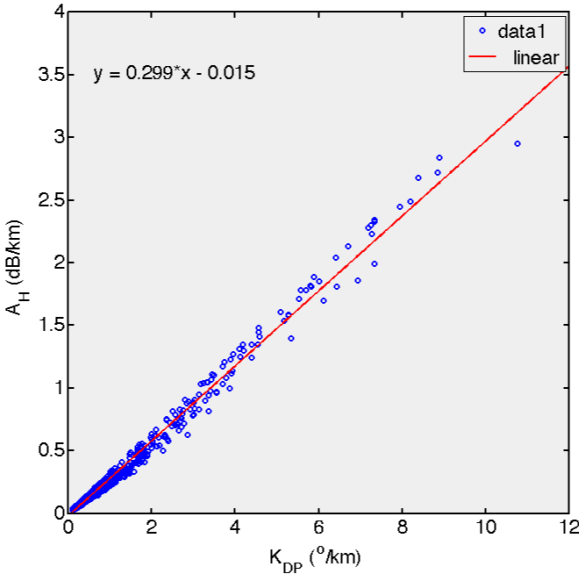
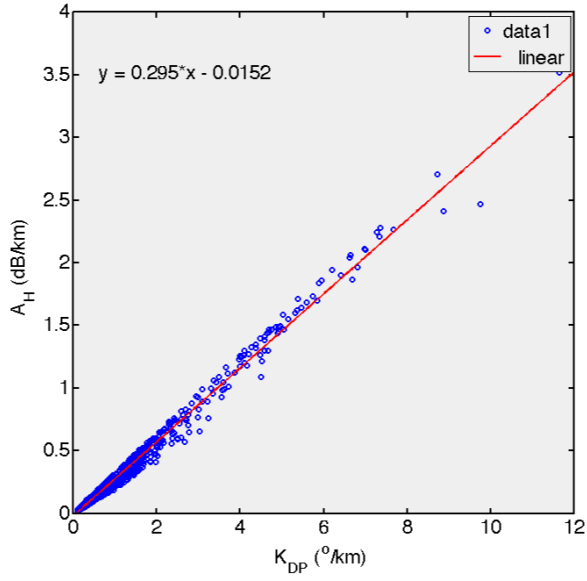


FIGURE 3.6. Global coefficients vs. mass-weighted mean diameter, computed using the one-minute DSDs from four 2DVDs located in different geographical locations. (a) α vs. D_m and (b) histogram of Global α ; (c) β vs. D_m and (d) histogram of Global β

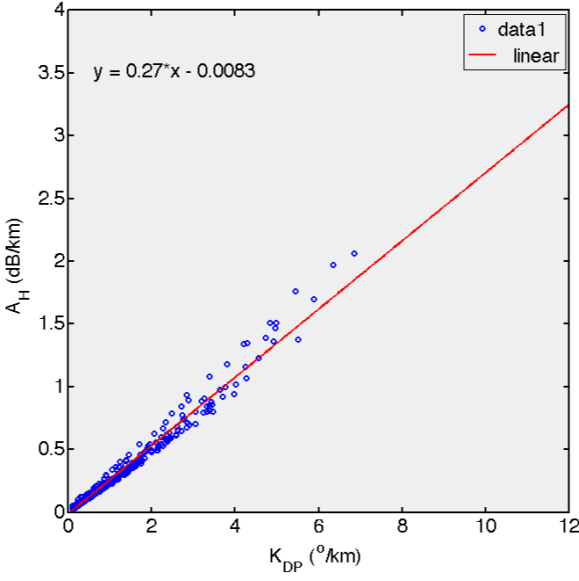
reason the power law fit is so ubiquitous in all of these relationships (e.g., $Z - R$, $R - K_{DP}$, $R - A_H$, and $R - A_H - Z_{DR-linear}$), is that, for example, the A_H is proportional to the 4th moment



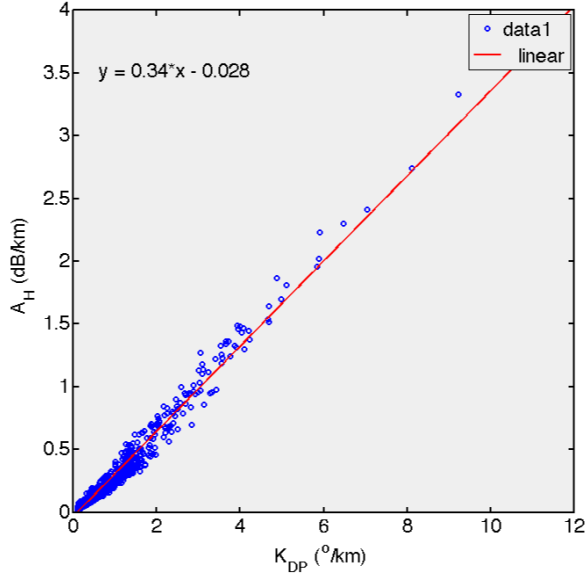
(a) HSV



(b) IFloodS



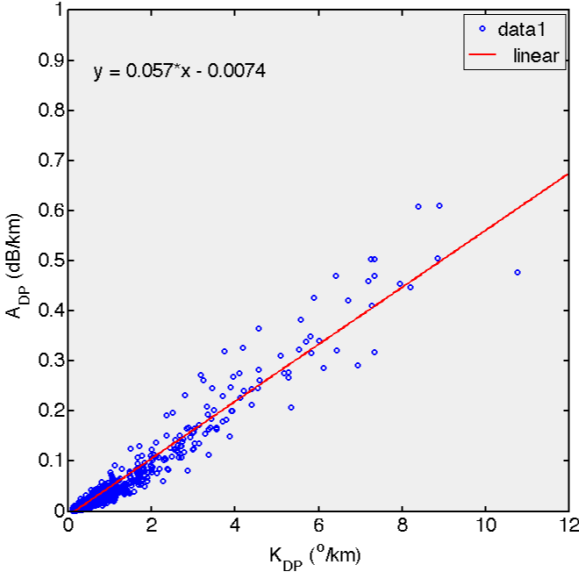
(c) Gan



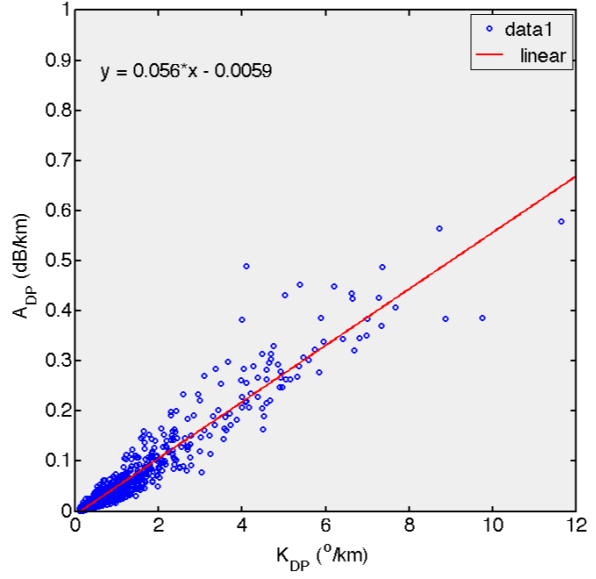
(d) MC3E

FIGURE 3.7. The $A_H - K_{DP}$ relations, derived from scattering simulations using one-minute DSDs from four 2DVDs located in different geographic locations. (a) Huntsville, AL (HSV), (b) Iowa (IFloodS), (c) Maldives (Gan), and (d) Oklahoma (MC3E).

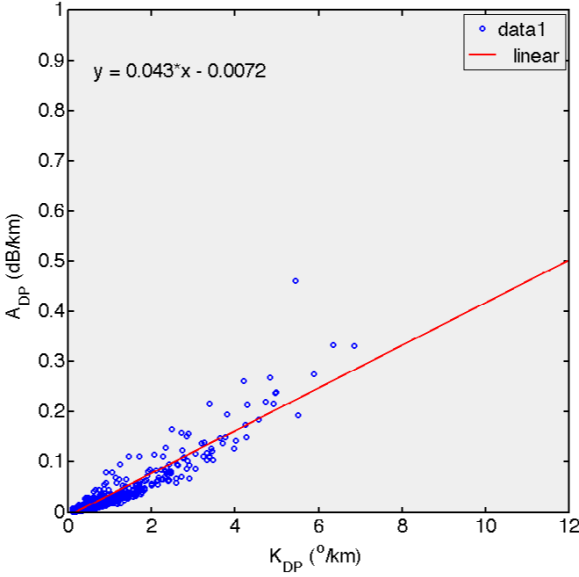
of the DSD, and R is also proportional to the 3.67^{th} moment of the DSD (i.e., Volume * Fall speed, of the drop), and as such, the other radar parameters are also related as moments of



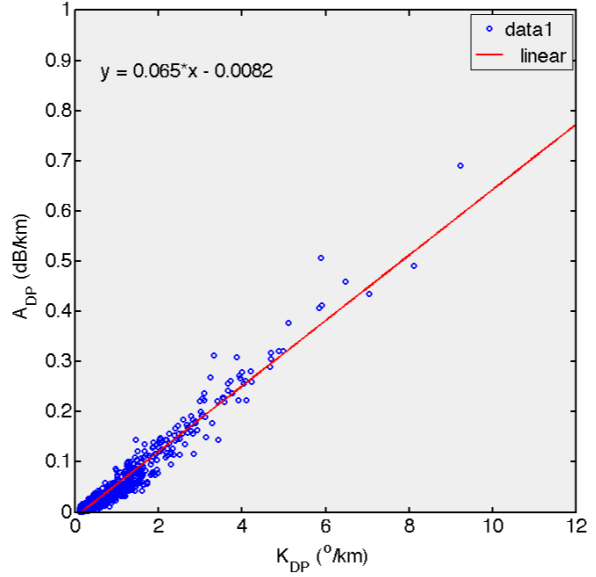
(a) HSV



(b) IFloodS



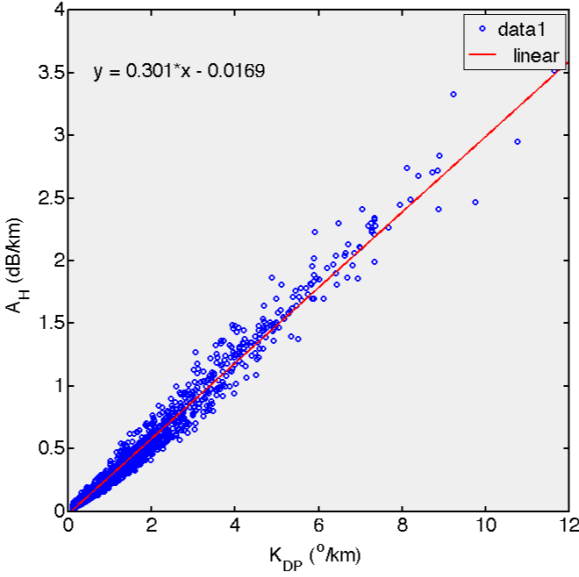
(c) Gan



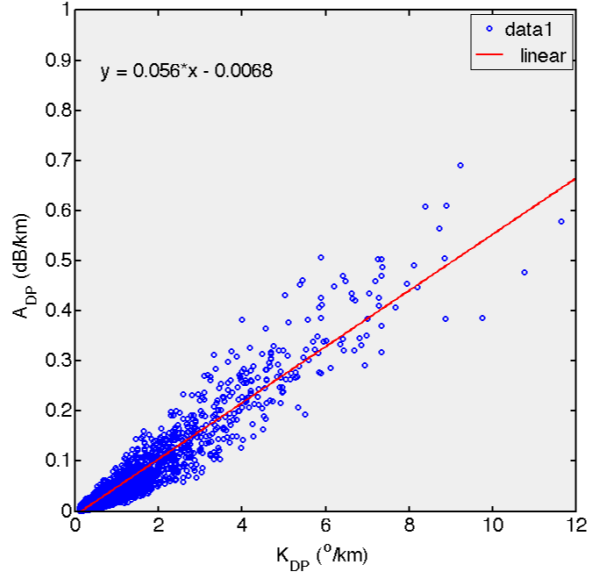
(d) MC3E

FIGURE 3.8. The $A_{DP} - K_{DP}$ relations, derived from scattering simulations using one-minute DSDs from four 2DVDs located in different geographic locations. (a) Huntsville, AL (HSV), (b) Iowa (IFloodS), (c) Maldives (Gan), and (d) Oklahoma (MC3E).

the drop size distribution. Scatter in the rain rate algorithms is primarily due to fluctuations in the DSDs and D_m 's at each point.



(a) Global $A_H - K_{DP}$ relation



(b) Global $A_{DP} - K_{DP}$ relation

FIGURE 3.9. 2DVD scattering simulations for the Global (a) $A_H - K_{DP}$ and (b) $A_{DP} - K_{DP}$ fits, derived from the combined (i.e., Global) DSDs from the four geographical locations.

TABLE 3.2. Scattering Simulation Relations between $A_H - K_{DP}$ & $A_{DP} - K_{DP}$. Linear fit slope and y-intercept are summarized for the various locations. We should note the y-intercept values for both fits are very small and thus we assume the relations only by the slope, i.e., coefficient.

2DVD Location	$A_H = \alpha K_{DP} + b$		$A_{DP} = \beta K_{DP} + c$	
	α	b	β	c
HSV	0.299	-0.015	0.057	-0.0074
IFloodS	0.295	-0.0152	0.056	-0.0059
MC3E	0.34	-0.028	0.065	-0.0086
Gan	0.27	-0.008	0.043	-0.0072
Global	0.301	-0.0169	0.056	-0.0068

In Figure 3.10, we see similarities from the four locations in the Z-R power law fit, $Z_{H-linear} = eR^f$, with the most scatter observed for moderate to high rain rates. The Z-R relation is the standard rain rate algorithm used for non-polarimetric radars (the global Z-R power law derived here is identical to the NEXRAD default power law $Z = 300R^{1.5}$. In the case of polarimetric-based rain rate estimators they often default to the climatological

Z-R relation at light rain rates with small drops, with low reflectivity values and near-zero K_{DP} . In Figure 3.11, the $R = cA_H^d$ estimator shows high scatter for low rain rates, but reduced variability at higher rain rates. The $R - A_H$ relations shown here are consistent with that presented by [19], where they propose this algorithm as a better radar-derived rain rate estimator, as it is less susceptible to the variability of drop size distributions in a wide range of rain intensities. In Figure 3.13, we see similar variability in $R = aK_{DP}$ over moderate to high rain rates, but when applied to the beam we expect some smoothing due to the nature of calculating the K_{DP} . In Figure 3.12, we immediately recognize the "tight" fit in the $R = gA_H^j Z_{DR-linear}^k$ algorithm, with minimal variability in rain rates from moderate to high rain intensities. However, in practice this algorithm is susceptible to Z_{DR} measurement and attenuation correction errors, which can lead to inflated rain rate estimates after these errors propagate through the rain rate estimator. In Figure 3.14 we compare the four rain rate algorithms, fit to the Global dataset, where again the $R(A_H, Z_{DR-linear})$ is shows the least amount of variability over all rain intensities, as compared to the other fits. Table 3.3, summarizes the coefficients and exponents of the various power law fits used to define the various Rain Rate algorithms. As noted earlier, the Global Z-R relation shows very good agreement with the NEXRAD $Z - R$ radar derived rain rate, i.e., $Z = 300R^{1.5}$. It is important to note that, for instance, in the $R - A_H$ estimator for Gan that has a higher rain rate for a given specific attenuation, as compared with the more convective events at MC3E. This is primarily due to more rain in Gan having a increased number of smaller drops resulting in the higher coefficient. The variability in coefficient and exponent values, although for a small subset of geographical locations, suggests that it is prudent to fine tune the rain rate algorithms to the local climatology and rain types present in the region.

We should note that all of these rain rate algorithms are based on "perfect" scattering simulations (i.e., theoretical best estimates under ideal conditions) and do not account for measurement errors, nor errors in the attenuation-corrected reflectivity and differential reflectivity which can amplify the rain rate estimate errors. There is no consensus in the literature as to the best rain rate algorithm for the different climatologies, so we use these simulation-based relations as guides only.

TABLE 3.3. Rain Rate algorithms from 2DVD scattering simulations, summarized for the various locations.

Location	$R = aK_{DP}^b$		$R = cA_H^d$		$Z_{H-lin} = eR^f$		$R = gA_H^j Z_{DR-lin}^k$		
	a	b	c	d	e	f	g	j	k
HSV	18.16	0.87	47.32	0.7876	262.93	1.49	156.01	1.004	-2.06
IFloodS	15.55	0.89	46.15	0.8748	351.08	1.56	153.25	1.005	-1.95
MC3E	13.45	0.85	32.60	0.7279	321.59	1.62	103.58	0.947	-1.86
Gan	25.10	0.91	70.5	0.7923	240.96	1.27	161.42	0.983	-2.01
Global	17.22	0.91	46.13	0.8181	299.98	1.50	176.89	1.032	-2.34

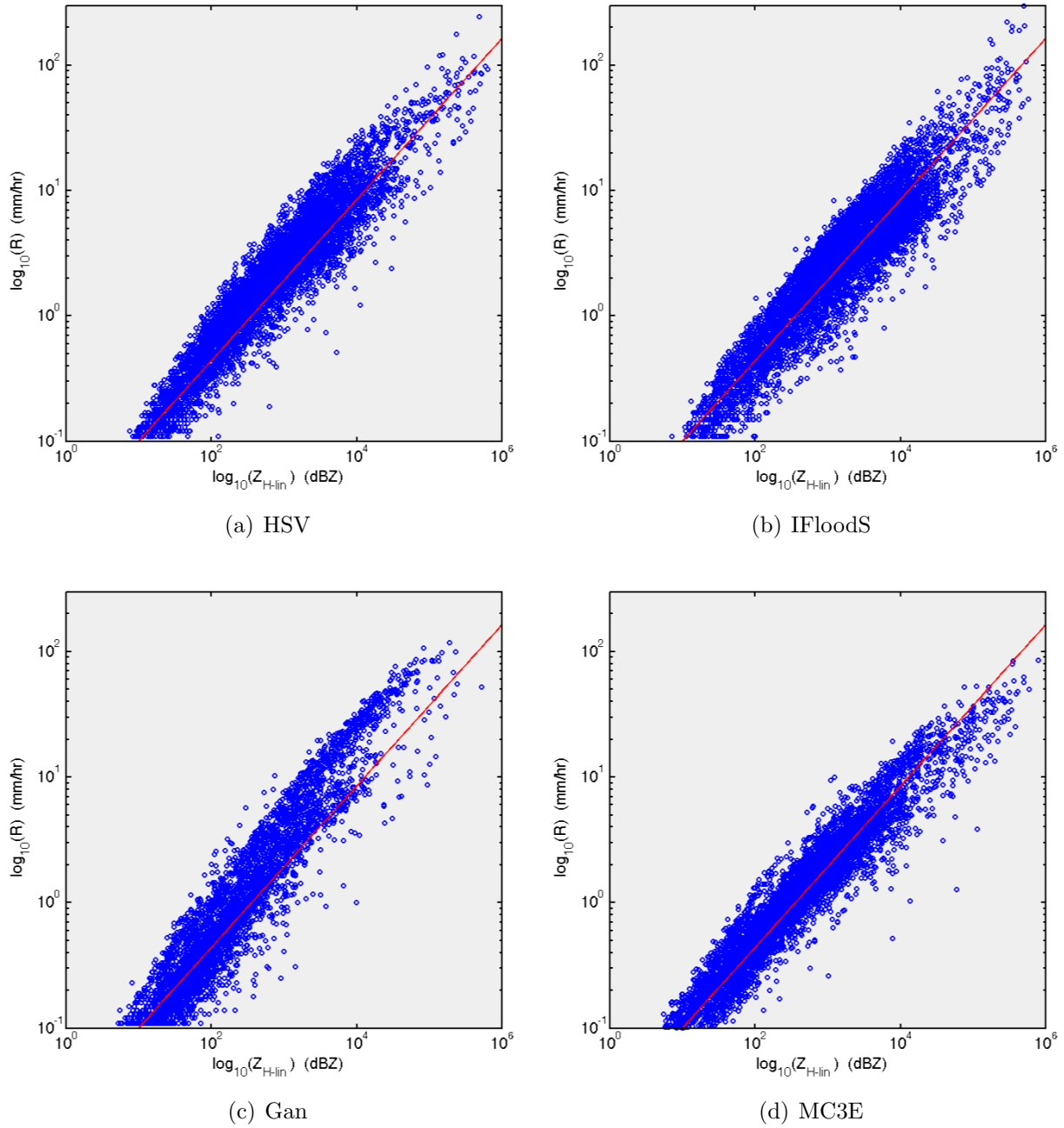
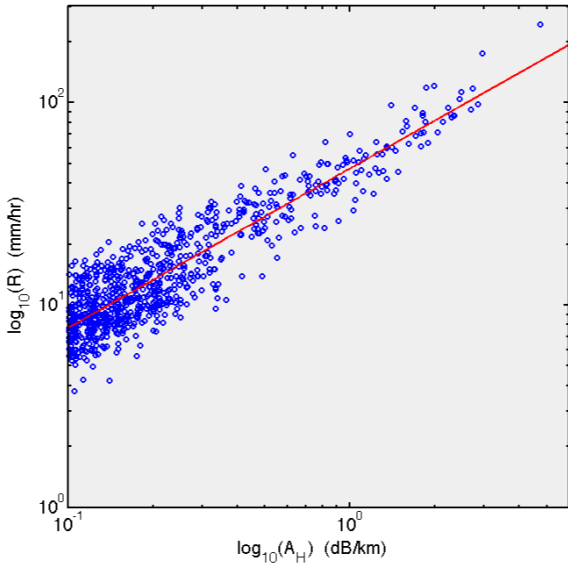
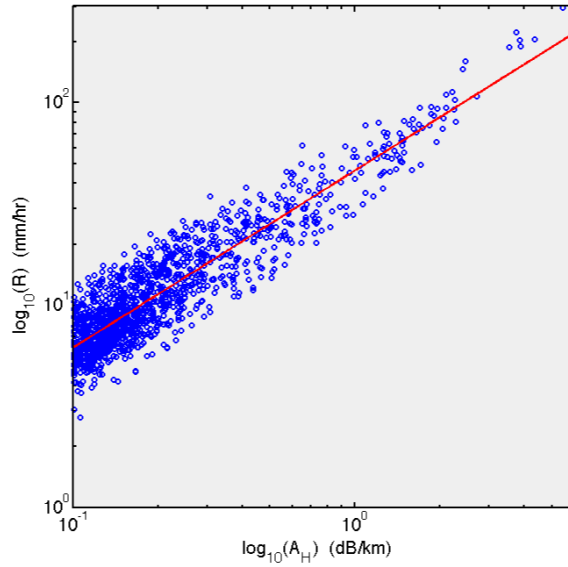


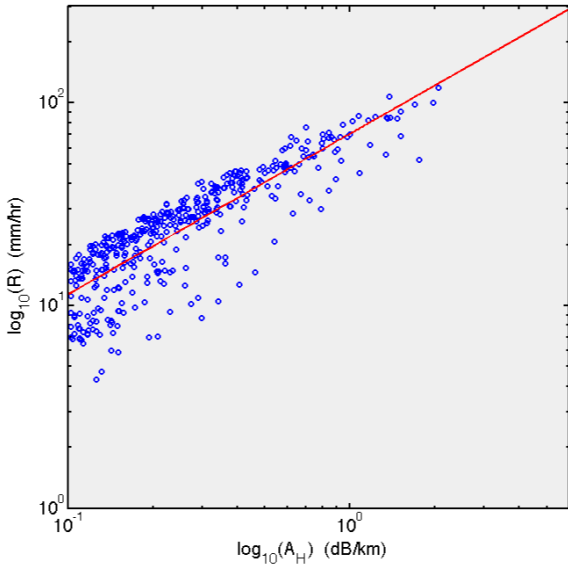
FIGURE 3.10. Rain Rate estimator using the $Z_{H-lin} - R$ fit to scattering simulations using one-minute DSDs from four 2DVDs located in different geographical locations. (a) Huntsville, AL (HSV), (b) Iowa (IFloodS), (c) Maldives (Gan), and (d) Oklahoma (MC3E).



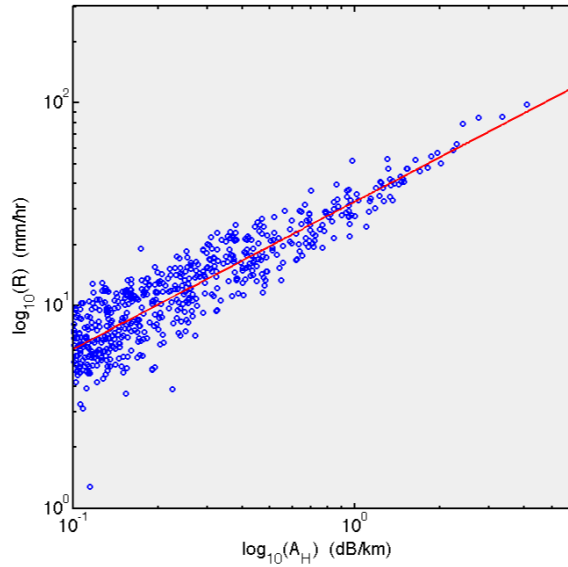
(a) HSV



(b) IFloodS

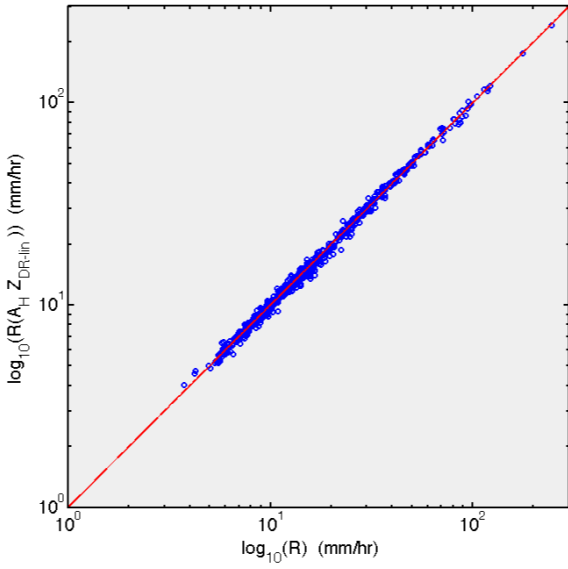


(c) Gan

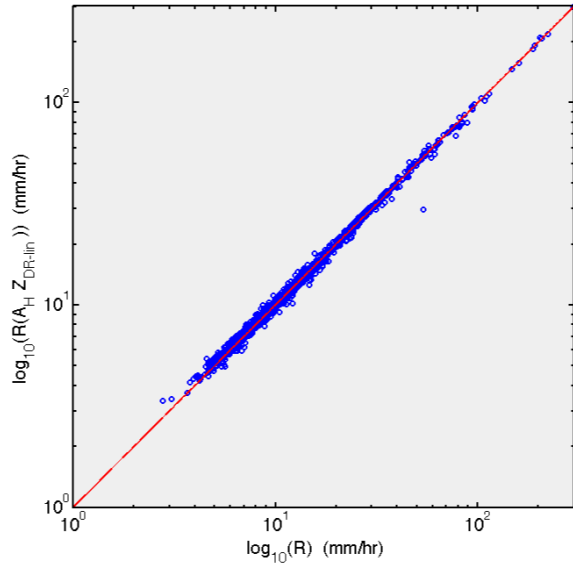


(d) MC3E

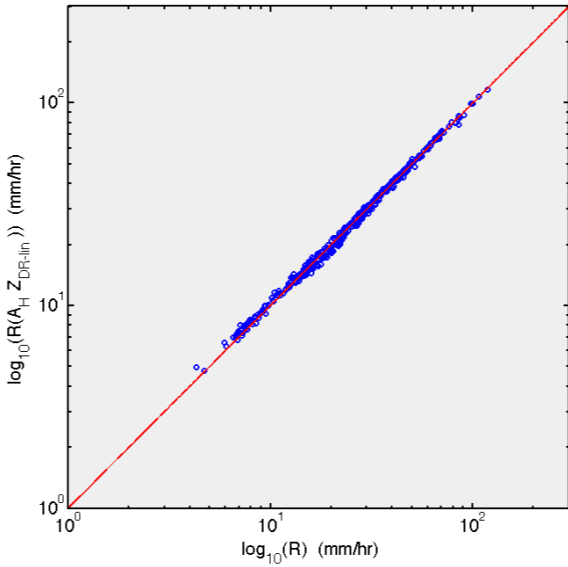
FIGURE 3.11. Rain Rate estimator $R(A_H)$ fit to scattering simulations using one-minute DSDs from four 2DVDs located in different geographical locations. (a) Huntsville, AL (HSV), (b) Iowa (IFloodS), (c) Maldives (Gan), and (d) Oklahoma (MC3E).



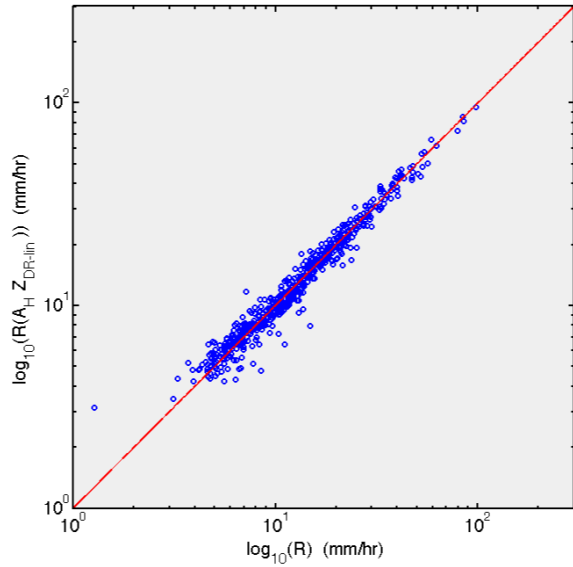
(a) HSV



(b) IFloodS



(c) Gan



(d) MC3E

FIGURE 3.12. Rain Rate estimator $R(A_H, Z_{dr-linear})$ fit to scattering simulations using one-minute DSDs from four 2DVDs located in different geographical locations. (a) Huntsville, AL (HSV), (b) Iowa (IFloodS), (c) Maldives (Gan), and (d) Oklahoma (MC3E).

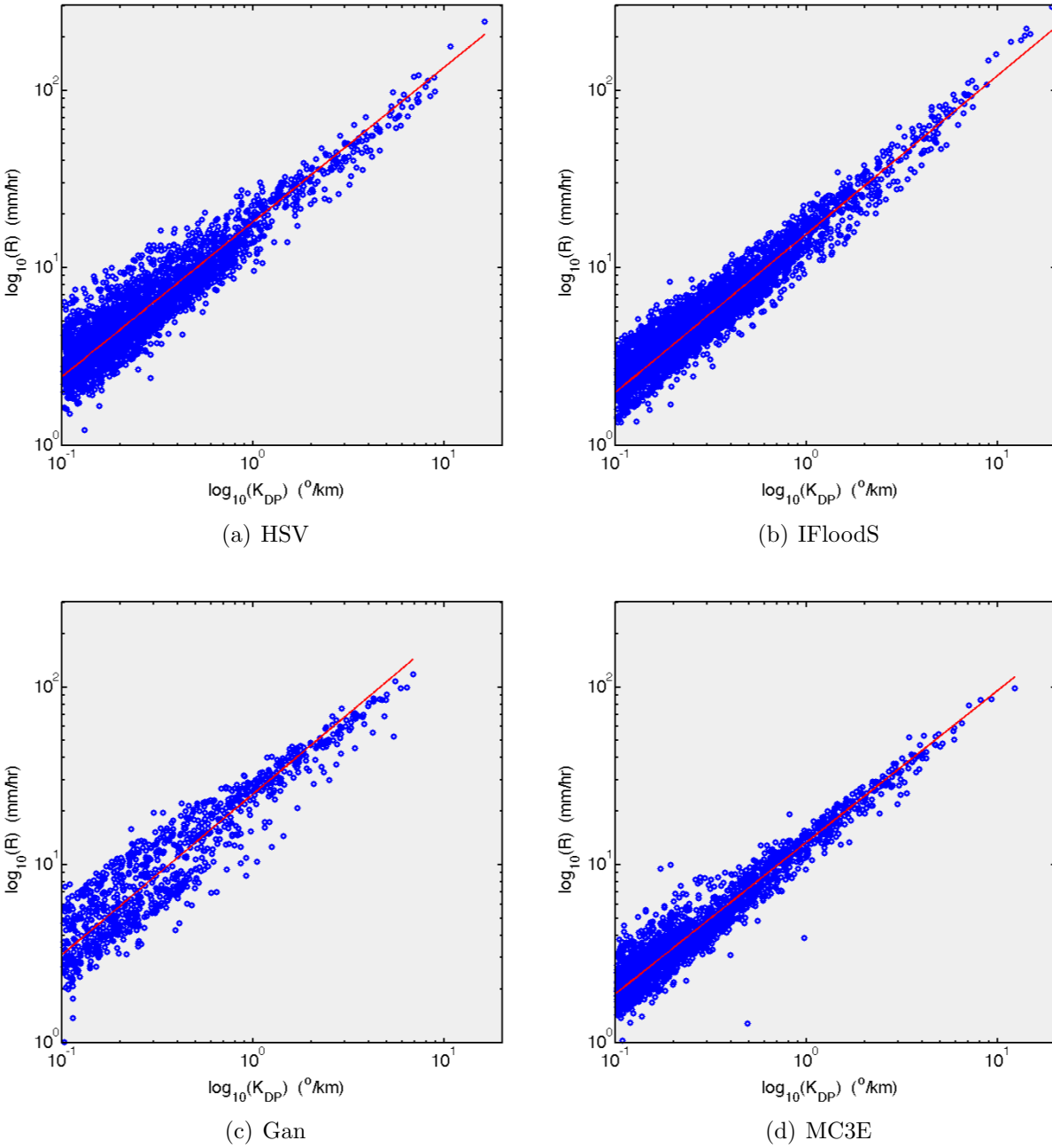
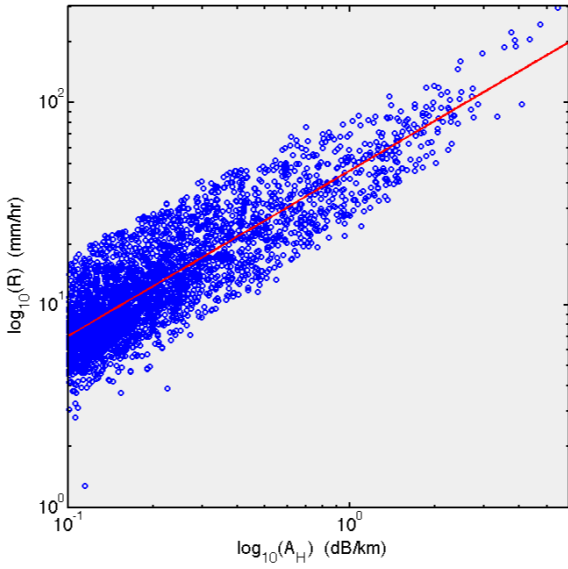
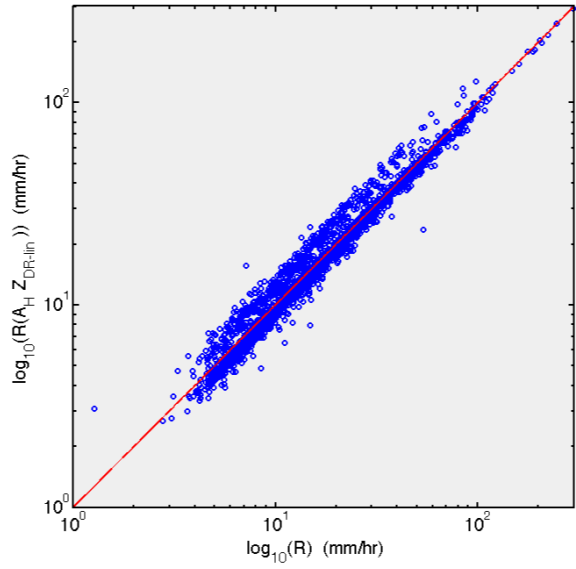


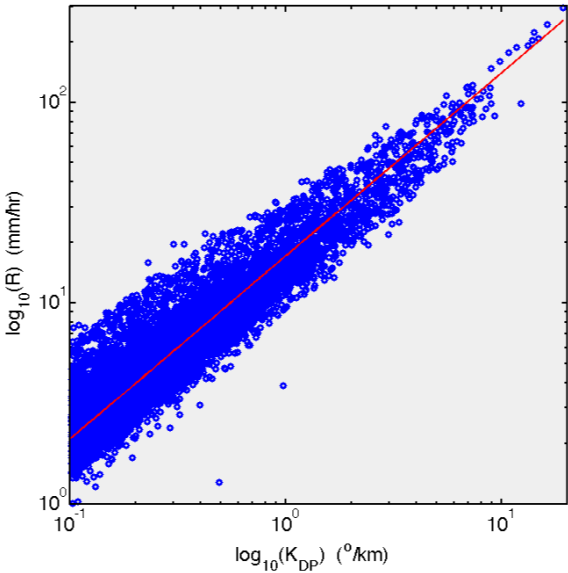
FIGURE 3.13. Rain Rate estimator $R(K_{DP})$ fit to scattering simulations using one-minute DSDs from four 2DVDs located in different geographical locations. (a) Huntsville, AL (HSV), (b) Iowa (IFloodS), (c) Maldives (Gan), and (d) Oklahoma (MC3E).



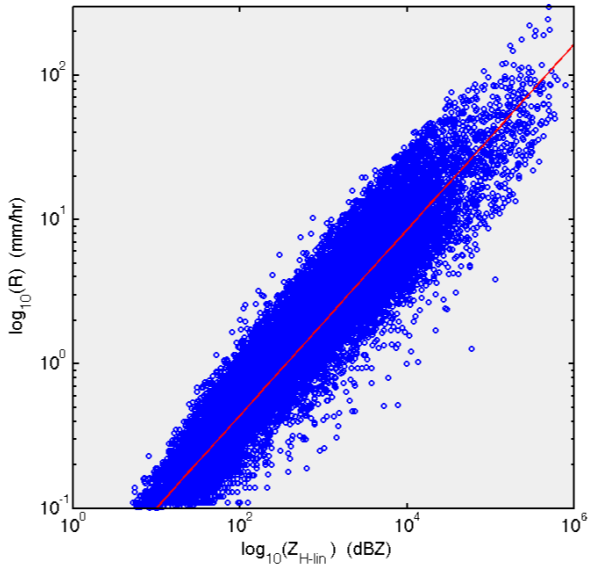
(a) $R(A_H)$



(b) $R(A_H, Z_{dr-linear})$



(c) $R(K_{DP})$



(d) $Z_{H-linear} - R$

FIGURE 3.14. Global Rain Rate estimator algorithms fit to scattering simulations using one-minute DSDs from four 2DVD locations: (a) $R(A_H)$, (b) $R(A_H, Z_{dr-linear})$, (c) $R(K_{DP})$, and (d) $Z_{H-linear} - R$.

CHAPTER 4

ATTENUATION CORRECTION USING THE ITERATIVE ZPHI METHOD AND AN IMPROVED DIFFERENTIAL BACKSCATTER PHASE ESTIMATOR

In this Chapter, we will introduce the attenuation-correction procedure applied to the Iowa XPOL radar data collected during the NASA GPM IFloodS field campaign. We share the summarized description of the ZPHI method, with Φ_{DP} constraint for attenuation correction at X-band, as presented in our article in the *Journal of Hydrometeorology* titled, "Deployment and Performance Analyses of High Resolution Iowa XPOL Radar System during the NASA IFloodS Campaign" [23]. In addition, we present an iterative FIR range filter designed for X-band radars with high range resolution ($\Delta r=30\text{m}$), based on a method proposed by Hubbert and Bringi (1995) for systems operating at $\Delta r=150\text{m}$, providing improved estimation of differential backscatter phase, δ , at these shorter range intervals. We introduce the attenuation correction procedures and filter design here, and in chapter 5 will present results from data observed during the IFloodS field campaign.

4.1. SUMMARY OF ATTENUATION CORRECTION PROCEDURE

At frequencies above S-band (10 cm), radar operating wavelengths decrease and correction of the measured reflectivity, Z_H , and differential reflectivity, Z_{DR} , due to rain attenuation along the propagation path becomes essential, particularly at X-band (3.2 cm) in convective storms. The method used herein for correcting the measured Z_H is an iterative version of the ZPHI method which uses a Φ_{DP} constraint [24, 25], initially developed at C-band then later extended to X-band by [26, 22]. In brief, the coefficient α is the linear relation between

specific attenuation at horizontal polarization (A_H) and specific differential phase (K_{DP}), approximately $A_H = \alpha K_{DP}$. This optimal coefficient is determined by minimizing a cost function (we refer to [2] for details), whereas the standard ZPHI method assumes an a priori fixed value for α [24]. In the modified ZPHI method, the optimal α obtained from this iterative process, overcomes its dependence on temperature and any potential deviations of the raindrop oblateness model from equilibrium theory [27]. There is additional compensation for drop size distributions, DSDs, with above average values of D_0 (median volume diameters > 2.5 mm or so). It is important to note that like all attenuation-correction algorithms based on Φ_{DP} , the correction is an approximation since the true DSD along the propagation path is not known. In essence, we obtain the optimal α and fix it for the entire beam, on a ray-by-ray basis, using the algorithm described in [22] with modifications for the higher range resolution ($\Delta r=30$ m) of the XPOL radar systems. Improvements in determining the optimal α are possible if the full beam is divided into smaller range intervals, then applying the estimation procedure to yield an optimal α coefficient for each sub-interval [21]. There are other alternatives of the attenuation-correction method at X-band, as elucidated, for example, by [28], [29], and [30].

The correction of the measured differential reflectivity, Z_{DR} , for specific differential attenuation (A_{DP}) is based on a method proposed by Smyth and Illingworth [31] for C-band, which is described in [2] as a "combined $\Phi_{DP} - Z_{DR}$ constraint." This method was later extended to X-band by Park et al. (2005 II) which is used herein with modifications tuned for the Iowa XPOL radars. In brief, the previously determined specific horizontal attenuation A_H using the Φ_{DP} constraint is scaled by a factor γ , and the measured Z_{DR} is corrected for the differential attenuation ($A_{DP} = \gamma A_H$), such that a desired value is reached at the end of the beam. The desired value is the intrinsic or 'true' Z_{DR} value at the end of the beam,

which is estimated from the corrected Z_H via a mean Z_H - Z_{DR} relation based on scattering simulations that use measured drop size distributions (DSDs) from several locations in eastern Iowa, representing a wide variety of rain types. This sets a constraint for Z_{DR} at the end of the beam (generally the $Z_{DR} \approx 0$ dB is due to light rain at the end of the beam or due to ice particles above the 0° C level). The end of the beam is defined as the last range gate where "meteo" echoes are detected. Like before, the differential attenuation-correction is approximate since the true DSD along the beam is unknown. Kim et al. (2010) proposed a method to correct for Z_{DR} by using the ZPHI method to independently estimate A_H and A_V (i.e., via the optimal coefficients α_H and α_V ; note that $A_{DP} = A_H - A_V$) without using an explicit Z_{DR} constraint at the end of the beam.

4.2. DATA PROCESSING STEPS FOR THE ATTENUATION-CORRECTION PROCEDURE

The processing steps used to correct the measured Z_H and Z_{DR} for XPOL data closely follow that proposed by [32, 33], and hence, we only summarize them here.

- I. On a ray-by-ray basis, we generate a data mask along each range profile to separate precipitation ('meteo'=1) from non-precipitation ('non-meteo'=0) echoes using the standard deviation of Φ_{DP} over a 10-gate moving window. The classification is based on using a threshold of 5° and an $SNR > 0$ dB, and may sometimes be referred to as the 'good data mask.'
- II. We correct the measured Z_H and Z_{DR} values for attenuation, as previously described.
- III. To derive the specific differential phase, K_{DP} , we first use the iterative range filter methodology applied to each range profile of Ψ_{DP} . The finite impulse response (FIR) range filter is, in essence, a weighted moving average filter where the weights are determined by the desired magnitude response of the filter transfer function (or spectrum).

Here, the FIR filter coefficients are based on a 75 m range gate spacing (an example of the filter transfer function for 150 m gate spacing can be found in [34]). It is important to note that for this study of the IFloodS data from XPOL-4, the range gate spacing was 30 m. The iterative nature of the algorithm described in Hubbert and Bringi (1995) is designed to remove local perturbations in the Ψ_{DP} data (e.g., due to backscatter differential phase) while still preserving the monotonic increase in propagation phase (Φ_{DP}) with range, along the beam. The copolar differential phase, Ψ_{DP} , consists of two phase components, that include the differential propagation phase, Φ_{DP} , and the differential backscatter phase, δ . We will consider the estimation of these perturbations later in this chapter. A "telescoping" method is used to compute the K_{DP} from the iteratively filtered Φ_{DP} profile, that is, a variable number of range gates is used, depending on the Z_H value, to determine the slope of a linear least squares fit. Selection of the telescoping gate number is as follows: 10 gates if $Z_H > 35$ dBZ; 20 gates if $25 < Z_H < 35$ dBZ; and 30 gates if $Z_H < 25$ dBZ. The telescoping method can be considered ad hoc, but has good agreement with the light (9 gates) and heavy (25 gates) filtering for computing K_{DP} discussed by [35].

Since the data processing progresses one beam (or range profile) at a time, we illustrate in Figure 4.1 range profiles of (a) the measured and attenuation-corrected Z_H , and the same for (b) Z_{DR} . The path integrated attenuation (PIA= corrected - measured, across the rain cell) from 0-20 km is around 14 dB, while the path integrated differential attenuation is around 2.7 dB. This sample beam is at an azimuth angle of 310° and elevation angle of 10.7° , as indicated by the dashed lines in Figure 5.4. Panel (c) shows the monotonically increasing Φ_{DP} with range, the overall difference across the rain cell is around $\Delta\Phi_{DP} = 40^\circ$. The filtered propagation phase, $\Phi_{DP-filt}$, is also shown from which K_{DP} is calculated. The

coefficient α , of the $A_H - K_{DP}$ relation, can be estimated as $\alpha \approx \text{PIA}/\Delta\Phi_{DP-filt}$ over the rain cell range interval. For this range profile $\alpha=14/40=0.35$ dB/deg, whereas the coefficient β (in $A_{DP} - K_{DP}$) is $2.7/40 = 0.067$ dB/deg. Panel (d) shows the K_{DP} profile seeing a peak of 5.6 °/km at a range of 12 km; the corresponding corrected Z_H and Z_{DR} are 52.8 dBZ and 2.2 dB, respectively. Also shown in this panel is the data mask indicating the occurrence of precipitation echoes (1 \equiv 'meteo', 0 \equiv 'non-meteo' echoes).

The rain rate from K_{DP} can be derived from $R = 14.2K_{DP}^{0.85}$, which gives 60 mm/hr whereas the $Z_H = 320R^{1.55}$, with $Z_H=52.8$ dBZ, also gives close to 60 mm/hr. The coefficients and exponents of the $R(K_{DP})$ and $R(Z_H)$ power laws are derived from 2D-video disdrometer measured DSDs from four days during IFloodS, and scattering simulations using the T-matrix method, assuming the 80 m fall bridge shapes from [36] and Gaussian distribution of canting angles with $[\mu = 0^\circ; \sigma = 7.5^\circ]$ from [37]. The agreement between the calculated rain rates, $R(K_{DP})$ and $R(Z_H)$, for the 12 km range gate is perhaps coincidental but it affirms that the Z_H attenuation-correction is reasonable (if the measured $Z_H = 42$ dBZ had been used, the corresponding R would have been severely underestimated at 12 mm/hr). This result attests to the established importance of attenuation correction at X-band particularly if Z-R relations are subsequently used to quantify rainfall amounts.

4.3. ITERATIVE FIR RANGE FILTER DESIGN FOR X-BAND RADARS OPERATING AT HIGH RANGE RESOLUTIONS OF $\Delta R=30\text{M}$

The copolar differential phase, Ψ_{DP} , measurement is of utmost importance and uniquely inherent to dual polarization radars. It has the advantage over reflectivity and differential reflectivity in that it is not adversely affected by attenuation along the propagation path

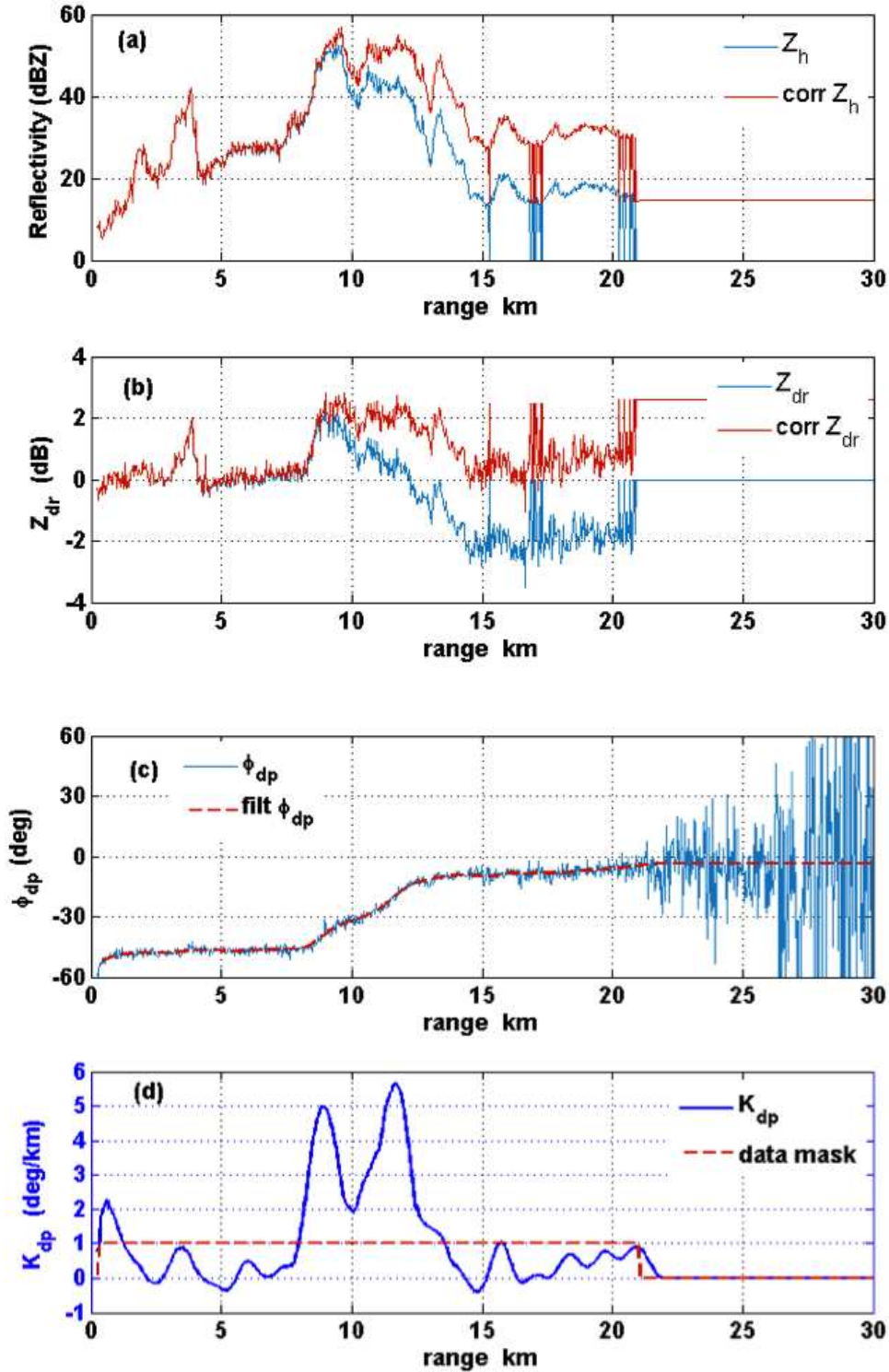


FIGURE 4.1. Example range profile from XPOL-4 radar during IFloodS on June 12, 2013 at 233230 UTC, AZ=310°, EL=10.7°. In panels (a) and (b) 'corr' stands for attenuation-corrected values. In (c) 'filt' stands for FIR range filtered Φ_{DP} . Data mask value of 1 \equiv 'meteo' echoes and 0 \equiv 'non-meteo' echoes (in this beam the latter is receiver noise).

through precipitation, nor to radar calibration issues. It is composed of two phase components, one being the range cumulative differential propagation phase, Φ_{DP} , and the other is due to scattering effects at each range resolution volume, known as differential backscatter phase, δ . In a purely rain event, Ψ_{DP} is dominated by Φ_{DP} , and we can easily rely on the computed slope of the copolar differential phase, i.e., specific differential phase K_{DP} , to estimate the rain rate and rainwater content. On the contrary, in the presence of melting hail or Mie scattering effects, δ becomes increasingly more significant in the copolar differential phase ($\Psi_{DP} = \Phi_{DP} + \delta$) which leads to local perturbations or "bumps" in the normally monotonic increasing Ψ_{DP} along the range. These δ bumps bias the estimated K_{DP} and lead to subsequent errors in estimations of rain rate and rainwater content. Unlike radars operating at S-band (10 cm), the effects due to Mie scattering are very relevant to hydrology studies using dual polarization Doppler weather radars operating at shorter wavelengths, like those at X-band (3.2 cm) and C-band (5 cm), for instance. In order to ensure accurate rain rate estimates based on K_{DP} at X-band, it is imperative that the δ is properly separated from the copolar differential phase measurement before computing specific differential phase.

For our filter design, we refer to the iterative range filtering technique developed by [34] (henceforth, H&B-95) for the analysis of Ψ_{DP} and dual-wavelength radar measurements, which has successfully proven to mitigate the local perturbations due to differential backscatter phase, in the monotonically increasing differential phase of radars operating with range resolutions of $\Delta r = 75 - 150$ m. Most polarimetric weather radars operating in the 5 cm to 10 cm wavelength regime (C-band & S-band), typically use these coarse range resolution intervals as a trade-off to increase the maximum achievable unambiguous scanning range, as limited by the radar PRF and the sampling frequency of the digital signal processor. Over the past decade, the use of X-band dual polarization radars has gained acceptance as a

complementary technology to the legacy S- & C-band radars used by the meteorological and hydrology communities. For instance, X-band polarimetric radars have been used in high spatio-temporal hydrology studies [23], warning systems for flooding and shallow landslide forecasting in urban areas [38], and configured in cooperative networks for urban and rural settings [39, 40], to combat the effects of signal extinction experienced by individual radars, at shorter wavelengths. These X-band radars are being operated with much higher range resolutions, for instance at a $\Delta r = 30\text{m}$ or less, like the University of Iowa XPOL radars.

We begin by evaluating the effectiveness of applying various iterative FIR range filters to a raw Ψ_{DP} range profile as observed by the XPOL-4 radar system during the IFloodS field campaign. Figure 4.2 compares the filtering performance of three iterated lowpass FIR range filters used to suppress the δ , all being lowpass FIR filters: (magenta) 40th order 75 m Butterworth of H&B-95, (black) 40th order 30 m Kaiser, and (green) 100th order 30 m Kaiser filters. We can clearly see similarities in δ -suppression between the 40th order FIR range filters (75 m & 30 m), although each was designed for a different spatial sampling period, the number of coefficients are the same. The coefficients of the H&B-95 FIR Butterworth filter were optimized for Δr of 75 to 150 meter intervals, which when applied to the much higher range resolution XPOL radar data, cannot effectively suppress the "bumps" in the monotonically increasing Ψ_{DP} , due to melting hail or Mie scattering effects. The superior δ -suppression rendered by the 100th order 30 m Kaiser lowpass FIR range filter is obvious in this range profile segment, and we will further discuss its design and a two-stage filtering process to further optimize it over the entire beam.

The Kaiser (or Kaiser-Bessel) finite impulse response (FIR) filter was selected from among several window functions that minimize the passband ripple by decreasing the sidelobes of the window transfer function. It is well known in the literature that a rectangular window

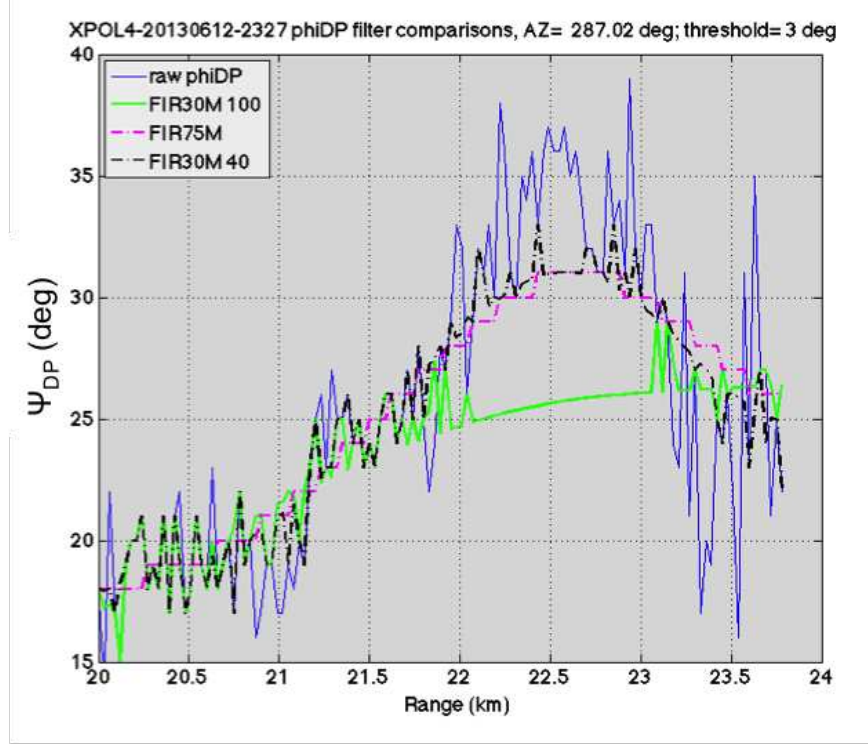


FIGURE 4.2. FIR30m-100 filter shows improvement in the ability to mitigate Mie backscattering between 20-24 km from the Φ_{DP} range profile through a convective storm. Radar data from a low elevation ($EL = 3^\circ$) XPOL-4 PPI scan, at $AZ = 287^\circ$, during IFloodS on 20130612-2327 UTC.

transfer function has very large sidelobes, at about -13 dB down from the main lobe, but on the contrary the Kaiser family of windows are optimized such that most of the energy is in its main lobe for a given side-lobe amplitude. The Kaiser window can be defined by (see [41, 42] for details),

$$(4.1) \quad w(n) = \frac{I_0 \left[\beta_K \sqrt{1 - \left(\frac{n-p}{p} \right)^2} \right]}{I_0(\beta_K)}, 0 \leq n \leq N$$

where $p=(N-1)/2$, and $I_0(*)$ is a zeroth-order modified Bessel function of the first kind, which can be generated using the power series expansion,

$$(4.2) \quad I_0(x) = 1 + \sum_{k=1}^{\infty} \frac{(x/2)^k}{k!}$$

The β_K parameter determines the shape of the window and controls the main lobe width and side-lobe amplitude δ_s . The relationship between the β_K parameter and stopband ripple of a lowpass filter, $\alpha_s = -20\log(\delta_{s-linear})$ can be determined as,

$$(4.3) \quad \beta_K = \begin{cases} 0.1102(\alpha_s - 8.7) & \alpha_s > 50 \\ 0.5842(\alpha_s - 21)^{0.4} + 0.07886(\alpha_s - 21) & 21 \leq \alpha_s \leq 50 \\ 0.0 & \alpha_s < 21 \end{cases}$$

and to meet our design criteria, we used a $\beta_K = 3.2$, which yielded a minimum sidelobe attenuation of $\delta_s = 25$ dB, and a stopband ripple $\alpha_s = 52$ dB. In order to "fine-tune" the filter, we used Matlab's Filter Design & Analysis Tool (FDATool), of the Signal Processing Toolbox, which saved time and made it simple to evaluate various other windows. We use this criteria for the design of both the 100th and 40th order FIR filters for the high spatial sampling of the XPOL radars (i.e., $\Delta r = 0.030$ km).

For the original attenuation-correction procedure, we applied the available 40th order "FIR75M" filter to the XPOL-4 data with $\Delta r = 0.030$ km, as mentioned in a previous section, where essentially we are applying a weighted moving average about each range sample, over a ± 600 meter window. Because we wanted better differential backscatter phase, δ , estimation we began to investigate the response of an equivalent Kaiser FIR filter. In Figure 4.3 we illustrate the magnitude response of the 40th order 30 m Kaiser lowpass FIR range filter, initially designed as the replacement for the Butterworth filter of H&B-95 (see [34], for an example 20th order filter, based on a 150 m spatial sampling period). The Kaiser FIR filter maintains the sharp attenuation (minimum of 25 dB) of spatial variations in the stopband, in this case over an interval of 0.4215 km or less based on the 0.030 km spatial sample period. Referring again to Figure 4.2, we see that 40 coefficients provide insufficient mitigation of the

spatial variation due to δ , which can potentially extend several kilometers, over the length of a strong convective core. The FIR30M-40 Kaiser filter appears to merely smooth along the average contour of the Ψ_{DP} , but also lightly filters the δ bumps. We will later capitalize on this apparent deficiency for the optimization of the two-stage FIR filtering process.

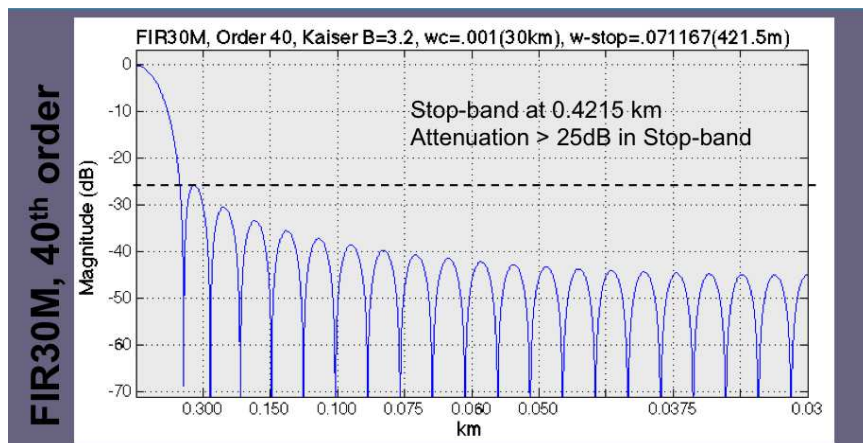


FIGURE 4.3. Magnitude response of the 40th order 30 meter lowpass FIR Kaiser range filter, "FIR30M-40". The design criteria included a minimum attenuation of 25 dB at the stop-band, in this case at 421.5 m (or 0.071167 km^{-1}).

If we now focus our attention on the frequency response of the 100th order Kaiser lowpass FIR filter (FIR30M-100) in Figure 4.4, we immediately see improvements in the stopband attenuation (near 52 dB), a narrower transition width from passband to stopband, and more importantly a further reaching stopband interval of 1.050 kilometers. The FIR30M-100 filter will sharply attenuate any statistical variations, as well as perturbations caused by δ , but will preserve the monotonically increasing differential phase due to propagation through rain. This is readily apparent in the comparison of δ mitigation capabilities of the 100th and 40th order Kaiser FIR filters, illustrated in Figure 4.5. We see that besides improved mitigation, the FIR30M-100 iterated filter reaches convergence within 4-5 iterations (9 iterations are shown), where even after 7 iterations of the FIR30M-40 filter, δ suppression is meager. The

convergence of the iterated 100^{th} order FIR filter is reached much faster than the 10 iterations achieved by the Hubbert & Bringi (1995) FIR filter.

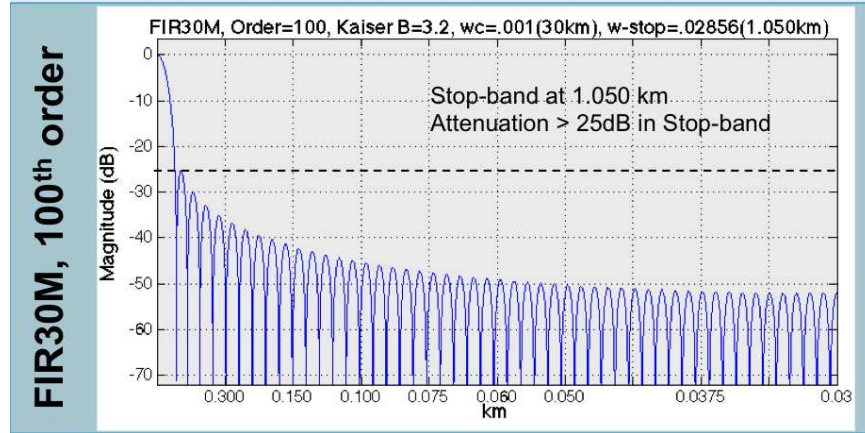


FIGURE 4.4. Magnitude response of the 100^{th} order 30 meter lowpass FIR Kaiser range filter, "FIR30M-100". The design criteria included a minimum attenuation of 25 dB at the stop-band, in this case at 1.050 km (or 0.02856 km^{-1}).

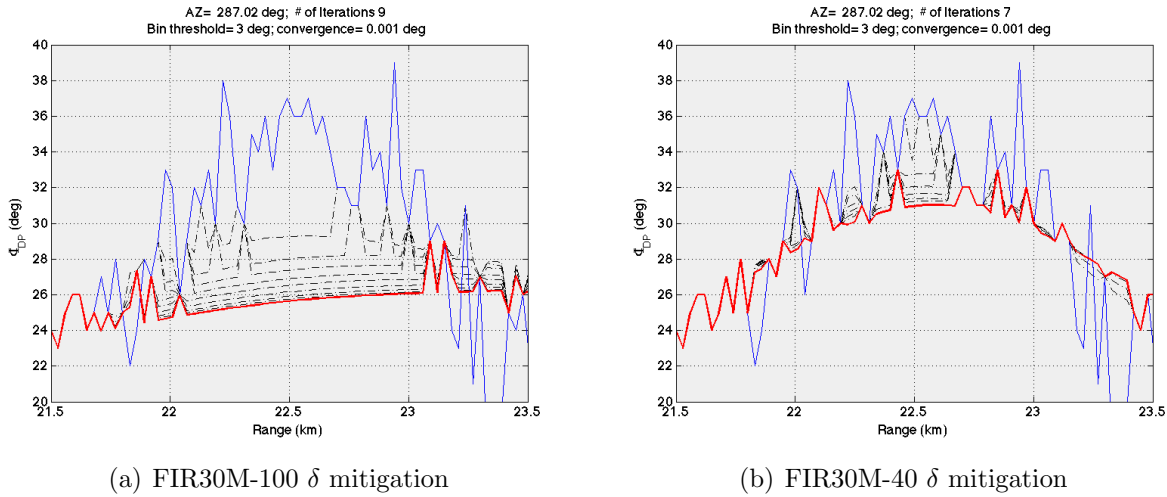


FIGURE 4.5. Comparison of δ suppression by the iterated filters using (a) 100^{th} order and (b) 40^{th} order Kaiser lowpass FIR filters. Note: (blue) raw Ψ_{DP} , (dashed) n^{th} iteration, (red) final iteration. A threshold of 3° is assessed at each range bin, while a convergence factor of 0.001° is used to stop the iteration process. The data is from the University of Iowa XPOL-4 radar ($\Delta r=30\text{m}$), collected during the IFloodS field experiment in the summer of 2013.

4.4. SIGNAL PROCESSING STEPS OF THE TWO-STAGE FIR RANGE FILTER FOR IMPROVED δ ESTIMATION AT X-BAND

The data signal processing steps taken to ensure the iterative filtering is possible on each range profile are now summarized, following the procedure described by [34]. In this technique, an iterative range profile, $\tilde{\Psi}_{DP}$, is constructed from either raw data or its filtered version as determined by a threshold. For our purpose, we found that a threshold of 3° yielded good results. The newly filtered range profile and the raw Ψ_{DP} are differenced at each range bin, and if its absolute value is greater than the threshold, the filtered range profile bin is selected, $\Phi_{DP-FIR}(r_n)$, otherwise the raw $\Psi_{DP}(r_n)$ value is kept to form the iterated $\tilde{\Psi}_{DP}$ range profile. Next, repeat the process by filtering $\tilde{\Psi}_{DP}$, and again take the difference with the original raw Ψ_{DP} range profile. This process continues until a convergence is reached, where the absolute value of the difference between $\tilde{\Psi}_{DP}$ -iterations is within a predefined tolerance. As previously mentioned about the FIR30M-100 filter, depending on the degree of δ bump suppression desired, convergence can be easily reached within 4-5 iterations.

Another important detail regarding the signal processing is how we manage bad data "gaps" in any particular range profile. These gaps of missing raw Ψ_{DP} data may be due to a low signal-to-noise ratio (SNR) in the absence of precipitation resulting in poorly estimated phase, or in the case of shorter wavelength radars (e.g. X-band with $\lambda = 3.2cm$), deep signal attenuation due to convective storm complexes, now below the SNR threshold. In these cases, interpolation is used to fill between the points at the edges of these gaps, or if at the beginning (end) of the rain cell we interpolate (extrapolate) to (from) the first (last) good range bin. Figure 4.6 illustrates how the filtered Φ_{DP} bridges the gap through the interpolated values, while still maintaining the general contour of the raw Ψ_{DP} .

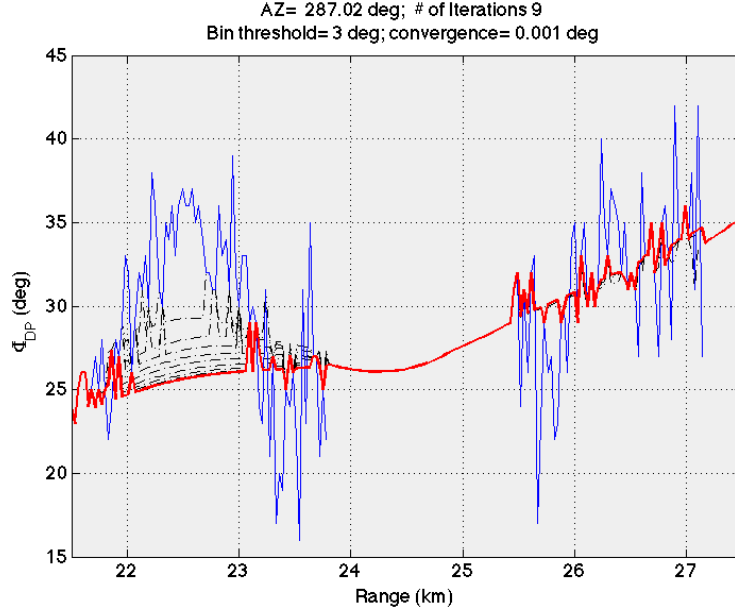


FIGURE 4.6. Interpolating over the non-meteo "gaps" in range profile segments. We interpolate over these regions prior to beginning the iterative filtering procedure in the two-stage FIR process. Shown are (blue) raw Ψ_{DP} , smooth filtered Φ_{DP} using the (magenta) FIR30M-100 Kaiser filter, and (dashed) iterations.

Satisfied with the improved performance of the 100th order Kaiser lowpass FIR filter (FIR30M-100) to mitigate the local perturbations due to differential backscatter phase, δ , we began to notice the filtered differential phase, $\Phi_{DP-filt}$, was over-smoothed in areas of transition (like at 10 and 15 km in Figure 4.7(a)). This could introduce bias in the specific differential phase, K_{DP} , and equally any rain rate estimate derived from it. After several unsuccessful attempts to reduce this premature smoothing, by varying the threshold and convergence tolerance in the iterative filtering technique, the "deficiency" of the FIR30M-40 Kaiser filter was revisited as a potential solution. Previously, the 40th order 30 m Kaiser FIR filter tended to follow the average contour of the raw Ψ_{DP} , while providing minimal δ suppression. These previously undesirable filter qualities could be applied to the final iteration of the filtered differential phase, $\Phi_{DP-filt}$, from the 100th order 30 m Kaiser FIR filter, to help reduce the over-smoothed regions. Figure 4.7(b), illustrates the better fitting results

by implementing this two-stage FIR range filtering technique which ultimately enhances differential backscatter phase estimation, where $\delta = \text{raw } \Psi_{DP} - \Phi_{DP-filt}$. Better estimates of differential backscatter phase at X-band can lead to improvements in estimating the K_{DP} , and in determining rain rates and rainwater content when using K_{DP} -based algorithms. In Chapter 5, further exploration is conducted into the effects of applying the two-stage FIR filtering technique to better estimate the δ signal.

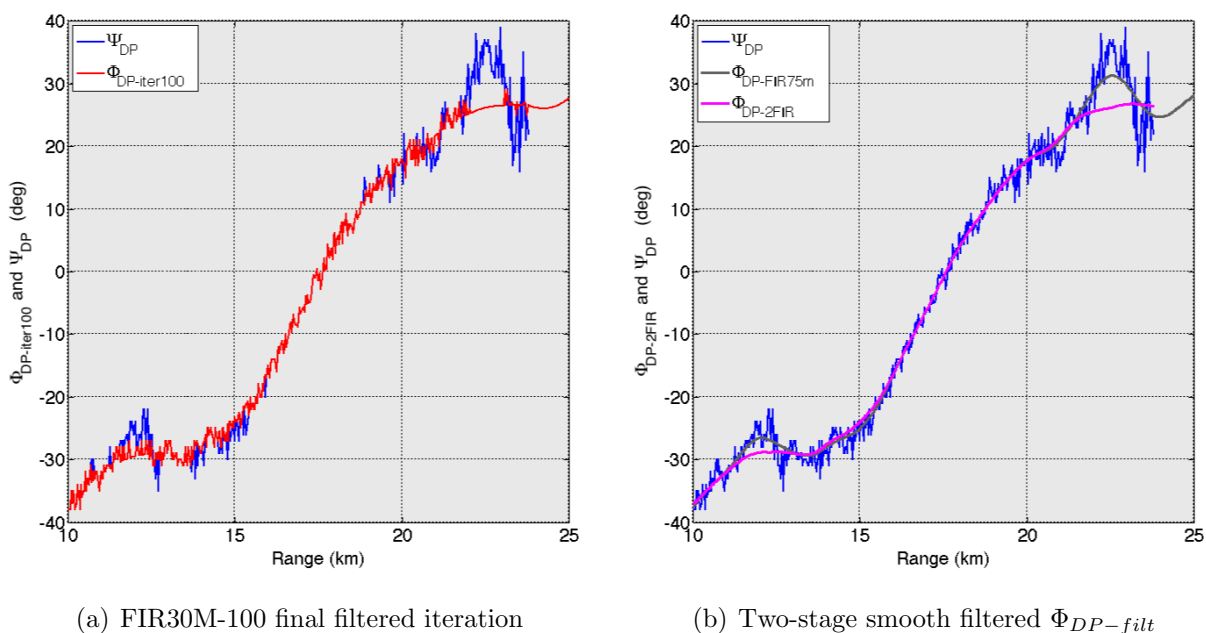
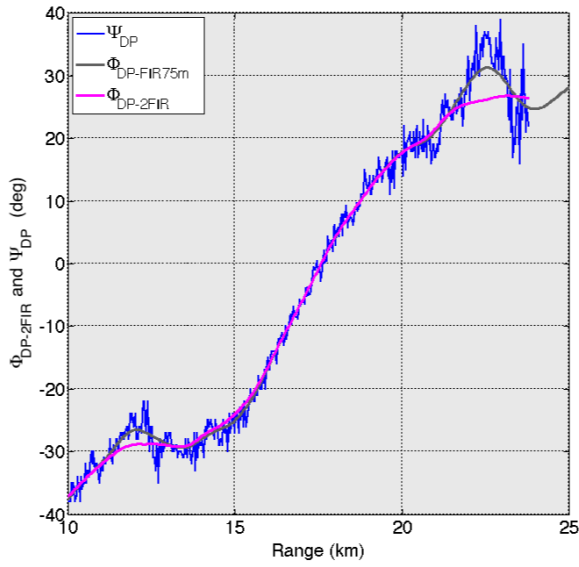


FIGURE 4.7. Range profile through a convective storm complex. In both, raw Ψ_{DP} is (blue); (a) is the Final iteratively filtered $\Phi_{DP-iter100}$ using the FIR30M-100 Kaiser filter (red), and in (b) the resulting two-stage smooth filtered $\Phi_{DP-2FIR}$ (magenta) after a single application of the FIR30M-40 Kaiser FIR to the Final iteratively filtered $\Phi_{DP-iter100}$ of (a). Radar data from Iowa XPOL-4 PPI at AZ=287 & EL=3, observed during IFloodS field campaign on 12 June 2013 at 23:27 UTC.

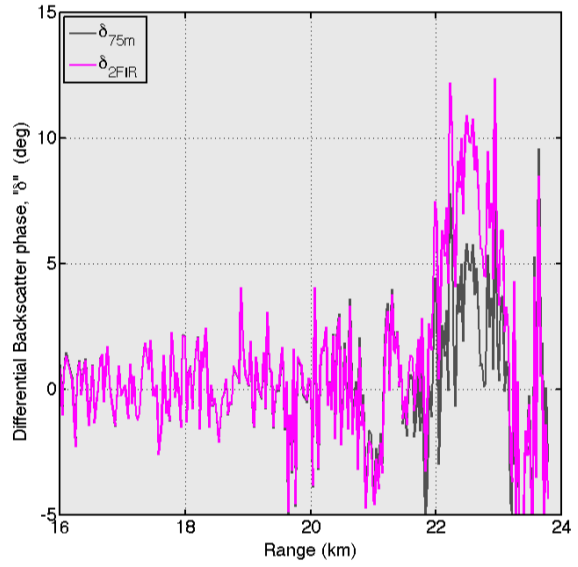
Now, considering the estimated differential backscatter phase "δ" obtained by applying the two-stage 100th order 30 m FIR lowpass range filter, improved detection of the local perturbation due to Mie scattering can clearly be seen. In Figure 4.8(b), the detection of backscatter phase is visible between 22-24 km down range from the radar, and also a small δ

around 11-13 km. Comparing it to the 40th order 75 m FIR lowpass range filter of Hubbert & Bringi (1995), the "δ" estimator using the new 2-stage FIR filtering of the Ψ_{DP} shows an appreciable improvement. This is due to the enhanced "δ" mitigation in the filtering of the raw copolar differential phase, evident in the comparison of the range profiles in Figure 4.8(a). Illustrated in panel (c) are overlaid scatter plots showing the relation between δ and Z_{DR-cor} for the two filtering methods. Again, the improved estimation of the 2-stage FIR filtering is evident by the higher concentration of δ 's values greater than 4° , indicating better detection of Mie scattering. The histograms of panel (d) confirm the better detection by the higher number of occurrences for the proposed filter. The $\delta - Z_{DR-cor}$ relation of the 2-stage FIR filter shows good agreement with the results obtained by [43], which are similar to the theoretical relationships for rain.

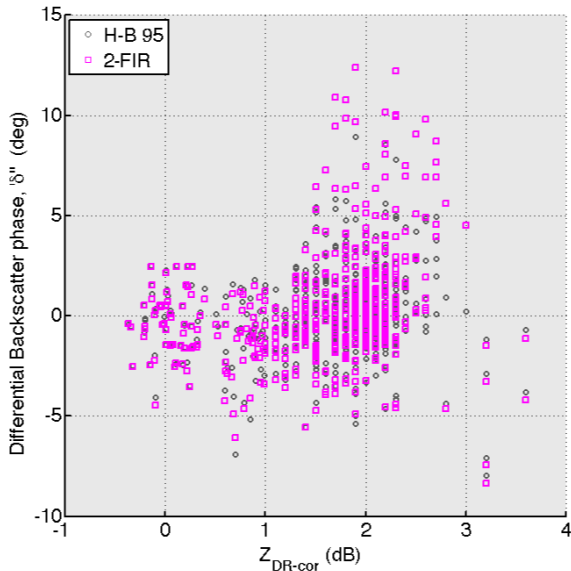
The enhanced differential backscatter phase estimation, using the proposed two-stage FIR lowpass filtering technique, has implications at X-band where Mie scattering can be experienced in moderate to severe rain. Estimation and detection of the backscatter phase can be used to improve specific differential phase, K_{DP} , and rain rate estimation, as well as aid in microphysical retrievals, as suggested for low elevation scans by [43].



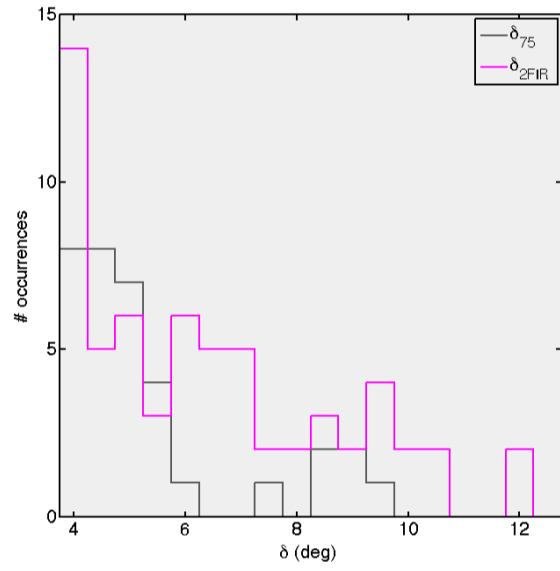
(a)



(b)



(c)



(d)

FIGURE 4.8. Estimated differential backscatter phase " δ " comparison between the proposed 2-stage FIR lowpass filter and the 75m FIR lowpass filter of Hubbert & Bringi (1995), H-B 95, when applied to the higher 30 m range resolution data of the XPOL-4. (a) Raw and filtered Φ_{DP} using both 2-stage FIR & FIR75m filters; (b) δ estimation, $r=16-24$ km; (c) δ vs. Z_{DR-cor} scatter plot for the $AZ = 287^\circ$ ray profile; (d) Histogram of $\delta > 4^\circ$ & $Z_{DR-cor} > 1$ dB for the ray profile. Radar data from Iowa XPOL-4 PPI at $AZ=287$ & $EL=3$, observed on 20130612-2327 UTC during the IFloodS field campaign.

RESULTS AND COMPARATIVE ANALYSES OF
ATTENUATION-CORRECTED XPOL RADAR DATA COLLECTED
DURING THE NASA GPM IFLOODS FIELD CAMPAIGN

During the spring of 2013, the Iowa Flood Studies (IFloodS) field campaign was conducted in central and northeastern Iowa as an integral component of the Ground Validation (GV) program of the NASA Global Precipitation Measurement (GPM) satellite mission. This experiment was collaboratively organized by NASA and the Iowa Flood Center [44] as the first NASA GPM-GV field campaign dedicated to hydrological studies. IFloodS was also the maiden field campaign for the four Iowa XPOL radar systems, and as such, gave us the opportunity to investigate their preferable high spatio-temporal resolution and also their ability to mitigate attenuation using common observations over watersheds from multiple radars. The mission of the Iowa XPOL radars is rain rate estimation over particular watersheds of interest, complemented by various ground-based instrumentation like rain gauges and two dimensional video disdrometers (2DVDs). During IFloodS the Turkey River Basin, in northeastern Iowa, was heavily instrumented with NASA dual tipping bucket rain gauges, while six 2DVDs were deployed further south. The careful layout of the experiment (see Figure 3.2) presented us with an opportunity to validate the XPOL radar data moments, as well as compare their radar-derived rain rate algorithms to that measured by the well-known ground-based instrumentation.

One advantageous application of X-band radar-derived rain rate estimates is to complement the ground-based "point" measurements by scanning over larger areas at pre-programmed intervals, thereby increasing the spatial and temporal resolutions of any hydrological experiment. As previously mentioned in Chapter 4, radars operating in the X-band frequency range will experience mild to severe attenuation as the radar pulse propagates through various rain types and intensities (e.g., from stratiform to convective storms). After careful correction for the precipitation-induced attenuation in reflectivity (A_H) and differential reflectivity (A_{DP}), we can expect improved radar-derived rain rate estimates that show good agreement with those from the gauges and 2DVDs.

In this Chapter, we will present the results and comparative analyses related to the attenuation-correction procedure applied to the Iowa XPOL radar data. To ensure data quality from the XPOL radars, a comparative analysis was conducted between scattering simulations from drop spectra collected by the 2DVDs, and the measured and corrected XPOL-4 radar relations for: $A_H - K_{DP}$, $A_H - A_{DP}$, $A_H - Z_H$, $Z_{DR} - Z_H$, and $Z_H - K_{DP}$. Upon demonstrating good agreement between the radar variables and scattering simulations, attenuation-corrected and inter-XPOL comparison results as presented in our journal article in the *Journal of Hydrometeorology* titled, "Deployment and Performance Analyses of High Resolution Iowa XPOL Radar System during the NASA IFloodS Campaign" [23]. Also presented are comparisons between rain rate time series from the XPOL-4 radar using various algorithms, to those measured by select NASA dual tipping bucket rain gauges located within the radar's scan area. For this analysis, we propose using a "nearest neighbor" selection criteria for choosing the radar pixels (at 30 m spacing), within a radius of influence around the rain gauge, for comparison to the point measurements. Lastly, we demonstrate the improvement in estimation of differential backscatter phase " δ ," using the iterative filtering

technique proposed by Hubbert and Bringi (1995), but applying a new two-stage FIR range filter on the raw, or measured copolar differential phase, Ψ_{DP} . The two-stage FIR range filter was specifically designed for the higher range resolution data generated by the Iowa XPOL radars.

5.1. COMPARISON OF 2DVD SCATTERING SIMULATIONS TO XPOL RADAR-DERIVED RELATIONS AT X-BAND

In this study, a version of the self-consistency method with constraints is used for the correction of precipitation-induced attenuation of reflectivity and differential reflectivity, as proposed by [25] at C-band, then later modified for X-band as detailed in [26, 22] and previously in Chapter 4. This "iterative ZPHI" method requires knowledge of the empirical relations between several polarimetric variables, in particular the relations of A_H - K_{DP} , A_H - A_{DP} , and A_H - Z_H . Comparisons are made between the radar-derived polarimetric relations to those of the well-known scattering simulations computed from drop spectra measured by several two-dimensional video disdrometers (2DVDs).

To validate the attenuation-corrected Z_H and Z_{DR} values from the University of Iowa XPOL radars, a comparison to the scattering simulation values calculated from drop spectra measured by six 2DVDs over four days during the NASA-GPM Iowa Flood Studies (IFloodS) field campaign in the spring of 2013. There were a total of 7,112 drop spectra collected at 1 minute intervals, encompassing a wide variety of rain types. Using a drop shape versus D (drop size diameter) relation, at a temperature of 20 C, and canting angle distribution obtained from the 80 m fall bridge experiment [36, 37], the data were fitted to a normalized gamma DSD. Using the N_w , D_0 , and μ parameters from the newly fitted DSDs, scattering simulations were obtained, at X-band wavelength ($\lambda = 3.2$ cm), employing the T-matrix

method [45]. From the resulting scattering simulations, a power-law fit was derived from the empirical relations of A_H-K_{DP} , A_H-A_{DP} , A_H-Z_H , and $Z_{DR}-Z_H$.

In Figures 5.1 and 5.2 illustrated are the scattering simulation relations overlaid on the measured and attenuation-corrected values (as intensity contour plots in $\log_{10}(\#occurrences)$) from XPOL-4 data collected during IFloodS on 12-13 June 2013 between the hours of 2107-0300 UTC. Figure 5.1 shows the comparisons between radar-derived and scattering simula-

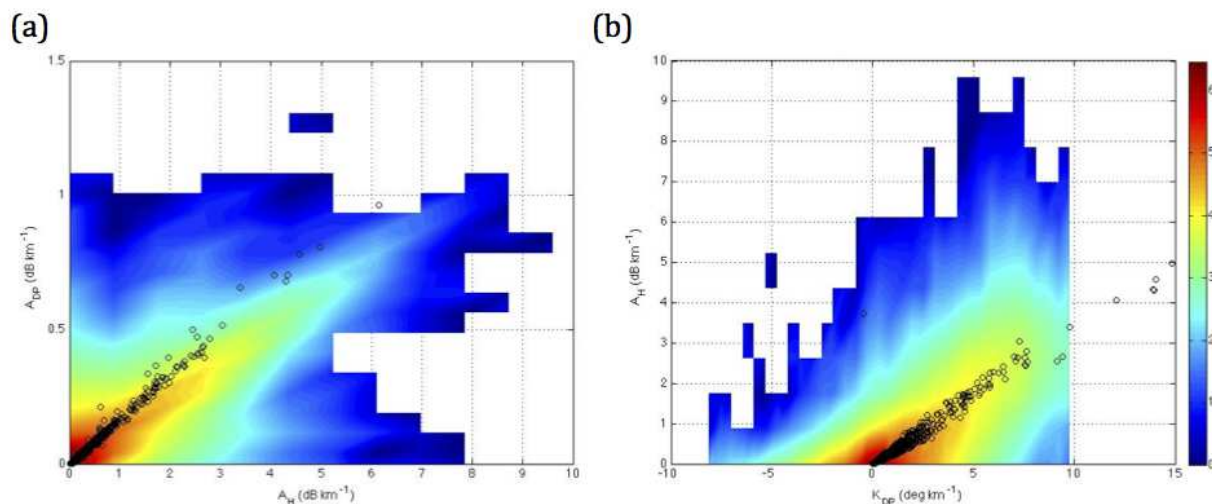


FIGURE 5.1. Intensity contour (in $\log_{10}(\#occurrences)$) plots of (a) A_{DP} vs A_H and (b) A_H vs K_{DP} . Data from XPOL-4 during IFloodS on 20130612-2107 to 20130613-0300 UTC. The overlay are disdrometer scattering simulation results, calculated for X-band from 4 days during IFloodS, for the same parameters.

tions of the (a) $A_{DP}-A_H$ and (b) A_H-K_{DP} relations. The radar-derived values show good agreement with the scattering simulations in the A_H-K_{DP} and $A_{DP}-A_H$ relations. In Figure 5.2 panel (a) when comparing to the scattering simulations of the $K_{DP}-Z_H$ relations it is obvious that for a given K_{DP} the measured reflectivity values are much smaller than expected. The same can be seen in the A_H-Z_H relation in panel (c) and the $Z_{DR}-Z_H$ relations in panel (e). After the attenuation correction procedure, the corrected Z_H and Z_{DR} there is good agreement with the predicted values of the scattering simulations, as seen in panels

(b), (d), and (f). The agreement between the corrected values and those based on scattering simulations is a good measure of validation of the attenuation-correction methodology used.

5.2. ATTENUATION CORRECTION APPLIED TO THE UNIVERSITY OF IOWA XPOL RADARS

Following the procedure outlined in chapter 4, the specific attenuation and specific differential attenuation are computed on a ray-by-ray basis to ultimately obtain the attenuation-corrected reflectivity and differential reflectivity from the measured values. Illustrated in Figure 5.3 are PPI scans of the (a) measured and (b) corrected Z_H at an elevation angle of 3° which depicts the large spatial variability in this highly convective rain cell complex at 23:34:00 UTC, on June 12, 2013. It is apparent that without attenuation correction at X-band important meteorological information is lost, and thus can lead to incorrect rain rate calculations or weather predictions/warnings. In this scan the peak corrected reflectivity is in the range of 55-60 dBZ. There was beam blockage near the radar surrounding two small azimuth sectors centered at 294° and 330° , evident in this figure.

To better illustrate the effectiveness of the attenuation corrections, vertical profile (RHI) plots were generated from a convective storm observed by XPOL-4 on 12 June 2013 at 23:32:30 UTC. Figure 5.4 shows RHI scans at $AZ=310^\circ$ with measured Z_H (panel (a)) and corrected Z_H (panel (c)). Upon close inspection of these plots the necessity for attenuation correction of Z_H (from an RHI perspective) is obvious when comparing the top and bottom panels, especially below a 4 km height (the 0C height is around this height). Moreover, the signal becomes extinct starting at a range around 14 km, at 4 km above the ground where no further correction is possible. The strong convective nature of the storm complex is evident in the tall column of high reflectivities reaching at least 8 km in height.

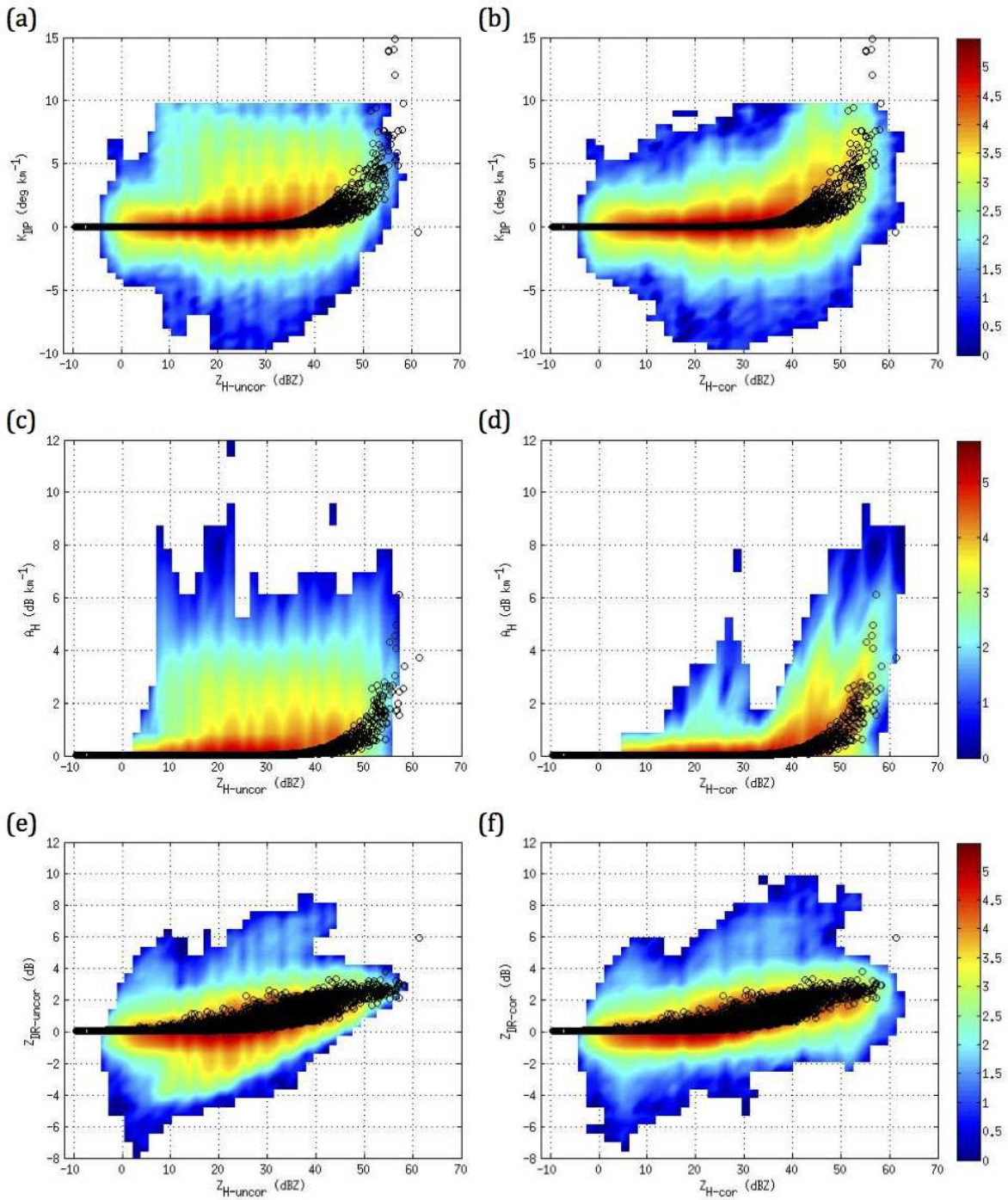


FIGURE 5.2. Intensity contour (in $\log_{10}(\#occurrences)$) plots of K_{DP} vs Z_H , A_H vs Z_H , and Z_{DR} vs Z_H . Data from XPOL-4 during IFloodS on 20130612-2107 to 20130613-0300 UTC. The overlay are disdrometer scattering simulation results, calculated for X-band from 4 days during IFloodS, for the same parameters. Plots (a), (c), and (e) are comparisons with uncorrected Z_H and Z_{DR} , while (b), (d), and (f) are with attenuation-corrected data.

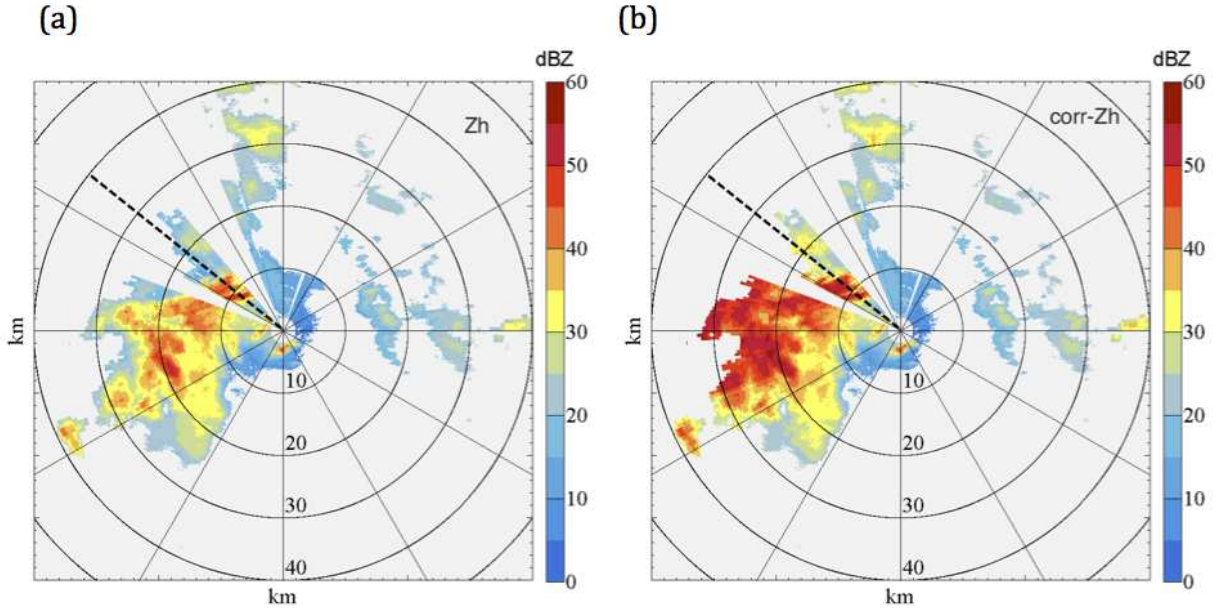


FIGURE 5.3. PPI scans of (a) measured and (b) attenuation-corrected Z_H field from 12 June 2013 at 2334:00 UTC. The origin is at the XPOL-4 radar location. The plot axes are aligned with true North/South and West/East, shown with 10 km range rings. The dashed line indicates a vertical RHI profile at azimuth=10°.

The measured and corrected Z_{DR} are similarly shown in Figure 5.4 in panels (b) and (d), respectively. Correction of measured differential reflectivity for differential attenuation is well illustrated in the vertical by comparing the top and bottom panels. It is difficult to fully correct for both attenuation and differential attenuation near the melting layer (in the 3.5 - 4 km height interval). This is a region of mixed phase, where in stratiform cells with a strong bright band we expect melting of larger, low density and dry snowflakes, but in a convective cell with a weak bright band we anticipate the melting of tiny, compact graupel, or rimed snow particles [46]. In this vertical profile, we have a convective cell, and thus the path integrated attenuation (PIA) will be the sum of that due to rain and wet ice, whereas the propagation phase, Φ_{DP} , is due to the rain component alone, and the backscatter phase, δ , to the larger drops and/or wet ice. In these situations, a Φ_{DP} constraint is not sufficient

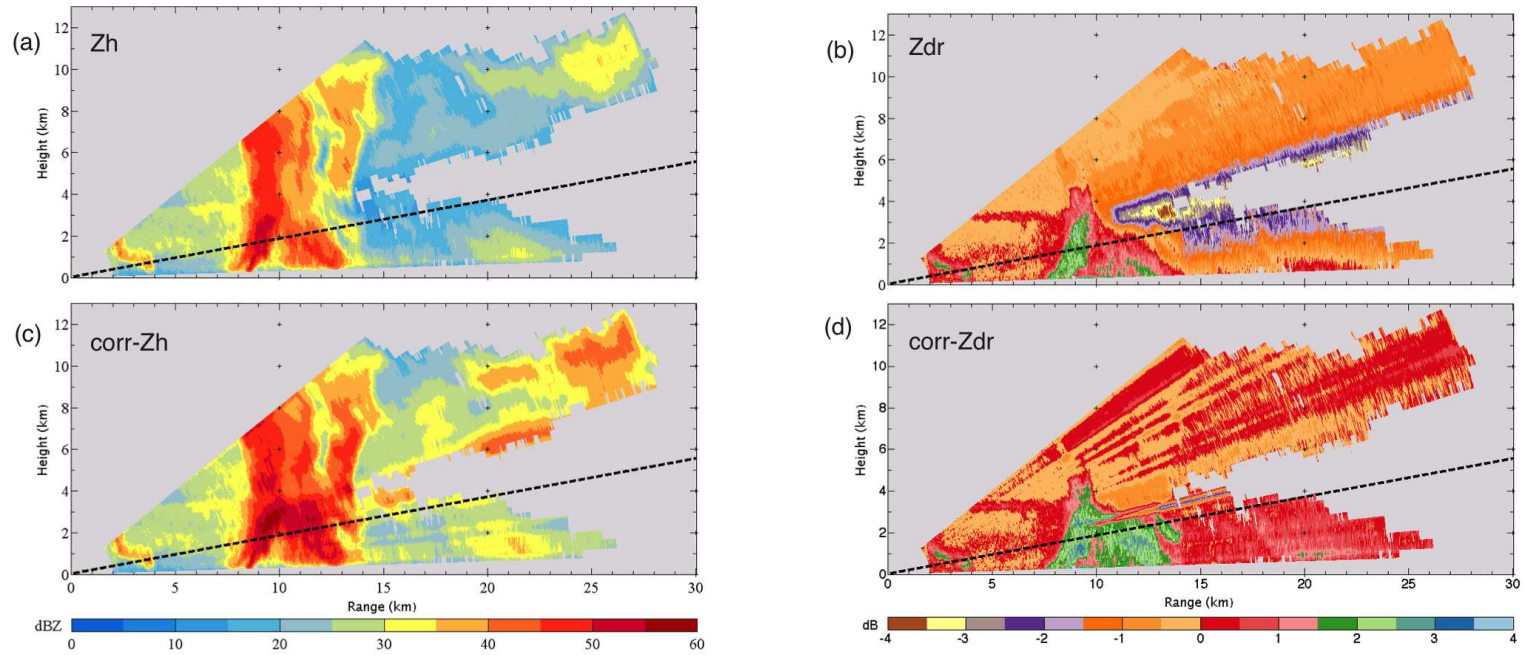


FIGURE 5.4. RHI scans of measured (panels (a) & (b)) and attenuation-corrected (panels (c) & (d)) Z_H and Z_{DR} along the $AZ=310^\circ$, from XPOL-4 radar data during IFloodS on June 12, 2013 at 2332:30 UTC, at $AZ=310^\circ$. The dashed line indicates the ray profile at an $EL=10.7^\circ$

and the investigation of dual-wavelength (e.g., S/X-band radar) techniques become necessary to separately estimate the PIA due to rain and wet snow or ice near the melting layer.

Figure 5.5 shows an RHI scan of the specific differential phase, K_{DP} , from the same date and time as the previously described RHI plots. An interesting feature is present at a range of 12 km in the vertical structure of K_{DP} , where the maximum values ($6-8^{\circ}/\text{km}$) are located aloft near 2.8 km, implying that the maximum rain water content has not yet descended to the surface. The maximum K_{DP} values correlate with reflectivities around 50 dBZ, and differential reflectivities above 2 dB, which are consistent with heavy rain. This would result in a rain rate near 60 mm/hr, but in the lowest elevation range profile a $K_{DP}=2.5^{\circ}/\text{km}$ results in $R=30$ mm/hr. In summary, the examples shown here illustrate the exceptional high quality of polarimetric radar data from the University of Iowa XPOL-4 radar.

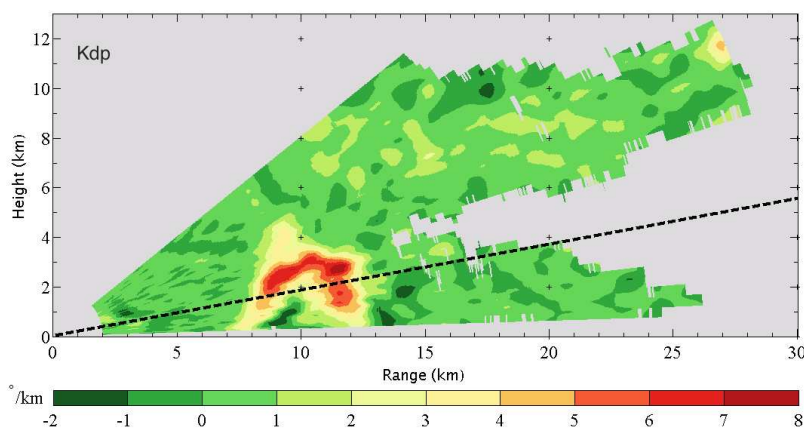


FIGURE 5.5. RHI scan of calculated K_{DP} from XPOL-4 radar during IFloodS on June 12, 2013 at 2332:30 UTC, at $AZ=310^{\circ}$. The colorbar units are in deg/km , and the dashed line indicates the $EL=10.7^{\circ}$ beam.

5.3. COMPARISON OF XPOL-2 AND XPOL-4 SCANS

In this section the attenuation-corrected, inter-XPOL comparisons of observations made in common precipitation volumes are presented, while both XPOL-2 and XPOL-4 radars were operating at a 30 m range resolution, as presented in [23]. For the IFloodS experiment, these two radars were deployed in the Turkey River Basin with a 34 km overlapping coverage area. Refer to Figure 3.2 to see the relative locations of XPOL-2 and XPOL-4 radars in northeastern Iowa, where the former is further north, and were pointed directly at each other at azimuth angles of 120° and 310° , respectively. This overlap was intentional for the recovery of potential signal extinction experienced in the outer ranges of one radar, but where valid signals exist in the near range of the other.

Consider vertical scans (RHIs) from both radars through a convective storm cell, observed one minute apart at 23:18 & 23:19 UTC on June 12, 2013, as seen in Figure 5.6 (XPOL-2 is in upper panels). Here values of corrected reflectivity, Z_{H-cor} , above 45 dBZ in the 10-20 km range and below 4 km in height are seen, while XPOL-2 experiences signal attenuation at low elevations starting around 20 km. Fortunately, XPOL-4 was able to observe most of the precipitation volume severely attenuated from XPOL-2 radar's perspective, and thus affirming the need for a networked approach when using radars with shorter wavelengths, like X-band. In the middle panels, corrected differential reflectivity, Z_{DR-cor} , confirms the convective nature of the storm complex with values at or above 2 dB below 2 km in height, where the "streaks" above 3.5 km are due to the limitations in the ZPHI method, with Φ_{DP} constraint, to separately estimate the path integrated attenuation due to rain and wet snow or ice near the melting layer. Later, dual-wavelength techniques are investigated in Chapter 6 that allow us to directly estimate the attenuation correction coefficients in rain only and in mixed-phase precipitation.

In the lower panels we see good agreement in the RHIs for estimated specific differential phase, K_{DP} , as confirmed by the congruency in the distributions of XPOL-2 and XPOL-4. Agreement in the attenuation-corrected values, Z_{H-cor} and Z_{DR-cor} , between the two radars is confirmed by congruency in their respective distributions in the overlap region enclosed by a 6-20 km range interval and a 1-5 km height, highlighted by the box in the top RHI scans. This region was selected where known good data existed with copolar correlation coefficients of $\rho_{HV} \geq 0.9$ and where the XPOL-2 signal was not fully extinct. Table 5.1 demonstrates the agreement between XPOL-2 & -4, in the standard deviations of the polarimetric estimates obtained over the selected region in this convective storm complex. It should be noted that although both radars shared the same range resolution of 30 m, XPOL-2 operated at a uniform PRT of 1000 μs , while the XPOL-4 employed a staggered PRT of 950/1200 μs . It is for this reason that we did not compare their Doppler velocities, as we expect they would not match across the two radars.

TABLE 5.1. Standard Deviations of Z_{H-cor} , Z_{DR-cor} , and K_{DP} for XPOL-2 & -4 in the overlap region enclosed by a 6-20 km range interval and a 1-5 km height of the comparative RHIs

	std of XPOL-2	std of XPOL-4
Z_{H-cor} (dBZ)	6.4571	4.8292
Z_{DR-cor} (dB)	0.5273	0.6471
K_{DP} ($^{\circ}/km$)	0.6239	0.6306

5.4. RAIN RATE COMPARISONS BETWEEN NASA RAIN GAUGES AND RADAR-DERIVED

ALGORITHMS FROM XPOL-4

In practice, rain rates from gauges are used to validate the rain rate estimates from the radars pixels directly above it, along with the four closest bins (two in range and two from the adjacent beams). This was a "rule-of-thumb" approach in selecting range bins from C- &

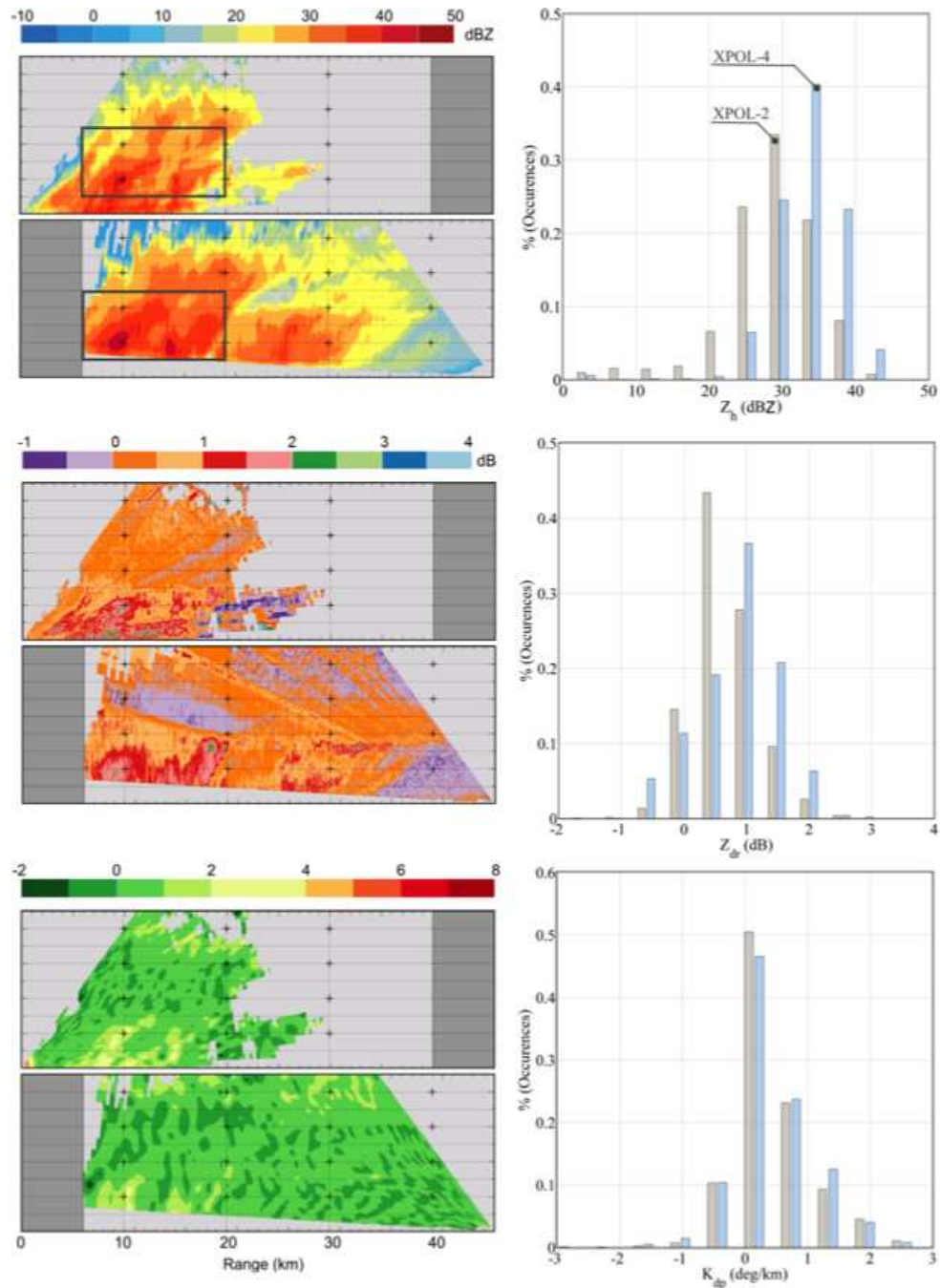


FIGURE 5.6. XPOL-2 to XPOL-4 radar intercomparison during IFloodS on June 12, 2013 at 23:18 & 23:19 UTC, respectively. Upper panels in the left column show RHIs from XPOL-2. (top) Z_{H-cor} , (middle) Z_{DR-cor} , (bottom) K_{DP} . Agreement in the attenuation-corrected values between the two radars is confirmed by congruency in their respective distributions (right column) in the overlap region enclosed by a 6-20 km range interval and a 1-5 km height, marked by the box in the top panel. Image adapted from [23]

S-band radars with range resolutions in the hundreds of meters (e.g., 150-300 m), where the selected range intervals could span 450 m to 900 m along the beam, with varying cross-beam lengths. The relatively low number of selected beams would typically capture a good areal sample of the radar-derived rain rate estimates about the rain gauge, to make an informed assessment of the validity of the rain rate algorithm in question. Unfortunately, this *ad-hoc* selection criteria may not be reasonable for weather radars with higher range resolutions of 30 m or less, like the Iowa XPOL radars. For instance, the total range interval covered along the beam will be a mere 90 meters, which may not be enough to capture the true radar-derived rain rates above a rain gauge if there is horizontal advection present that may carry the precipitation away from the rain gauge below. Figure 5.7 shows an example where the rain doesn't fall straight down, but rather falls away to the right as observed by the camera.



FIGURE 5.7. Advection is visible as rain falls to the right in this photo taken during a recent Northern Colorado spring thunderstorm. When analyzing high resolution (30 m or less) radar derived rain rates, this effect suggests we cannot only select range bins directly above and adjacent to the rain gauges for comparison, but rather select the nearest neighbor bins with minimal errors to in situ rain rates measured on the ground. (Photo by M. B. Galvez, May 2, 2015).

For this reason, we propose using a Nearest Neighbor selection criteria for choosing the range bins which most contribute to the radar-derived rain rates for validation purposes. For this analysis selected are two NASA gauge locations, 32A&B and 43A&B (see Figure 5.8), to demonstrate the proposed comparisons of four XPOL radar derived algorithms, namely the relations of $Z_{H-lin} - R$, $R(A_H)$, $R(K_{DP})$, and $R(Z_{DR-lin}, A_H)$. The first step is locating the distance and bearing of each NASA rain gauge relative to the XPOL radar. Next, it is important to locate the center of every pixel (see the \diamond 's), as opposed to its starting azimuth (see the \square 's). Using the center of the pixel ensures that at least 50% of its area lies within the radius of influence, and may therefore be selected by the Nearest Neighbor algorithm as a possible contributor to the radar-derived rain rate estimate. This method does not guarantee a completely filled circle of influence. It is evident from the zoomed-in areas that the number of range bins within a 500 meter radius of the gauges, depends on its proximity to the radar, where Gauge 43 has four beams fall inside the radius of influence, while only two lie near Gauge 32. The cross-beam or sector length of any particular range gate can be computed as, $l_{sector} = \Theta_{BW} * r_{bin}$, where Θ_{BW} is the antenna beam width in radians, and r_{bin} is the distance to the range bin. The number of range pixels selected will affect the distribution and variability of the radar-derived estimate to be compared to the point measurement of the rain gauge.

Figure 5.9, shows an example comparison between NASA Gauges 43 A&B and XPOL-4 radar-derived rain rates estimated using the $R(A_H)$ relation, which is a power-law fit from 2DVD scattering simulations. The time series shows good agreement between the 1-minute rain rates from the dual tipping bucket gauges, Gauge A (black "+") and Gauge B (red \square), which indicates a good reference for validating the radar's algorithms. The XPOL-4 radar-derived rain rates are at 7-minute intervals, with the occasional total signal extinction

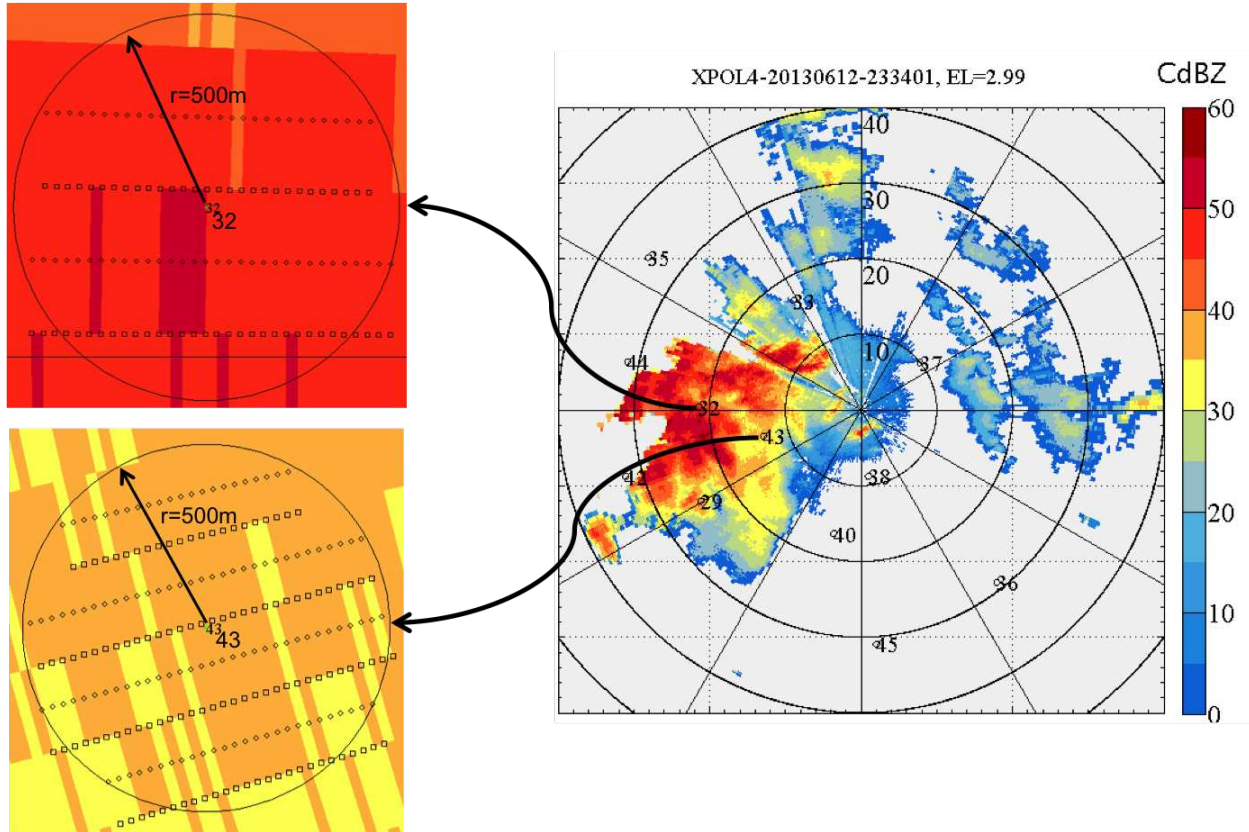


FIGURE 5.8. XPOL-4 Z_{H-cor} PPI plot of an inbound convective storm, highlighting the locations of 12 NASA dual tipping rain gauges within its 40 km unambiguous range. A blow-up is shown for Gauges 32 and 43, which are used to illustrate the nearest-neighbor selection criteria for range bins within a radius $r_{nn} < 500m$ of the gauges. The \square 's represent the starting azimuth of the range bin, and the \diamond 's the center of the bin. Radar data from XPOL-4 during IFloodS on 20130612-2334 UTC.

due to high $Z_{H-cor} > 55$ dBZ, like at 23:53 UTC, as verified in Figure 5.10. In the time series, radar-derived rain rates are represented with slim filled box plots (in blue) to provide a sense of the distribution of the nearest neighbors, within a 500 m radius of the NASA A&B gauges. The box plots show the maximum, minimum, median (circle with a dot), the 75th and 25th percentiles (top and bottom of filled box), as well as any points considered outliers of the distribution. Also highlighted on each box plot is the range bin, or pixel, nearest to the location of the rain gauge (blue \diamond) on the ground below. Each gauge is installed at a point on the ground and its location is a straight-line distance from the radar, while the

individual radar data range bins are actually volumetric representations (enclosed by the 1x1 degree beamwidth of the antenna) at a height above the ground, with respect to the radar antenna height. Because of the finite fall velocities, there will be some time delay - of a few minutes - from the radar pixel height to ground level where the gauges are located (for details on computing fall velocities, see Thurai and Bringi's section 10.5 in [8]).

Figures 5.11 and 5.12 show the variability in radar-derived rain rates, from the four rain rate algorithms previously mentioned. In the comparisons to both gauges (32 & 43), it is clear that estimates derived using $R(K_{DP})$ and $R(A_H)$ show good agreement with the ground-based measurements, while the Z-R and $R(Z_{DR}, A_H)$ estimates under- or over-estimated rain rates, respectively. It should be noted that although the $R(Z_{DR}, A_H)$ algorithm showed the least variability in the scattering simulations (see Figure 3.12), it is the most susceptible to measurement and attenuation-correction errors in Z_{DR-cor} , as evident in the computed over estimates. The Z-R algorithm made good estimates in low rain rates, and could be used in a composite rain rate algorithm where estimates of moderate to high rain rates can be derived from $R(K_{DP})$ or $R(A_H)$. It should be noted in various of the rain rate algorithm comparisons, the bin nearest to the gauge (blue \diamond) was well outside the 75%- and 25%-iles of the values estimated from pixels within the 500m radius of influence, that were close to the gauge measurements. This provides evidence of the effects due to advection, and for the need of a nearest-neighbor selection criteria of pixels in radar-derived to rain gauge rain rate comparisons, for radars operating at high spatio-temporal resolutions.

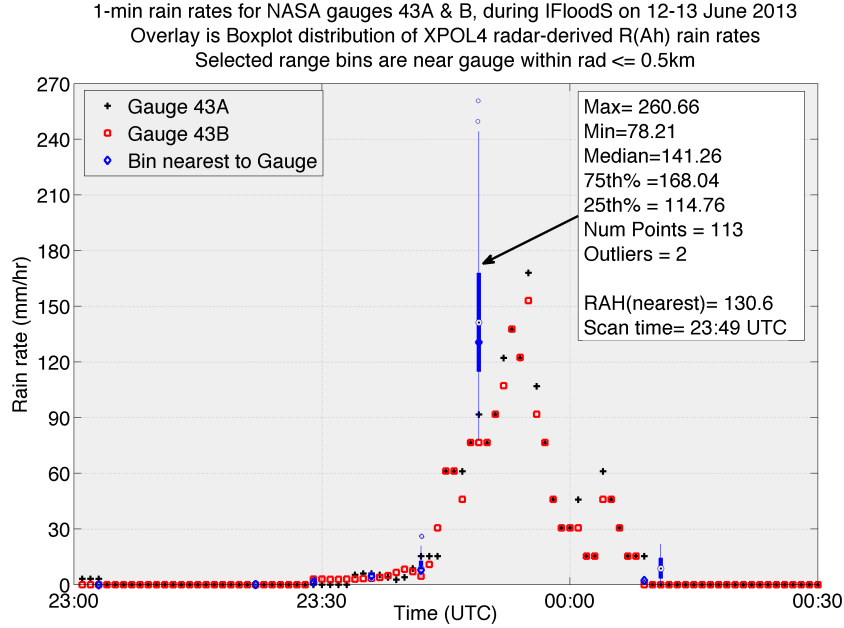


FIGURE 5.9. Comparison of XPOL-4 nearest-neighbor range bins ($r_{nn} < 500m$) of radar-derived Rain rates to NASA dual tipping bucket Gauge 32 A&B. Rain Rates are computed using the $R(A_H)$ relation. Radar data from XPOL-4 during IFloodS on 20130612-13.

5.5. APPLICATION OF TWO-STAGE FIR RANGE FILTER TO XPOL DATA COLLECTED DURING IFLOODS FOR IMPROVED DIFFERENTIAL BACKSCATTER PHASE " δ " ESTIMATION

In this section, the effectiveness of the 75 m lowpass Butterworth FIR range filter, proposed by [34], is investigated when applied to the 30 m range resolution data of the XPOL radar systems. For comparison, we designed a 40th order Kaiser lowpass FIR range filter tuned to 30 m intervals, and found it had similar performance to the 75 m FIR filter when applied to 30 meter range resolution data. For reference, the 75 meter filter was initially developed for polarimetric weather radars with range resolutions of 75 meters and greater. Evidence of their similarities can be seen in Figures 5.13 and 5.14 when applying the filters to XPOL-4 range profiles of measured co-polar differential phase, which suggests the newly

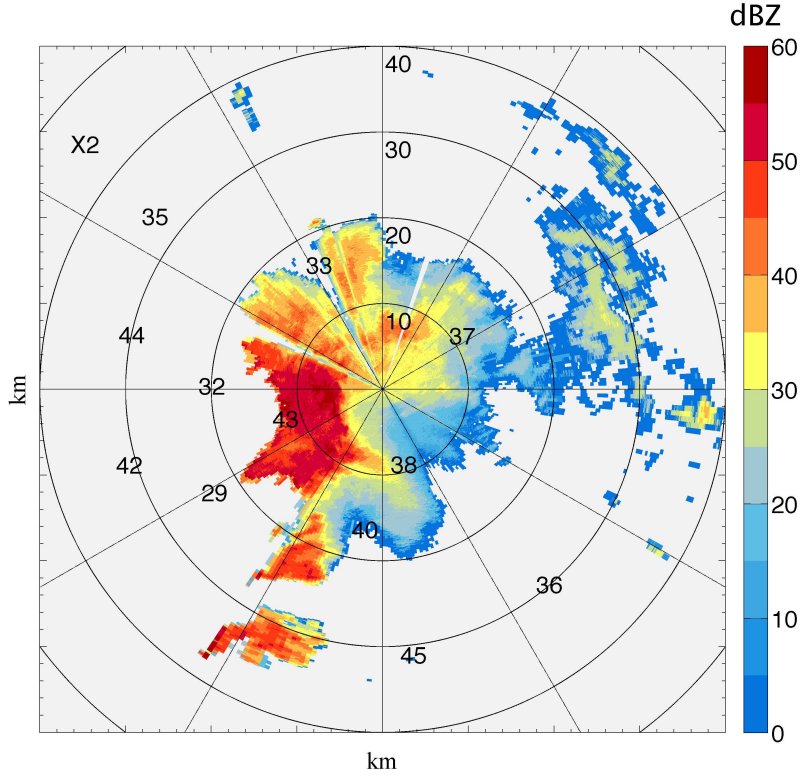


FIGURE 5.10. Signal Extinction starting around 11.5 km W-SW of XPOL-4 during IFloodS field campaign on 20130612-2353 UTC. This resulted in the absence of received signal to compute radar-derived rain rates for comparison to NASA Gauges 43, 32, 29, 42, and 44, at or around this time.

designed FIR30m-40 Kaiser filter was a good choice to easily replace the lowpass Butterworth FIR filter.

By evaluating their ability to mitigate the "bumps," due to Mie scattering, in a monotonically increasing raw co-polar differential phase, Ψ_{DP} , the poor performance of both 40th order filters is evident. We then designed a 100th order 30 m Kaiser FIR lowpass filter to better mitigate the local perturbations in Ψ_{DP} , potentially due to differential backscatter phase (δ), specifically for the higher 30 m range resolution data of the XPOL radar systems. Figure 5.15, highlights the FIR30m-100 filter's improvements, where after applying the iterative filtering technique [34] now converges only after 3-4 iterations. In order to prevent

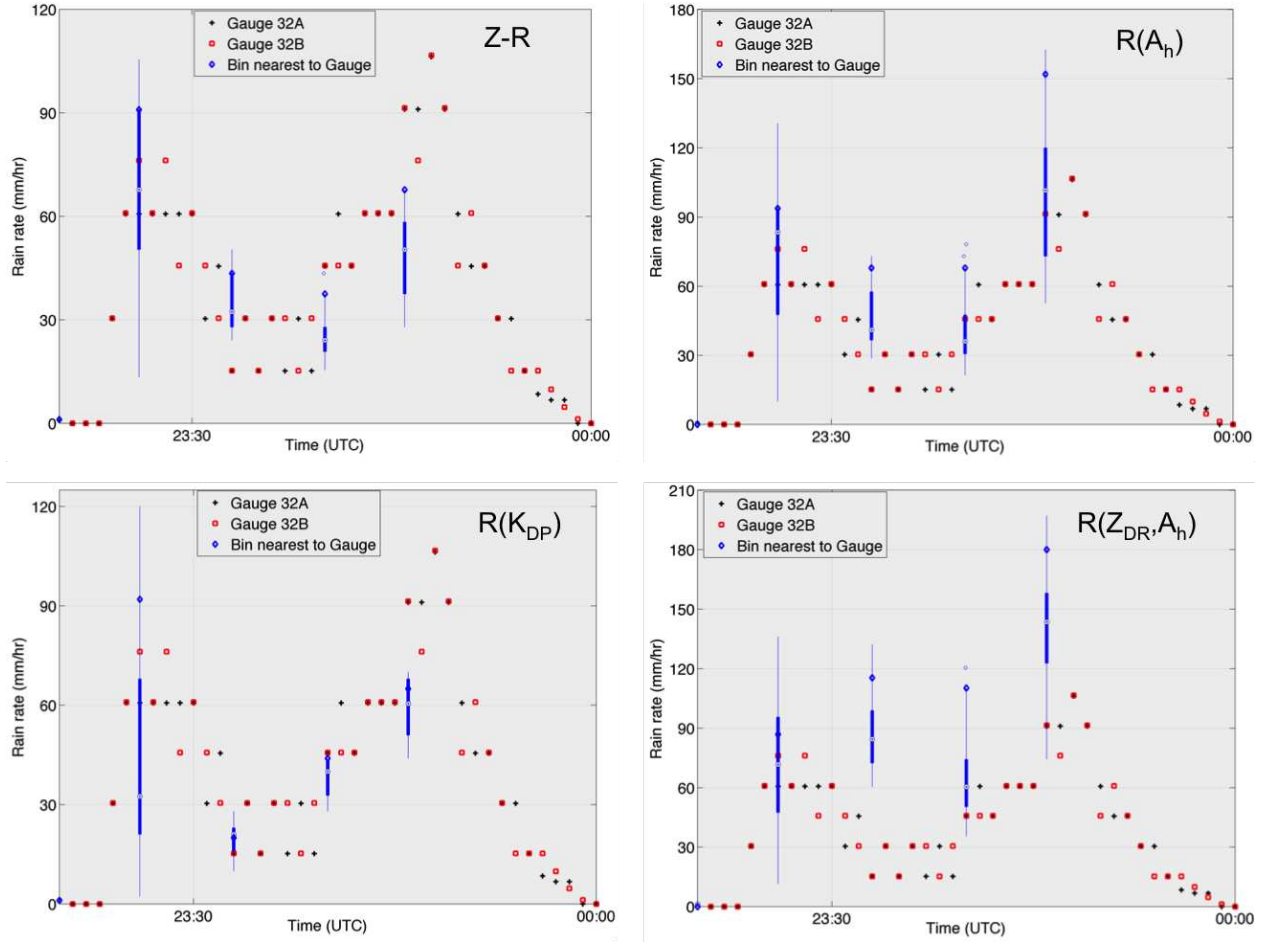


FIGURE 5.11. Comparison of XPOL-4 nearest-neighbor range bins ($r_{nn} < 500m$) of radar-derived Rain rates to NASA dual tipping bucket Gauge 32 A&B. Rain Rates are computed using the following relations: $Z_{H-lin} - R$ (top left), $R(A_H)$ (top right), $R(K_{DP})$ (bottom left), and $R(Z_{DR-lin}, A_H)$ (bottom right). Radar data from XPOL-4 during IFloodS on 20130612-2334 UTC, and shifted by +4 minutes to account for drop fall-time from a height of approximately 1.122 km.

over-smoothing of the filtered Φ_{DP} by the FIR30m-100 filter, a two-stage filtering scheme (see Chapter 4 for details) was employed.

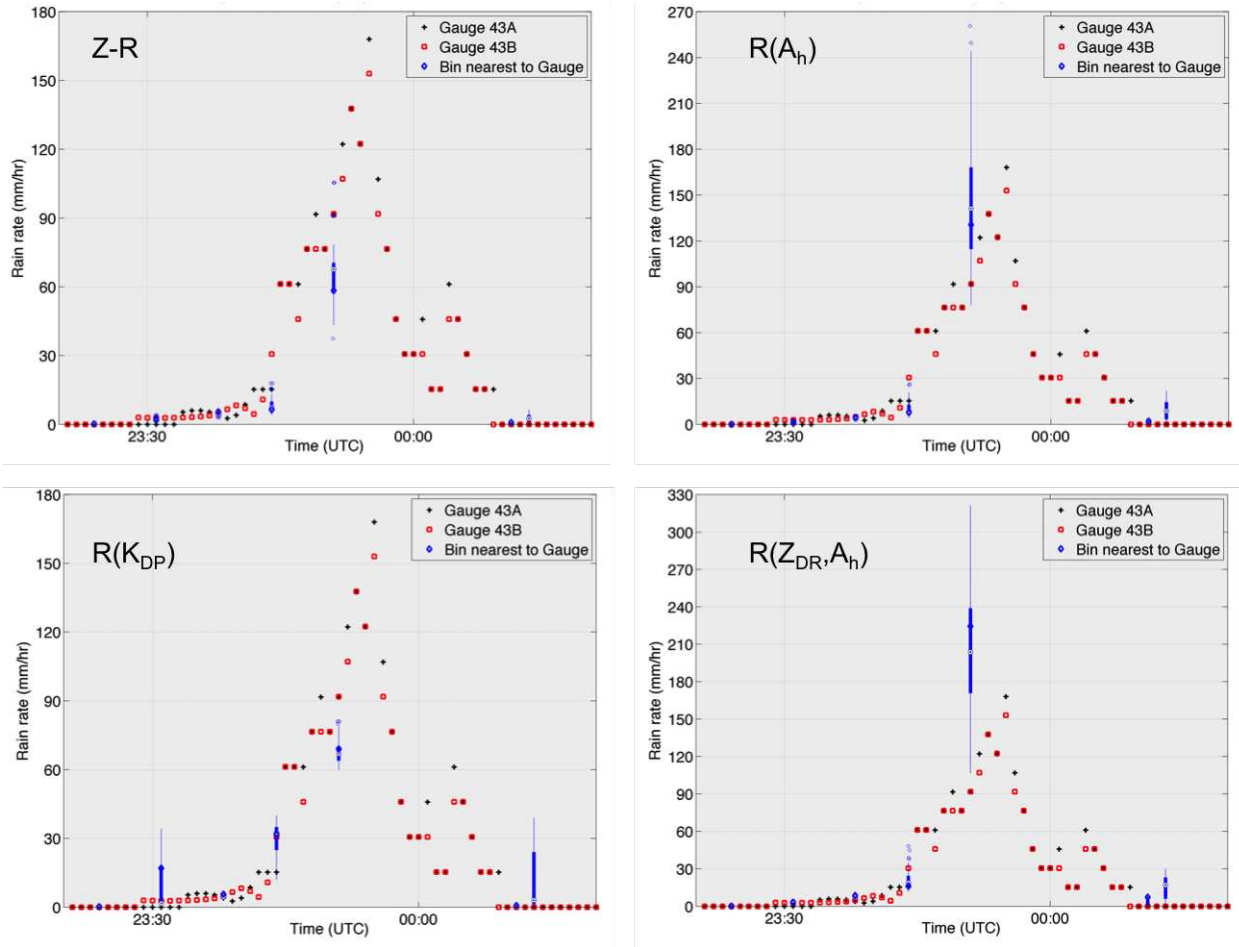


FIGURE 5.12. Comparison of XPOL-4 nearest-neighbor range bins ($r_{nn} < 500m$) of radar-derived Rain rates to NASA dual tipping bucket Gauge 43 A&B. Rain Rates are computed using the following relations: $Z_{H-lin} - R$ (top left), $R(A_H)$ (top right), $R(K_{DP})$ (bottom left), and $R(Z_{DR-lin}, A_H)$ (bottom right). Radar data from XPOL-4 during IFloodS on 20130612-2334 UTC, and shifted by +2 minutes to account for drop fall-time from a height of approximately 0.633 km.

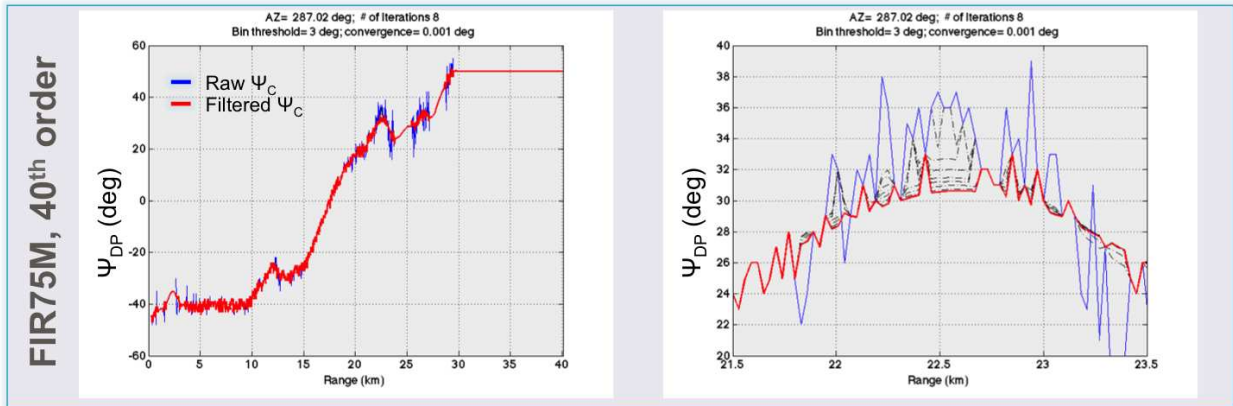


FIGURE 5.13. Application of the 75 m, 40th order Lowpass Butterworth FIR filter to a Φ_{DP} range profile through a convective storm, with evidence of Mie backscattering between 20-24 km. Radar data from a low elevation ($EL = 3^\circ$) XPOL-4 PPI scan, at $AZ = 287^\circ$, during IFloodS on 20130612-2327 UTC.

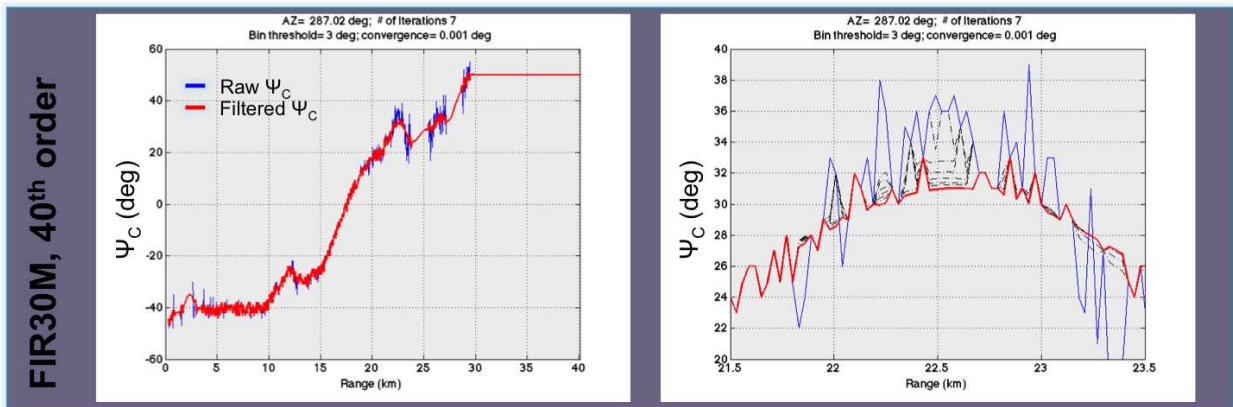


FIGURE 5.14. Application of the 30m, 40th order Lowpass Kaiser FIR filter to a Φ_{DP} range profile through a convective storm, with evidence of Mie backscattering between 20-24 km. Radar data from a low elevation ($EL = 3^\circ$) XPOL-4 PPI scan, at $AZ = 287^\circ$, during IFloodS on 20130612-2327 UTC.

FIR30M, 100th order

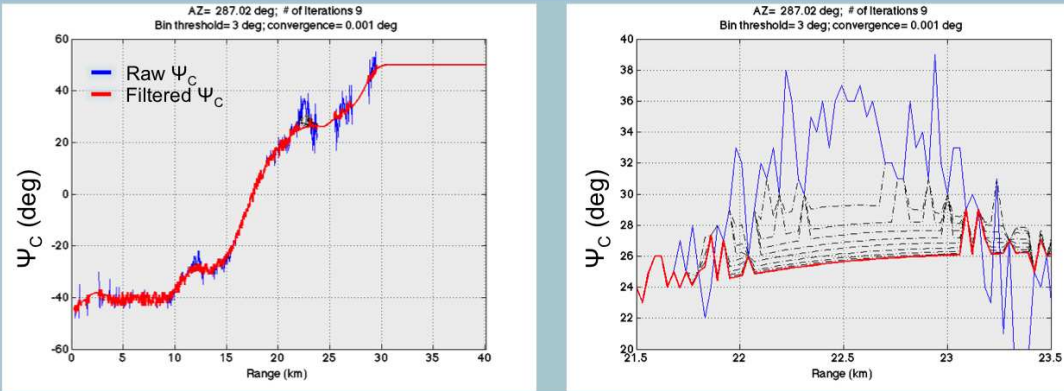


FIGURE 5.15. Application of the 30m, 100th order Lowpass Kaiser FIR filter to a Φ_{DP} range profile through a convective storm, with evidence of Mie backscattering between 20-24 km. Radar data from a low elevation ($EL = 3^\circ$) XPOL-4 PPI scan, at $AZ = 287^\circ$, during IFloodS on 20130612-2327 UTC.

CHAPTER 6

DUAL WAVELENGTH RATIOS OF REFLECTIVITY & DIFFERENTIAL REFLECTIVITY

The accuracy of dual-wavelength techniques depend on proper matching of the S- and X-band radar beam resolution in azimuth, elevation, radial range spacing, and timing of the pulse triggering between the two systems. As described in Chapter 2, the CHILL S/X-band radar signals share the same antenna, although with 1 deg beamwidth at S-band and about 0.3 deg at X-band with a higher gain. For the analysis herein we synthesize the higher resolution X-band beam width to match the S-band beam, with an approximately 3:1 beam ratio (X:S). Aside from hail detection, the dual-wavelength ratio allows for using the virtually unattenuated S-band reflectivity measurement as a constraint in the attenuation correction algorithm that can be applied directly to the measured X-band data. We focus on the attenuation correction aspect of the dual-wavelength ratios and the variability of the α & β coefficients with height, in rain-only, and in rain/hail mixtures.

6.1. DESCRIPTION OF DUAL WAVELENGTH ANALYSIS PROCEDURE

We investigate dual-wavelength algorithms to directly estimate the α and β coefficients, of the $A_H = \alpha K_{DP}$ and $A_{DP} = \beta K_{DP}$ relations, to obtain the path integrated attenuation due to rain and wet ice or snow in the region near the melting layer. We use data from the dual-wavelength, dual-polarization CHILL S-/X-band Doppler weather radar for analyzing the coefficients and compare their variability as a function of height, where the hydrometeors are expected to go through a microphysical transformation as they fall, starting as snow or graupel/hail then melting into rain or a rain-hail mixture. The S-band signal is un-attenuated

and so forms a reference for estimating the X-band attenuation and differential attenuation. We present the ranges of the α and β coefficients in these varying precipitation regimes to help improve KDP-based attenuation correction algorithms at X-band as well as rain rate algorithms based on the derived specific attenuation, A_H . One such rainfall estimation algorithm, $R(A_H)$, was presented by [19] and tested at X-band to include mitigation of partial beam blockage and also in a networked radar configuration.

Figure 6.1 shows RHI scans of reflectivity at (a) S-band Z_{H-S} and (c) X-band, Z_{H-X} , and their corresponding differential reflectivities (b) Z_{DR-S} and (d) Z_{DR-X} observed by the CSU-CHILL S/X-band radar at an azimuth angle of 291° . These scans were through a mostly rain-only event observed on 18 July 2013 at 22:10 UTC, and was previously identified as such in a study presented by [7]. We can see reflectivity values greater than 40 dBZ at heights at or above 3 km in both reflectivity plots, while it is evident how the effects of attenuation diminish Z_{H-X} beyond 30 km in range, as it propagates through the heavier rainfall. The effects of attenuation on Z_{DR-X} are apparent in the image as the "negative Z_{DR} shadow" cast beyond 30 km range, due to Z_H attenuating more than Z_V (where $Z_{DR} = Z_H - Z_V$), as the pulse propagates through a medium composed of larger oblate rain drops. It is in these regions of attenuation at X-band that we can directly estimate the coefficients and correct for specific and differential attenuation from the $A_H = \alpha K_{DP-X}$ and $A_{DP} = \beta K_{DP-X}$ relations.

To demonstrate the application of the dual-wavelength procedure, we select a beam that propagates through rain only, and below the melting layer, so we consider the range profile at an elevation of 1.7° , as highlighted by the black line in the RHIs. We estimate the α and β coefficients directly from the dual-wavelength equations (2.19) and (2.20) defined in Chapter 2. Figure 6.3 shows range profiles of (a) Z_{H-S} and Z_{H-X} vs Φ_{DP-X} , (b) Z_{DR-S}

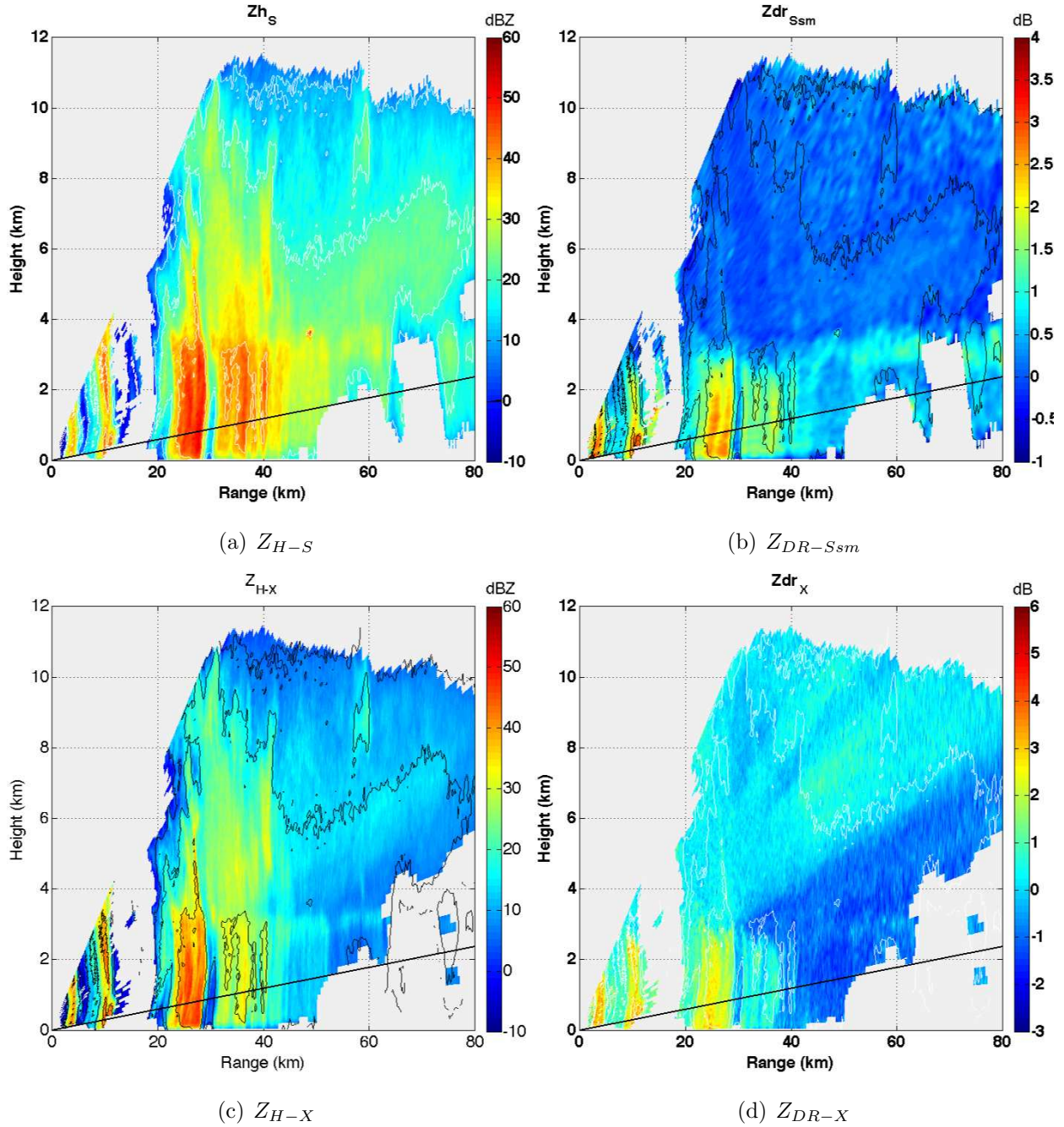


FIGURE 6.1. CSU-CHILL RHI scans at $AZ=291^\circ$ for S-band: (a) Z_{H-S} and (b) Z_{DR-Ssm} , and at X-band: (c) Z_{H-X} & (d) Z_{DR-X} observed on 18 July 2013 at 2210 UTC. The black line shows the range profile at $EL=1.7^\circ$ to be analyzed for Dual wavelength attenuation correction at X-band.

and Z_{DR-X} vs ρ_{HV} , where we can see on a ray basis where attenuation at X-band is first experienced between 25-30 km. The dual-wavelength reflectivity and differential reflectivity,

along with differential phase at X-band, are shown as raw data in (c) DWR_Z vs Φ_{DP-X} , and (d) Δ_{Zdr} vs Φ_{DP-X} . After direct application of the dual-wavelength equations, we get (c) $\alpha=0.375$ dB/deg, while the specific differential attenuation coefficient from panel (d) is $\beta = 0.058$ dB/deg. Both of these estimates are within the expected intervals at X-band for rain only, as presented by [22].

6.2. DWR-DERIVED α AND β COEFFICIENT VARIABILITY WITH HEIGHT IN RAIN AND MIXED PHASE PRECIPITATION

In this section, we investigate the variability of the α and β coefficients derived directly from dual-wavelength ratios, as a function of height and precipitation type. As previously mentioned, dual-wavelength algorithms are employed to directly estimate the α and β coefficients to obtain the path integrated attenuation due to rain and wet ice or snow in the region near the melting layer. It is important to understand the variability in the coefficients, due to precipitation type, since the attenuation correction procedure used herein, i.e., the ZPHI method with Φ_{DP} constraints, as proposed by Park et al. (2005 I&II), is optimized for rain only events. Presented are the ranges of the α and β coefficients in these varying precipitation regimes to help improve KDP-based attenuation correction algorithms at X-band as well as rain rate algorithms based on the derived A_H .

A few vertical scans of a convective storm complex observed by the dual-wavelength, dual-polarization CSU-CHILL S-X band radar in the summer of 2013 have been selected. In these RHI scans, there are areas of heavy rain, rain mixed with hail, and in some regions of hail aloft. Figure 6.2 shows RHI plots of the reflectivities at S&X bands, Z_{H-S} and Z_{H-X} , in the left column, while the dual-wavelength reflectivity (DWR) and specific differential phase at X-band, K_{DP-X} are in the right column. Regions of high reflectivity (starting near

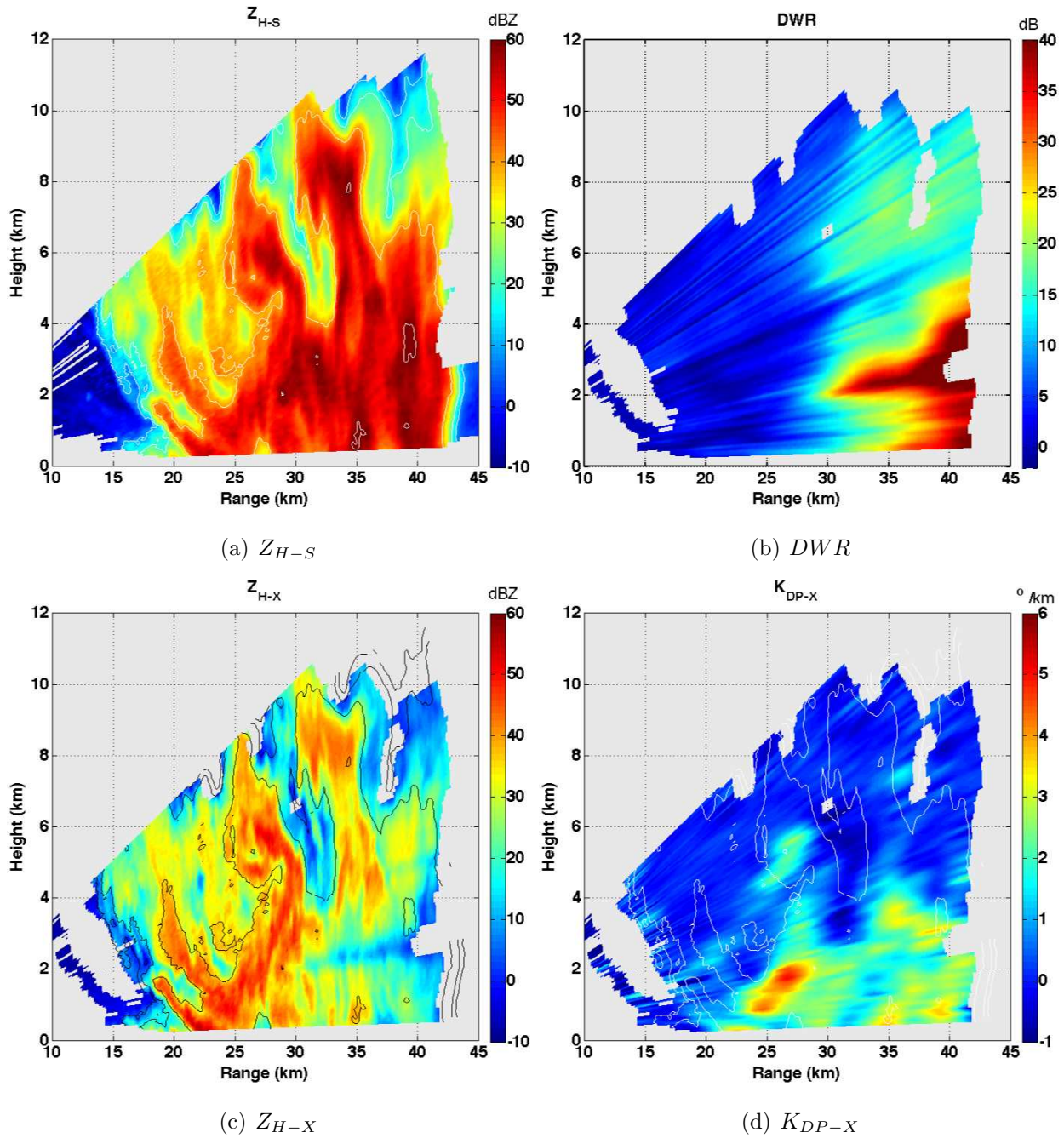


FIGURE 6.2. (a) Z_{H-S} RHI showing a convective storm with high reflectivities above 50 dBZ up to 8 km above ground; (c) Z_{H-X} showing attenuation starting at 25 km and beyond; (b) dual-wavelength ratio, $DWR = Z_{H-S} - Z_{H-X}$; (d) K_{DP-X} indicating heavy rain around 25 km, below 2 km height. Data collected from a CSU-CHILL S-X RHI scan, at $AZ = 291^{\circ}$, on 20130803-2142 UTC.

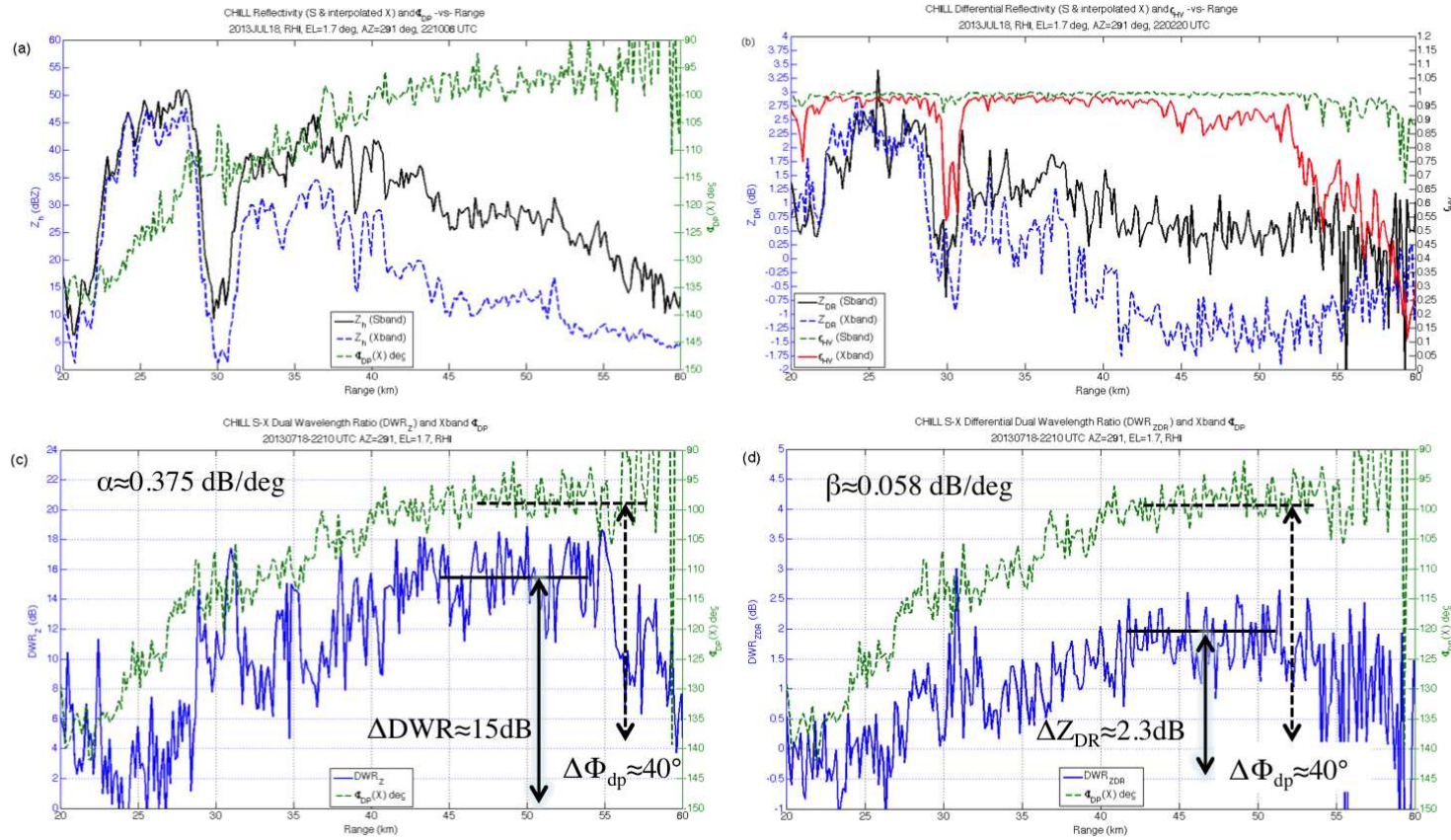


FIGURE 6.3. CSU-CHILL S/X-band range profiles from RHI scans at $AZ=291^\circ$ & $EL=1.7^\circ$, observed on 18 July 2013 at 22:10 UTC for (a) Z_{H-S} and Z_{H-X} vs Φ_{DP-X} ; (b) Z_{DR-S} and Z_{DR-X} vs ρ_{HV} ; (c) DWR_Z vs Φ_{DP-S} ; (d) ΔZ_{DR} vs Φ_{DP-X} . Estimated coefficients are, $\alpha = 0.375$ dB/deg; $\beta = 0.058$ dB/deg

30 km in radial range) are evident in the Z_{H-S} plot, and the rapidly attenuating signal in the Z_{H-X} plot. The dual-wavelength reflectivity shows the degree of accumulating path integrated attenuation as the beams propagate through the volumes filled with larger oblate hydrometeors, with peak attenuation beyond 30 km and above 2.5 km in height. We take advantage of the more sensitive differential propagation phase at X-band, which is immune to the effects of attenuation (unless the signal is extinct), to detect areas of heavy rainfall like that seen around 25 km in range. From these RHIs, coupled with the computed Hail Detection Ratio (HDR, not shown) we were able to identify regions of uniform rain (25-30 km), as well as rain-hail mix and hail aloft regions (30-35 km) for analysis of the variability in α and β with height, and through the different precipitation regimes.

6.2.1. DUAL-WAVELENGTH DERIVED α COEFFICIENT IN UNIFORM RAIN AND RAIN-HAIL MIXED PHASE REGIONS. First, the α coefficient is computed in "rain-only" regions between the range interval of 25-30 km, applying the dual-wavelength technique previously described. In Figure 6.4, we show the vertical profiles, averaged over the range interval (25-30km), of reflectivity and differential reflectivity at S-band, Z_{H-S} & Z_{DR-S} , along with those for specific attenuation and specific differential phase at X-band, A_{H-X} and K_{DP-X} . This indeed is a heavy rainfall with high reflectivities and positive Z_{DR-S} values seen up to 5.5 km. The relatively low Mie signal (upper right panel) below 5 km height indicates the absence of melting snow/hail which could lead to the presence of differential backscatter phase signal. The α -vs-height profile is that for a purely rain only event below 3 km, with values near that computed from 2DVD scattering simulations, at $\alpha \approx 0.3$ dB/deg. There is good agreement between the $\alpha = A_{H-X}/K_{DP-X}$ relation in the vertical profile and the dual-wavelength derived α coefficient as a function of height. This behavior of increasing α with

height is expected as we get into regions of mixed phase where wet quasi-spherical frozen particles produce a lower Φ_{DP-X} , positively biasing the inversely proportional coefficient.

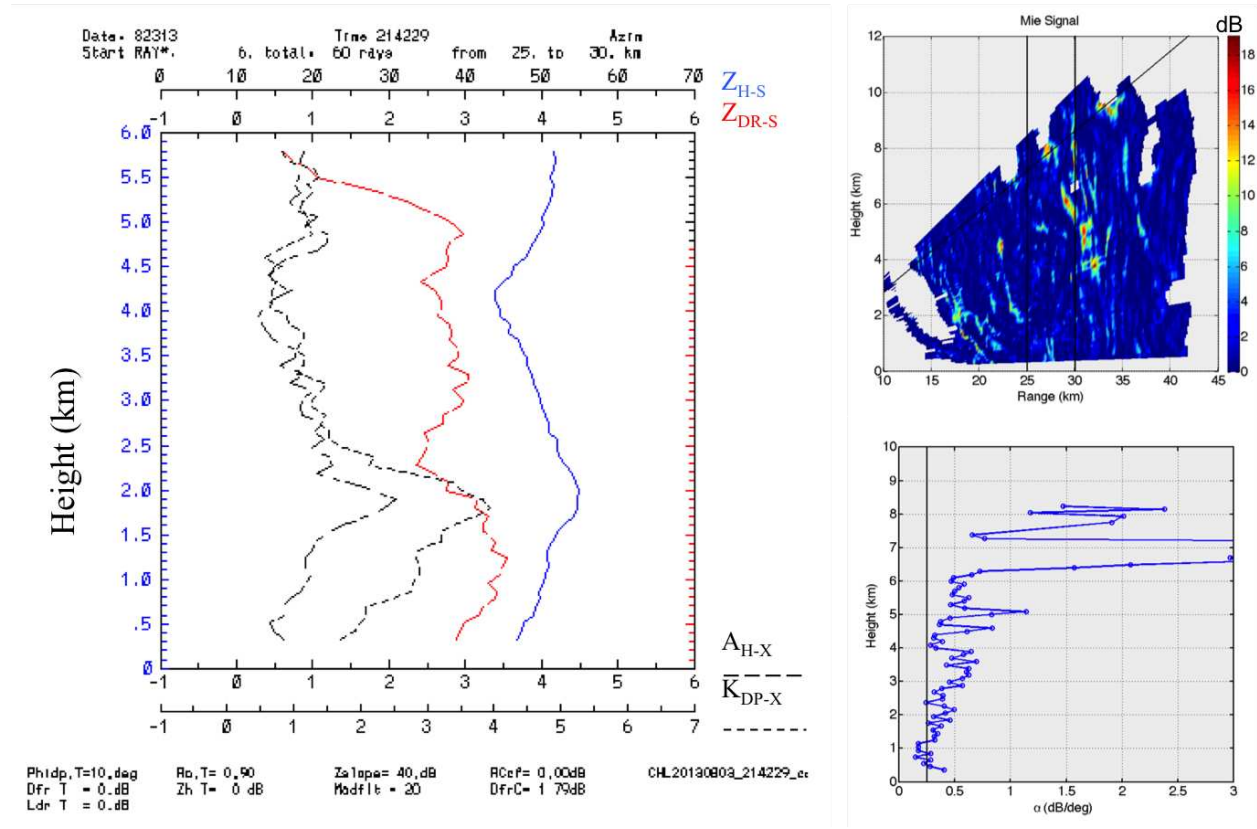


FIGURE 6.4. α vs. height in Rain-only. (left) Vertical profiles, between range=25-30 km, of Z_{H-S} , Z_{DR-S} , A_{H-X} , and K_{DP-X} from a CHILL S-X RHI scan, at $AZ = 291^\circ$, on 20130803-2142 UTC; (top right) low Mie scatter signal over the range interval; (bottom right) α coefficient estimated, over the range interval between 25-30 km on a ray-by-ray basis, using the direct $\alpha = \Delta DWR / \Delta \Phi_{DP-X}$ method. This was determined to be a "Rain-only" region below 3 km in height, which was confirmed with $\alpha \approx 0.3 \text{ dB/deg}$ and the low Mie signal, as expected.

In Figure 6.5 we consider estimation of the α coefficient in the rain-hail mixed phase range interval between 30-35 km, showing (left panel) the vertical profiles of Z_{H-S} , Z_{DR-S} , A_{H-X} , and K_{DP-X} ; (top right) the Mie signal RHI scan indicating mixed-phase hydrometeors above 3 km; and (bottom right) the DWR-derived α coefficient as a function of height. The radar data used for this analysis is from a CSU-CHILL S-X RHI scan, at $AZ = 291^\circ$, as observed

on 3 August 2013 at 21:42 UTC. For reference, the vertical profile shows high reflectivities and positive Z_{DR-S} below 2.5 km, and a hail aloft signature with near-zero values above 3 km (see also Figure 6.6). The estimated α coefficients in this region are clearly higher than in the rain-only range interval, in addition showing increased variability over the same height intervals. Here the coefficients from the $\alpha = A_{H-X}/K_{DP-X}$ relation are higher due to significant attenuation in the lowest height intervals of the vertical profile, compared to the rain-only interval. Again, we see an increase in the coefficient above 3 km as a result of the rapidly decreasing K_{DP-X} relative to the derived A_{H-X} , with exception to the decrease in α 's between 5-7 km where the specific differential phase at X-band goes negative.

6.2.2. DUAL-WAVELENGTH DIFFERENTIAL REFLECTIVITY DERIVED β COEFFICIENT IN RAIN ONLY. Referring to the same convective event observed by the CSU-CHILL S/X-band radar on 3 August 2013 at 21:42 UTC for the β vs. height analysis. In Figure 6.6 we have RHI plots of the differential reflectivities at S- & X-bands, Z_{DR-S} and Z_{DR-X} , in the left column, while the dual-wavelength differential reflectivity (ΔZ_{DR}) and specific differential phase at X-band, K_{DP-X} are in the right column. Easily detected is the convective precipitation in regions of high differential reflectivity (mostly below 2 km) in the Z_{DR-S} plot (upper left), and the rapidly attenuating signal (with range) in the Z_{DR-X} plot (lower left). Severe differential attenuation is evident at X-band, starting near 25 km in range, and rapidly degrading beyond 30 km into the "negative Z_{DR} shadow." For this analysis the X-band signal had a minimum threshold of $Z_{DR-X} > -3$ dB, limited by the signal processing hardware. In the upper right, the ΔZ_{DR} shows the degree of accumulating path integrated differential attenuation, $A_{DP-X}(\approx \Delta Z_{DR})$ as the beams propagate through precipitation volumes filled with larger oblate hydrometeors. For the β coefficient analysis we avoid regions with hail only because the quasi-spherical shapes will result in near-zero specific differential

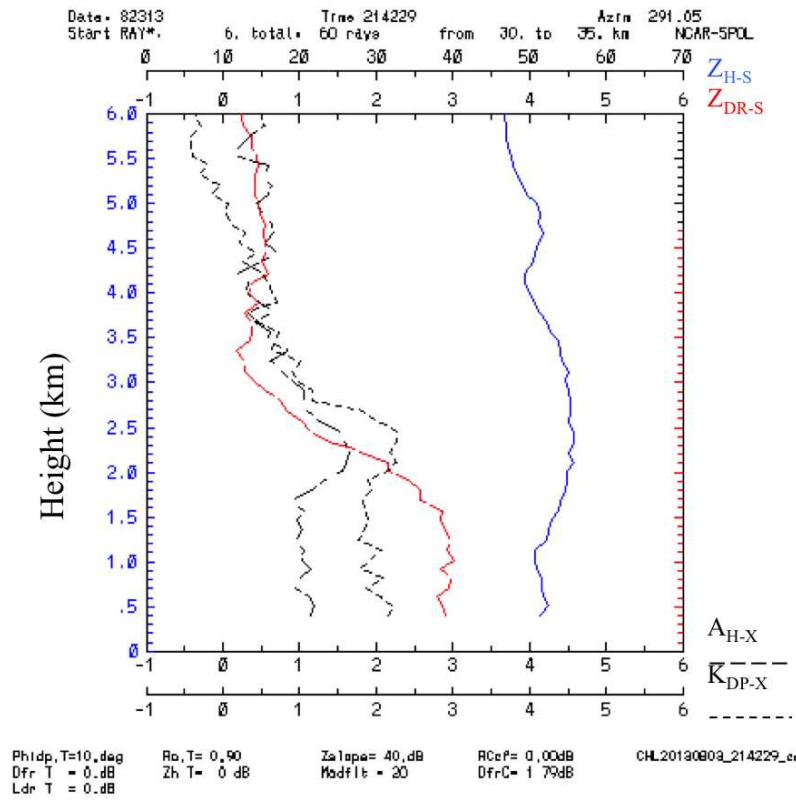


FIGURE 6.5. α vs. height in Rain-Hail mix. (left) Vertical profiles, between range=30-35 km, of Z_{H-S} , Z_{DR-S} , A_{H-X} , and K_{DP-X} from a CSU-CHILL S-X RHI scan, at $AZ = 291^\circ$, on 20130803-2142 UTC; (top right) high Mie scatter signal over the range interval; (bottom right) α coefficient estimated, over the range interval between 30-35 km on a ray-by-ray basis, using the direct $\alpha = \Delta DWR / \Delta \Phi_{DP-X}$ method. This was determined to be a "mixed-phase" column, which was confirmed with higher α 's and increasing Mie signal with height. The vertical profiles show near-zero Z_{DR-S} , with $Z_{H-S} \approx 50$ dBZ, and decreasing K_{DP-X} above 3 km, indicating spherical particles probably due to wet hail aloft.

phase at X-band which can cause a singularity in the relation, $\beta \approx \Delta Z_{DR} / \Delta \Phi_{DP-X}$. We focus on the 25-30 km range interval below 5 km, dominated by rain only, and avoid the mixed phase 30-35 km interval with prevailing hail regions, apparent in the near-zero Z_{DR-S} column aloft above 2 km.

In Figure 6.7 the estimation of β coefficient in a rain-only range interval between 25-30 km and below 6 km in height is considered, where in the left panel are the vertical profiles of Z_{H-S} , Z_{DR-S} , Z_{DR-X} , and K_{DP-X} ; (top right) the ΔZ_{DR} signal as an RHI scan; and

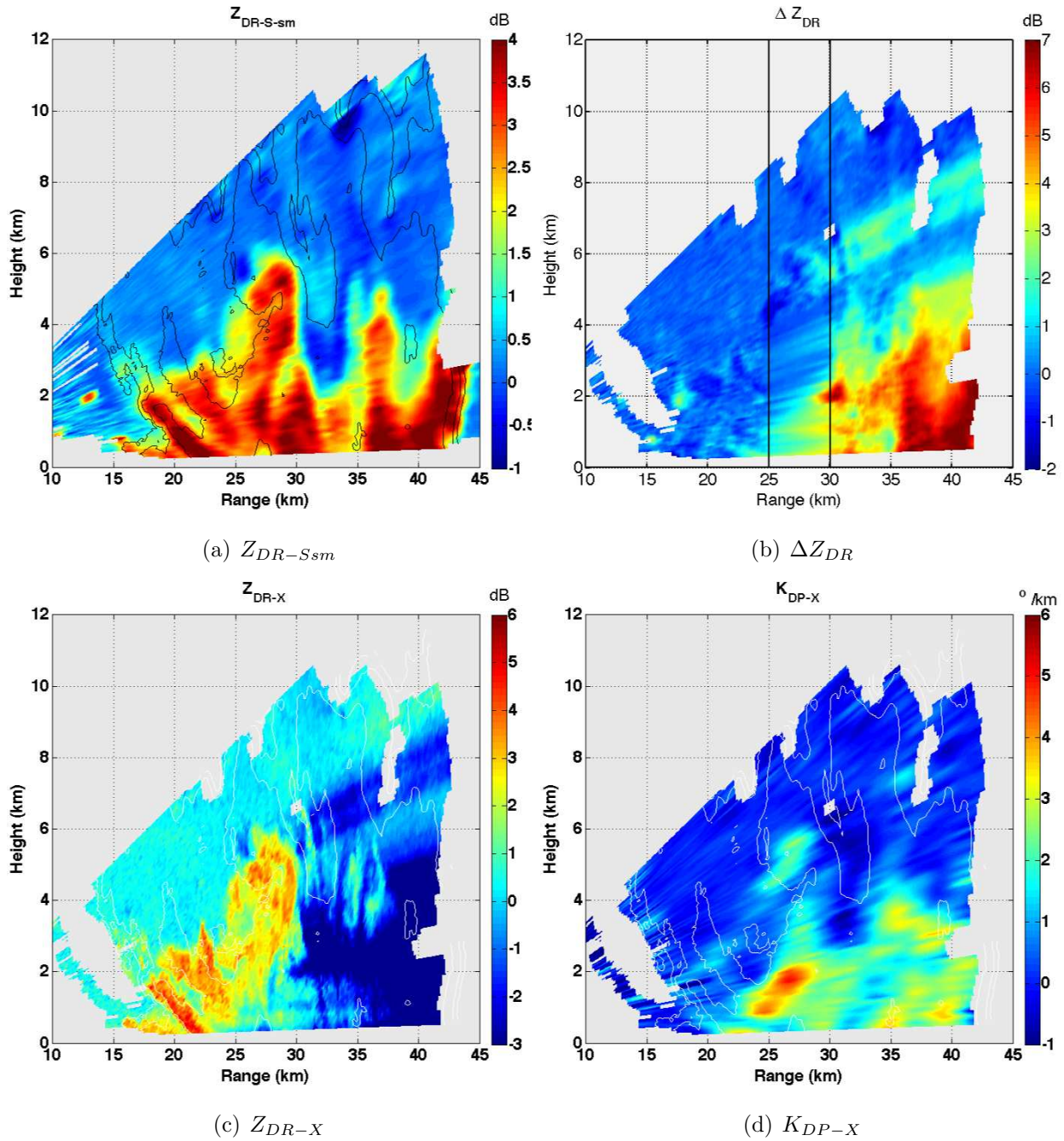


FIGURE 6.6. (a) Z_{DR-S} RHI showing a convective storm with high differential reflectivities above 3 dB up to 5 km above ground; (c) Z_{DR-X} showing attenuation starting at 25 km and beyond; (b) Dual-wavelength Differential Reflectivity, DFR $Z_{DR} = Z_{DR-S} - Z_{DR-X}$; (d) K_{DP-X} indicating heavy rain around 25 km, below 2 km height. Data collected from a CHILL S-X RHI scan, at $AZ = 291^{\circ}$, on 20130803 21:42 UTC.

(bottom right) the ΔZ_{DR} -derived β coefficient as a function of height. For reference, the increasing K_{DP-X} within the range interval and below 2 km, indicates propagation through larger hydrometeors of the convective rain complex. The ΔZ_{DR} signal is on average a 2.3 dB difference, and $\Delta\Phi_{DP-X} \approx 35^\circ$, resulting in $\beta \approx 0.06$ dB/deg, which is in good agreement with the 2DVD scattering simulations obtained in rain, as presented by [22]. We see a spike in the ΔZ_{DR} -derived β (bottom right) around 2 km height and again around 3.5 km due to a drop in K_{DP-X} (see Figure 6.6), probably due to mixed phase and some wet hail at these altitudes along the radial range interval.

6.2.3. SUMMARY OF VARIABILITY IN α & β COEFFICIENTS USING DUAL WAVELENGTH TECHNIQUES. In this chapter, the variability in α and β coefficients as a function of height in different precipitation regimes, using several RHIs from the CSU-CHILL S/X-band radar at 21:42, 21:53, and 22:03 UTC on 3 August 2013. In Figure 6.8, the variability of the dual-wavelength derived α & β coefficients as a function of height, in the rain-only range intervals, are attained from the three successive RHI scans. In (a) the height-interval mean α coefficient, below 2.5 km, is near 0.3 dB/deg as expected for rain only, and more importantly there is little variability as confirmed by the standard deviation about the mean. The histogram of α 's in panel (b) confirms its mode is near the theoretical value of 0.3 dB/deg, while the compiled height-interval means and standard deviations (over 1 km intervals) are listed in Table 6.1. In panels (c) and (d) it is obvious that the mean ΔZ_{DR} -derived β coefficient is slightly lower, at 0.045 dB/deg, than the simulated value of 0.06 dB/deg, but in good agreement with X-band radar-derived β value of 0.0371 dB/deg observed by [22]. The standard deviation is about 0.02 dB/deg below 2 km where it is mostly rain, but increases with height where more mixed phase hydrometeors are expected to exist. In Figure 6.9, it is apparent that the increased mean DWR-derived α coefficient in rain-hail mixed phase

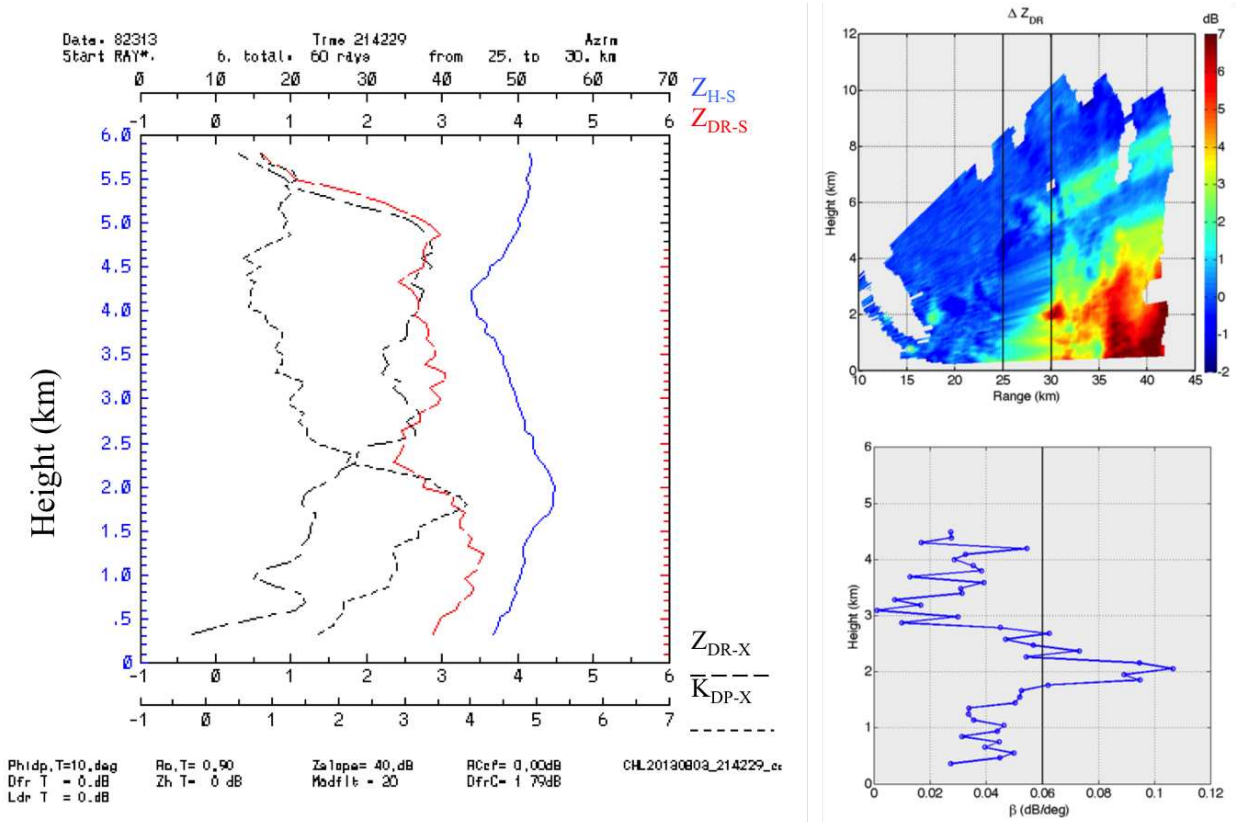
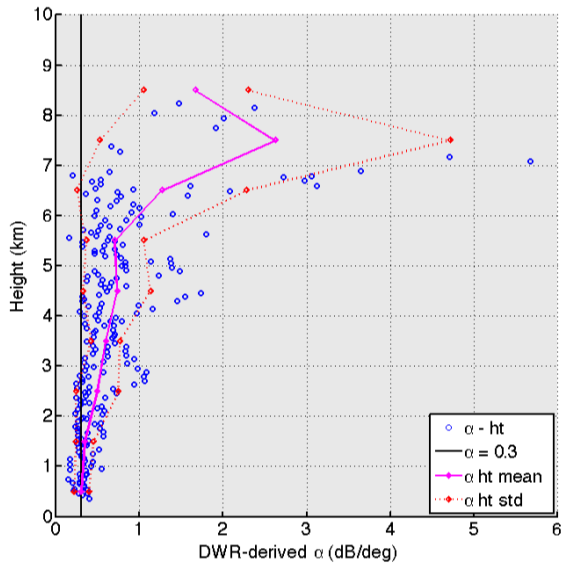


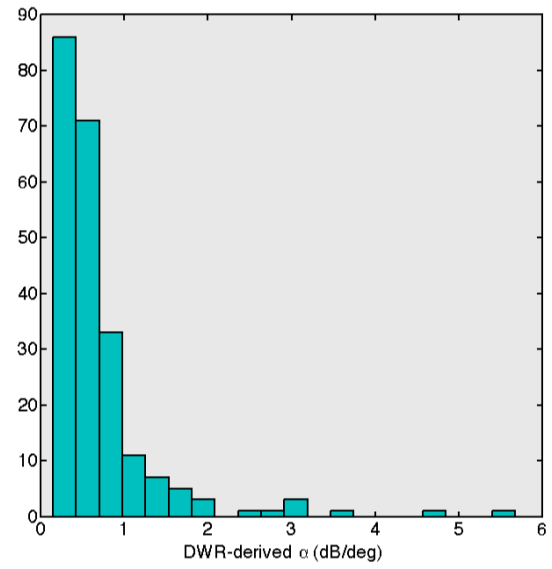
FIGURE 6.7. β vs. height in Rain-only. (left) Vertical profiles, between range=25-30 km, of Z_{H-S} , Z_{DR-S} , Z_{DR-X} , and K_{DP-X} from a CHILL S-X RHI scan, at $AZ = 291^\circ$, on 20130803-2142 UTC; (top right) $1dB < \Delta Z_{DR} < 3.5dB$ over the range interval and below 2 km height; (bottom right) β coefficient estimated, over the range interval between 25-30 km on a ray-by-ray basis, using the direct $\beta = \Delta Z_{DR} / \Delta \Phi_{DP-X}$ method. This was in a heavy "Rain-only" region below 3 km in height, which was confirmed with $\beta \approx 0.06dB/deg$.

regions at about 0.5 dB/deg, and also the higher variability as compared to the rain-only range intervals.

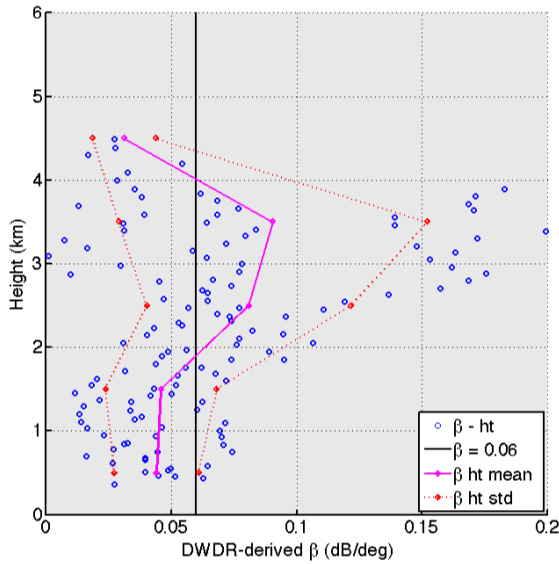
The compiled height-interval means and standard deviations of α and β coefficients, over 1 km intervals from the ground to an upper limit of 9 km and 5 km, respectively, including those computed over the total observed heights. Table 6.1 shows these computed means and standard deviations for α & β in rain only and rain-Hail mixed phase regions that are presented here as a small sample of the variability of these coefficients.



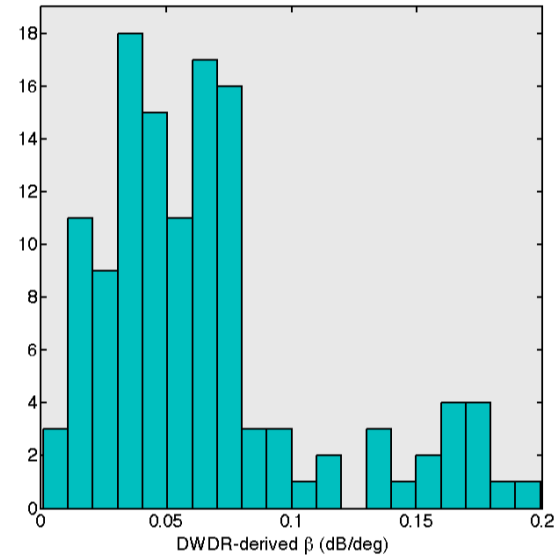
(a)



(b)



(c)



(d)

FIGURE 6.8. Dual-wavelength derived α and β coefficients in Rain only. Radar data was collected by CSU-CHILL S/X band radar on 20130803 at 21:42, 21:53, and 22:03 UTC.

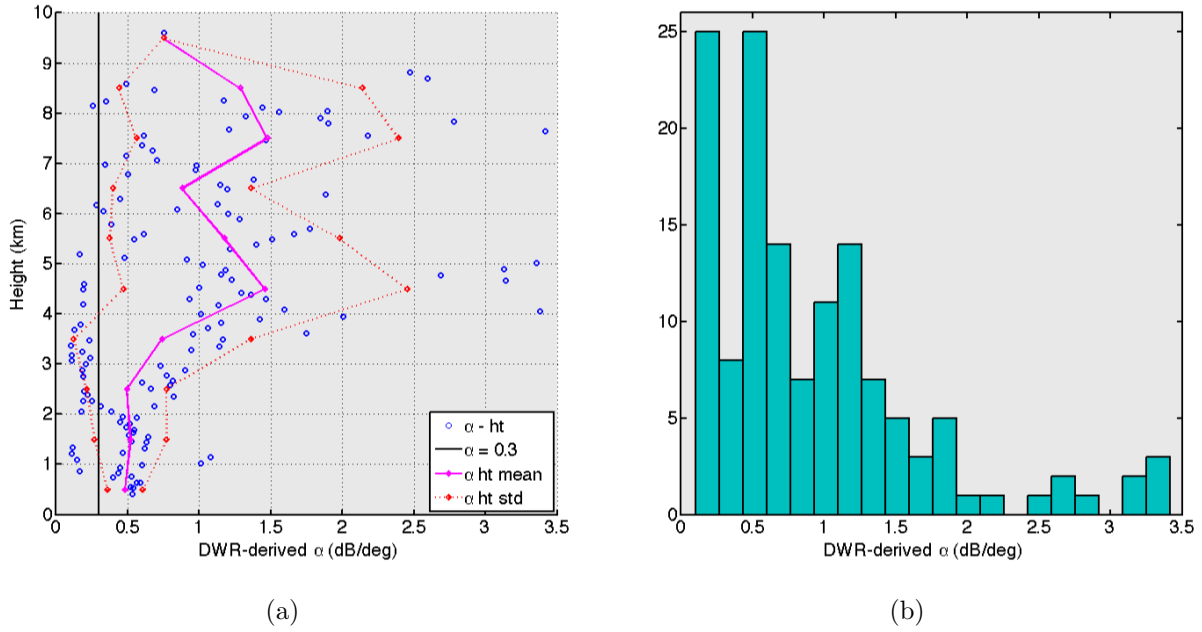


FIGURE 6.9. Dual-wavelength derived α coefficient in Rain-Hail mixed phase. (a) Radar data was collected by CSU-CHILL S/X band radar on 3 August 2013 at 21:42, 21:53, and 22:03 UTC.

TABLE 6.1. Variability of Dual Wavelength derived α and β coefficients with Height

Height Interval	Rain Only				Rain-Hail	
	α_{avg}	α_{std}	β_{avg}	β_{std}	α_{avg}	α_{std}
0-1 km	0.3090	0.0901	0.0442	0.0167	0.4838	0.1239
1-2 km	0.3499	0.1051	0.0459	0.0222	0.5236	0.2516
2-3 km	0.4942	0.2559	0.0809	0.0407	0.4937	0.2786
3-4 km	0.5944	0.1714	0.0442	0.0167	0.7416	0.6166
4-5 km	0.7306	0.4021	0.0905	0.0616	1.4597	0.9903
5-6 km	0.7077	0.3423			1.1783	0.8040
6-7 km	1.2679	1.0160			0.8804	0.4810
7-8 km	2.6223	2.0917			1.4763	0.9152
8-9 km	1.6738	0.6277			1.2901	0.8496
0-5 km			0.0651	0.0444		
0-9 km	0.7002	0.6827			0.9243	0.7441

CHAPTER 7

SUMMARY, CONCLUSIONS

This body of work has presented the primary objectives of this research and the results, obtained from data collected during the Iowa Flood Studies (IFloodS) in spring 2013, to support the proposed solutions. In Chapter 3, we presented the role regional climatology has on the variability of drop size distributions of 2DVD scattering simulations, relative to the effects in a global sense. We also presented the effects on scattering-derived *alpha* and *beta* coefficients, of the $A_H - K_{DP}$ and $A_{DP} - K_{DP}$ relations, as well as how these coefficients vary based on regional versus global climatologies. The ranges in *alpha* and *beta* coefficients, extracted from the Global histograms are applicable to coefficient optimization in the iterative ZPHI method, with Φ_{DP} constraint. In Chapter 4 we presented the ZPHI method for attenuation correction, tuned for X-band polarimetric radars with high spatio-temporal resolution and dedicated to hydrology studies of vast river basins and watersheds. We proposed a new two-stage FIR range filtering technique with improved estimation of differential backscatter phase, due to Mie scattering effects at X-band, which has implications for more accurate K_{DP} estimates and related rain rated algorithms. In Chapter 5, we selected the XPOL radar platform of the Iowa Flood Center, i.e., the four-node transportable X-band polarimetric radar network dedicated to hydrology studies, for the development and validation of the modified ZPHI attenuation correction algorithm, and furthermore for validating the new backscatter differential phase estimator. The results shown herein for the XPOL-4 radar display good agreement between the regional 2DVD scattering simulations and the attenuation-corrected radar moments (Z_H , Z_{DR} , and K_{DP}) suggesting good quality data from the applied correction methodology. Although the correction method showed good

results for rain-only events, it is difficult to fully correct attenuation near the melting layer where a mixed phase of rain and melting graupel exists. In Chapter 6 we highlight the benefits of dual-wavelength reflectivity (DWR) and differential reflectivity (ΔZ_{DR}) algorithms, developed with CSU-CHILL S/X-band radar, to directly and separately estimate the path integrated attenuation due to rain and wet snow/ice in the region near the melting layer. The DWR and ΔZ_{DR} algorithms were also key in determining the variability in direct measurement estimates of α and β coefficients, as a function of height above the ground and for different precipitation types.

The research objectives were met, and will compliment the body of knowledge regarding attenuation correction for polarimetric weather radars operating at high spatio-temporal resolutions in the shorter X-band wavelength regime. Although the results presented herein proved to be significant improvements to the present readily available X-band polarimetric technologies, the future of X-band polarimetric weather radars lies in phased-array platforms yielding much faster scan times, thereby making even higher spatio-temporal rain rate estimates. Phased array radars will need to overcome cost prohibitive barriers, as well as antenna impurities seen off the beam boresight, that can contribute significant sidelobe interference.

BIBLIOGRAPHY

- [1] R. J. Doviak and D. S. Zrnic, *Doppler Radar and Weather Observations*. Academic Press Inc., 2nd ed., 1993.
- [2] V. Bringi and V. Chandrasekaran, *Polarimetric Doppler Weather Radar: Principles and Applications*. Cambridge University Press., 2001.
- [3] F. Junyent, V. Chandrasekar, V. N. Bringi, S. A. Rutledge, P. C. Kennedy, D. Brunkow, J. George, and R. Bowie, “Transformation of the CSU–CHILL Radar Facility to a Dual-Frequency, Dual-Polarization Doppler System,” *Bulletin of the American Meteorological Society*, vol. 96, no. 6, pp. 975–996, 2014.
- [4] K. V. Mishra, A. Kruger, and W. F. Krajewski, “Engineering Evaluation and Calibration of Iowa X-Band Polarimetric Radars,” in *EGU General Assembly Conference Abstracts*, vol. 15, p. 13010, 2013.
- [5] W. F. Krajewski, K. V. Mishra, R. Goska, D. Ceynar, B.-C. Seo, and A. Kruger, “Evaluation of Small-Scale Dual-Polarimetric Measurements of Iowa XPOL Radars During the IFloodS Campaign,” in *AGU Fall Meeting Abstracts*, vol. 1, p. 1430, 2013.
- [6] V. N. Bringi, R. Hoferer, D. A. Brunkow, R. Schwerdtfeger, V. Chandrasekar, S. A. Rutledge, J. George, and P. C. Kennedy, “Design and Performance Characteristics of the New 8.5-m Dual-Offset Gregorian Antenna for the CSU–CHILL Radar,” *Journal of Atmospheric and Oceanic Technology*, vol. 28, no. 7, pp. 907–920, 2011.
- [7] S. Y. Matrosov, P. Kennedy, and R. Cifelli, “Dual-wavelength estimates of X-band radar signal attenuation characteristics in rain,” in *ERAD 2014- The eighth European Convergence on Radar in Meteorology and Hydrology*, 2014.

- [8] S. C. Michaelides, ed., *Precipitation: advances in measurement, estimation and prediction*. Springer-Verlag, 2008.
- [9] A. Kruger and W. F. Krajewski, “Two-dimensional video disdrometer: a description,” *Journal of Atmospheric and Oceanic Technology*, vol. 19, pp. 602–617, 2002.
- [10] P. C. Waterman, “Symmetry, Unitarity, and Geometry in Electromagnetic Scattering,” *Physical Review*, vol. D, no. 3, p. 825, 1971.
- [11] P. B. Gatlin, M. Thurai, V. N. Bringi, W. Petersen, D. Wolff, A. Tokay, L. Carey, and M. Wingo, “Searching for Large Raindrops: A Global Summary of Two-Dimensional Video Disdrometer Observations,” *Journal of Applied Meteorology and Climatology*, vol. 54, pp. 1069–1089, 2015.
- [12] C. R. Williams, V. Bringi, L. D. Carey, V. Chandrasekar, P. N. Gatlin, Z. S. Haddad, R. Meneghini, S. Joseph Munchak, S. W. Nesbitt, W. A. Petersen, *et al.*, “Describing the shape of raindrop size distributions using uncorrelated raindrop mass spectrum parameters,” *Journal of Applied Meteorology and Climatology*, vol. 53, no. 5, pp. 1282–1296, 2014.
- [13] M. Thurai, C. R. Williams, and V. N. Bringi, “Examining the correlations between drop size distribution parameters using data from two side-by-side 2D-video disdrometers,” *Atmospheric Research*, vol. 144, pp. 95–110, 2014.
- [14] W. F. Krajewski, K. V. Mishra, M. B. Galvez, R. Goska, M. Thurai, V. Bringi, L. Tolstoy, A. Kruger, and W. A. Petersen, “Salient observations and performance evaluation of Iowa XPOL radars during the NASA GPM IFloodS campaign,” in *AGU Fall Meeting*, 2014.

- [15] W. A. Petersen and M. Jensen, “The NASA-GPM and DOE-ARM Midlatitude Continental Convective Clouds Experiment (MC3E),” *The Earth Observer*, vol. 24, pp. 12–18, January-February 2012 2012.
- [16] H. C. Barnes and J. R. A. Houze, “The precipitating cloud population of the Madden-Julian Oscillation over the Indian and west Pacific Oceans,” *Journal of Geophysical Research*, vol. 118, pp. 6996–7023, 2013.
- [17] E. J. Thompson, S. A. Rutledge, B. Dolan, and M. Thurai, “Drop size distributions and radar observations of convective and stratiform rain over the equatorial Indian and West Pacific Oceans,” *Journal of the Atmospheric Sciences*, vol. <http://dx.doi.org/10.1175/JAS-D-14-0206.1>, 2015.
- [18] J. S. Marshall and W. M. Palmer, “The distribution of raindrops with size,” *Journal of Meteorology*, vol. 5, pp. 165–166, 1948.
- [19] A. Ryzhkov, M. Diederich, P. Zhang, and C. Simmer, “Potential Utilization of Specific Attenuation for Rainfall Estimation, Mitigation of Partial Beam Blockage, and Radar Networking,” *Journal of Atmospheric and Oceanic Technology*, vol. 31, no. 3, pp. 599–619, 2014.
- [20] A. R. Jameson, “The effect of temperature on attenuation correction schemes in rain using polarization propagation differential phase shift,” *Journal of Applied Meteorology*, vol. 31, pp. 1106–1118, 1992.
- [21] D.-S. Kim, M. Maki, and D.-I. Lee, “Retrieval of Three-Dimensional Raindrop Size Distribution Using X-Band Polarimetric Radar Data,” *Journal of Atmospheric and Oceanic Technology*, vol. 27, no. 8, pp. 1265–1285, 2010.
- [22] S.-G. Park, M. Maki, K. Iwanami, V. N. Bringi, and V. Chandrasekar, “Correction of Radar Reflectivity and Differential Reflectivity for Rain Attenuation at X Band. Part II:

- Evaluation and Application,” *Journal of Atmospheric and Oceanic Technology*, vol. 22, no. 11, pp. 1633–1655, 2005.
- [23] K. V. Mishra, W. F. Krajewski, R. Goska, D. Ceynar, B.-C. Seo, A. Kruger, J. J. Niemeier, M. B. Galvez, M. Thurai, V. N. Bringi, L. Tolstoy, P. A. Kucera, W. A. Petersen, J. Grazioli, and A. L. Pazmany, “Deployment and Performance Analyses of High-Resolution Iowa XPOL Radar System during the NASA IFloodS Campaign,” *Journal of Hydrometeorology*, 2015.
- [24] J. Testud, E. Le Bouar, E. Obligis, and M. Ali-Mehenni, “The Rain Profiling Algorithm Applied to Polarimetric Weather Radar,” *Journal of Atmospheric and Oceanic Technology*, vol. 17, no. 3, pp. 332–356, 2000.
- [25] V. Bringi, T. Keenan, and V. Chandrasekar, “Correcting C-band radar reflectivity and differential reflectivity data for rain attenuation: a self-consistent method with constraints,” *Geoscience and Remote Sensing, IEEE Transactions on*, vol. 39, no. 9, pp. 1906–1915, 2001.
- [26] S.-G. Park, V. N. Bringi, V. Chandrasekar, M. Maki, and K. Iwanami, “Correction of Radar Reflectivity and Differential Reflectivity for Rain Attenuation at X Band. Part I: Theoretical and Empirical Basis,” *Journal of Atmospheric and Oceanic Technology*, vol. 22, no. 11, pp. 1621–1632, 2005.
- [27] K. V. Beard and C. Chuang, “A New Model for the Equilibrium Shape of Raindrops,” *Journal of the Atmospheric Sciences*, vol. 44, no. 11, pp. 1509–1524, 1987.
- [28] E. N. Anagnostou, M. N. Anagnostou, W. F. Krajewski, A. Kruger, and B. J. Miriovsky, “High-Resolution Rainfall Estimation from X-Band Polarimetric Radar Measurements,” *Journal of Hydrometeorology*, vol. 5, no. 1, pp. 110–128, 2004.

- [29] S. Y. Matrosov, D. E. Kingsmill, B. E. Martner, and F. M. Ralph, "The Utility of X-Band Polarimetric Radar for Quantitative Estimates of Rainfall Parameters," *Journal of Hydrometeorology*, vol. 6, no. 3, pp. 248–262, 2005.
- [30] E. Gorgucci and V. Chandrasekar, "Evaluation of Attenuation Correction Methodology for Dual-Polarization Radars: Application to X-Band Systems," *Journal of Atmospheric and Oceanic Technology*, vol. 22, no. 8, pp. 1195–1206, 2005.
- [31] T. J. Smyth and A. J. Illingworth, "Correction for attenuation of radar reflectivity using polarization data," *Quarterly Journal of the Royal Meteorological Society*, vol. 124, no. 551, pp. 2393–2415, 1998.
- [32] V. Bringi, M. T. Thurai, K. Nakagawa, G. J. Huang, T. Kobayashi, A. Adachi, H. Hanado, and S. Sekizawa, "Rainfall estimation from C-band polarimetric radar in Okinawa, Japan: Comparisons with 2D-video disdrometer and 400 MHz wind profiler," *Journal of the Meteorological Society of Japan*, vol. 84, no. 4, pp. 705–724, 2006.
- [33] V. N. Bringi, C. R. Williams, M. Thurai, and P. T. May, "Using Dual-Polarized Radar and Dual-Frequency Profiler for DSD Characterization: A Case Study from Darwin, Australia," *Journal of Atmospheric and Oceanic Technology*, vol. 26, no. 10, pp. 2107–2122, 2009.
- [34] J. Hubbert and V. N. Bringi, "An Iterative Filtering Technique for the Analysis of Copolar Differential Phase and Dual-Frequency Radar Measurements," *Journal of Atmospheric and Oceanic Technology*, vol. 12, no. 3, pp. 643–648, 1995.
- [35] A. V. Ryzhkov, S. E. Giangrande, and T. J. Schuur, "Rainfall Estimation with a Polarimetric Prototype of WSR-88D," *Journal of Applied Meteorology*, vol. 44, no. 4, pp. 502–515, 2005.

- [36] M. Thurai, G. J. Huang, V. N. Bringi, W. L. Randeu, and M. Schönhuber, “Drop Shapes, Model Comparisons, and Calculations of Polarimetric Radar Parameters in Rain,” *Journal of Atmospheric and Oceanic Technology*, vol. 24, no. 6, pp. 1019–1032, 2007.
- [37] G.-J. Huang, V. N. Bringi, and M. Thurai, “Orientation Angle Distributions of Drops after an 80-m Fall Using a 2D Video Disdrometer,” *Journal of Atmospheric and Oceanic Technology*, vol. 25, no. 9, pp. 1717–1723, 2008.
- [38] M. Maki, K. Iwanami, R. Misumi, S.-G. Park, H. Moriwaki, K.-i. Maruyama, I. Watabe, D.-I. Lee, M. Jang, H.-K. Kim, V. N. Bringi, and H. Uyeda, “Semi-operational rainfall observations with X-band multi-parameter radar,” *Atmospheric Science Letters*, vol. 6, no. 1, pp. 12–18, 2005.
- [39] M. Maki, T. Maesaka, R. Misumi, K. Iwanami, S. Suzuki, A. Kato, S. Shimizu, K. Kieda, T. Yamada, H. Hirano, F. Kobayashi, A. Masuda, T. Moriya, Y. Suzuki, A. Takahori, D.-I. Lee, D.-S. Kim, V. Chandrasekar, and Y. Wang, “X-band polarimetric radar network in the Tokyo metropolitan area -X-NET,” in *The 5th European Conf. Radar in Meteorology and Hydrology, Helsinki, Finland*, p. 5 pp (in CD), ERAD, 2008.
- [40] D. McLaughlin, D. Pepyne, B. Philips, J. Kurose, M. Zink, D. Westbrook, E. Lyons, E. Knapp, A. Hopf, A. Defonzo, R. Contreras, T. Djaferis, E. Insanic, S. Frasier, V. Chandrasekar, F. Junyent, N. Bharadwaj, Y. Wang, Y. Liu, B. Dolan, K. Droege-meier, J. Brotzge, M. Xue, K. Kloesel, K. Brewster, F. Carr, S. Cruz-Pol, K. Hondl, and P. Kollias, “Short-Wavelength Technology and the Potential For Distributed Networks of Small Radar Systems,” *Bulletin of the American Meteorological Society*, vol. 90, no. 12, pp. 1797–1817, 2009.

- [41] R. G. Lyons, *Understanding Digital Signal Processing*. Addison Wesley Longman, Inc., 1997.
- [42] M. H. Hayes, *Schaum's Outline of Digital Signal Processing*. McGraw-Hill, 1999.
- [43] T. Otto and H. W. J. Russchenberg, "Estimation of specific differential phase and differential backscatter phase from polarimetric weather radar measurements of rain," *Geoscience and Remote Sensing Letters, IEEE*, vol. 8, no. 5, pp. 988–992, 2011.
- [44] W. A. Petersen and W. F. Krajewski, "An overview of the Iowa Flood Studies (IFloodS) GPM Ground Validation field campaign," *Journal of Hydrometeorology*, 2015.
- [45] P. Barber and C. Yeh, "Scattering of electromagnetic waves by arbitrarily shaped dielectric bodies," in *Applied Optics*, vol. 14, pp. 2864–2872, 1975.
- [46] F. Fabry and I. Zawadski, "Long-Term Radar Observations of the Melting Layer of Precipitation and Their Interpretation," *Journal of the Atmospheric Sciences*, vol. 52, no. 7, pp. 838–851, 1995.